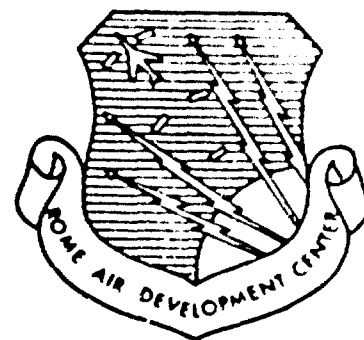AD616001

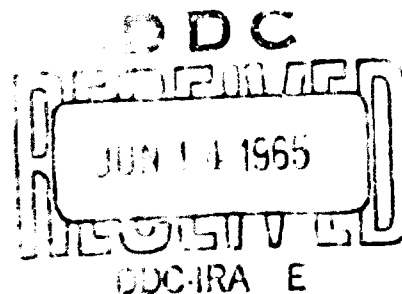# INVESTIGATION OF LINEAR BEAM AND NEW CONCEPTS OF MICROWAVE POWER

Volume VI - Laser-Stimulated Electron Emission

L. A. MacKenzie

D. M. Stevenson

D D C

JUN 1 4 1965

DDC-IRA E

INVESTIGATION OF LINEAR BEAM AND
NEW CONCEPTS OF MICROWAVE POWER

Volume VI - Laser-Stimulated Electron Emission

L. A. MacKenzie
D. M. Stevenson

THE DIFFUSION OF MAGNETIC FIELDS THROUGH CONDUCTORS AND
THE DESIGN OF PULSED SOLENOIDS

L. A. MacKenzie

ABSTRACT

The diffusion of time-varying magnetic fields through conductors is examined, and the quantitative results are applied to pulsed solenoids to obtain the axial magnetic fields produced by these devices. Based upon these results a design procedure is established for simple pulsed solenoids. A trial design and its experimental results are presented for comparison with the theory.

TABLE OF CONTENTS

Contents   Page

I. INTRODUCTION

Experimental requirements for large magnetic fields impose major
difficulties which are increased if high precision or field uniformity
is required. Continuous magnetic fields on the order of 100,000 gauss
are conventionally produced by large, heavy field coils or by expensive
superconducting magnetic systems. Field coils present cooling problems,
and the working volume of superconducting magnets tends to be small and
relatively inaccessible. If the magnetic field is not required for continuous
measurements, an attractive possibility is a pulsed solenoid. This device
has a ratio of total volume to working volume as desirable as the super-
conducting magnet, but the working volume can be large since elaborate
cooling is not required. In addition, a pulsed solenoid is readily designed
and inexpensively fabricated if extreme field uniformity is not required.
One disadvantage of a pulsed solenoid is that when metallic vessels are
placed within the field, because the magnetic field is time varying,
electric fields are induced that produce currents in the conductors.
These currents in turn produce a magnetic field opposing the original
field, which means the net magnetic field within a metallic vessel is
less than one would expect for a d-c solenoid. These effects can be
described by a diffusion process of the magnetic field or in terms of
the "eddy currents" familiar in the electrical power field. This report
examines this reduction of the magnetic field within pulsed solenoids
and gives quantitative results useful for designing them.

II. THEORY OF MAGNETIC FIELD DIFFUSION

This section describes the diffusion of pulsed magnetic fields through metallic vessels placed within a solenoid. In all cases, the solenoids are idealized ones in which end effects are neglected; i.e., solenoids are assumed to be infinitely long as are the metallic vessels. The object is to determine the relationship between the thickness of the metallic vessels and the resultant decrease of field within these vessels.

A. DIFFUSION EQUATION

The expressions governing magnetic field behavior may be found from Maxwell's curl equations:

$$\underline{\nabla} \times \underline{B} = \mu \, \underline{i} + \mu\epsilon \, \frac{\partial E}{\partial t} \tag{1}$$

$$\underline{\nabla} \times \underline{E} = - \frac{\partial B}{\partial t} \quad . \tag{2}$$

Consider linear, homogeneous, and isotropic media, where the conduction current density is related to the electric field by Ohm's law,

$$\underline{i} = \sigma \, \underline{E} \quad . \tag{3}$$

Finally, consider metallic media where the conductivity is sufficiently large that the displacement current can be neglected with respect to the conduction current; i.e.,

$$\frac{\epsilon}{\sigma |\underline{E}|} \left| \frac{\partial E}{\partial t} \right| \ll 1 \quad . \tag{4}$$

With these assumptions, Equations (1), (2), and (3) may be combined to give:

$$\left[\nabla^2 - \mu\,\sigma\,\frac{\partial}{\partial t}\right] \begin{bmatrix} \underline{B} \\ \underline{i} \\ \underline{E} \end{bmatrix} = 0 \qquad\qquad (5)$$

where the nomenclature indicates that each of the field quantities satisfies Equation (5) separately. Equation (5) is recognized as the standard form of a diffusion equation and will adequately describe the field behavior within good conductors at least to millimeter wavelengths.

The standard wave equation is appropriate for the electric and magnetic fields in regions outside of the conductors where the conductivity is zero. Here, however, the discussion is limited to the case where operating frequencies are sufficiently low and physical spacings in the transverse direction are sufficiently small that a finite velocity of propagation need not be considered. Thus, for regions outside of conductors, the following expressions apply:

$$\left[\nabla^2\right] \begin{bmatrix} \underline{B} \\ \underline{E} \end{bmatrix} = 0 \quad . \qquad\qquad (6)$$

All that remains is to solve Equations (5) and (6) subject to the appropriate boundary and initial conditions of interest. Since this is to apply to pulsed magnets, it is the transient phenomena rather than the steady-state phenomena that are of interest. With this application and the fact that Equation (5) is a partial differential equation in time

and space, the solution of these expressions is most simply accomplished by a Laplace transform in time, thus let

$$\underline{\beta} = \int_{0}^{\infty} e^{-pt} \ \underline{B} \ dt \tag{7.a}$$

$$\underline{\epsilon} = \int_{0}^{\infty} e^{-pt} \ \underline{E} \ dt \tag{7.b}$$

$$\underline{j} = \int_{0}^{\infty} e^{-pt} \ \underline{i} \ dt. \tag{7.c}$$

With the initial conditions that all field quantities are zero at and before $t = 0$, the field equations reduce to

$$\left[\nabla^2 - \mu\sigma p \right] \begin{bmatrix} \beta \\ \epsilon \\ j \end{bmatrix} = 0 \tag{8.a}$$

in conducting regions and

$$\left[\nabla^2 \right] \begin{bmatrix} \beta \\ \epsilon \end{bmatrix} = 0 \tag{8.b}$$

in nonconducting regions.

B. SOLUTIONS FOR RECTANGULAR GEOMETRY

It is instructive to consider first a very simple geometry for the pulsed solenoid configuration, so that the mathematics is fairly simple. Once the behavior in a simple system is understood, it is readily extended to more complex (and more realistic) situations.

-4-

The first structure considered is shown in Figure 1. A nonmagnetic metal slab of thickness 2T is placed midway between two infinite current sheets located as shown. The system has mechanical symmetry about $x = 0$ and is infinite in extent in both the y and z directions. In this system of rectangular co-ordinates, Equation (8) becomes

$$\left[\frac{d^2}{dx^2} - \tilde{\gamma}^2\right] \begin{bmatrix} \beta_z \\ \epsilon_y \\ j_y \end{bmatrix} = 0 \tag{9.a}$$

$$\left[\frac{d^2}{dx^2}\right] \begin{bmatrix} \beta_z \\ \epsilon_y \end{bmatrix} = 0 \tag{9.b}$$

where

$$\tau^2 = \mu\sigma p \quad . \tag{10}$$

The field quantities are related to each other by the following expressions:

$$\frac{d\epsilon_y}{dx} = -p\beta_z \tag{11.a}$$

$$\frac{d\beta_z}{dx} = -\mu\sigma\epsilon_y \quad . \tag{11.b}$$
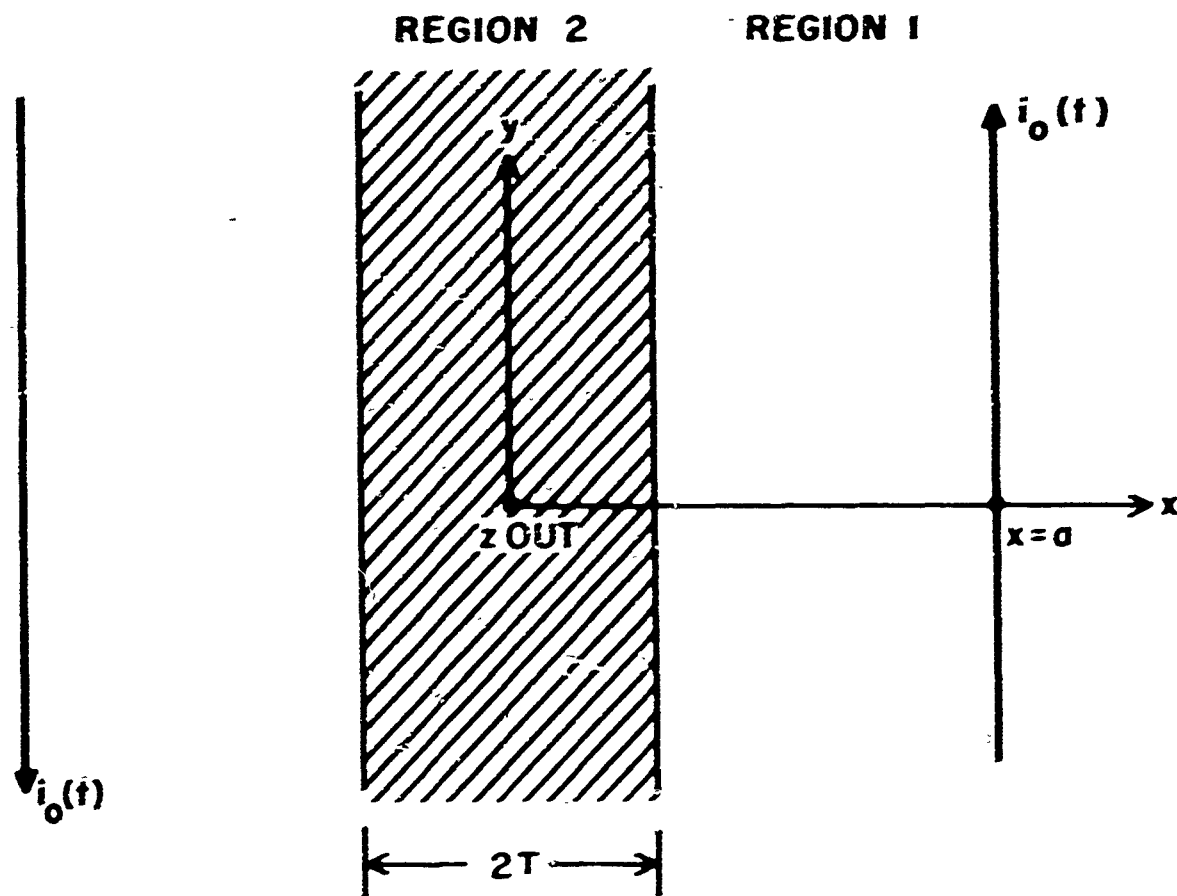
Figure 1. Schematic Structure of Simple Pulsed Solenoid System in Rectangular Co-ordinates.

The solutions of Equations (9) and (11) are easily found as follows (the x, y, z subscripts are now dropped, and the subscripts 1, 2 added to denote quantities in regions 1 and 2 shown in Figure 1):

for $0 < x < T$:

$$j_2 = A \, e^{\mathcal{T}x} + Be^{-\mathcal{T}x} \qquad\qquad (12.a)$$

$$\epsilon_2 = \frac{A}{\sigma} \, e^{\mathcal{T}x} + \frac{B}{\sigma} \, e^{-\mathcal{T}x} \qquad\qquad (12.b)$$

$$\beta_2 = -\frac{\mathcal{T}}{\rho\sigma} (A \, e^{\mathcal{T}x} - B \, e^{-\mathcal{T}x}) \; ; \qquad\qquad (12.c)$$

for $T < x < a$:

$$j_1 = 0 \tag{13.a}$$

$$\epsilon_1 = -p\, C_x + D \tag{13.b}$$

$$\beta_1 = C \tag{13.c}$$

In Equations (12) and (13) the quantities A, B, C, D are constants of integration. These constants are found from the boundary conditions for the continuity of tangential field components across the boundaries. Also, from symmetry considerations it is clear that

$$j_2 \Big|_{x=0} = 0$$

from which $A = -B$. If we denote the Laplace transform of $i_o(t)$ by $j_o(p)$, then the discontinuity in magnetic field at $x = a$ is related to the forcing current as

$$\beta_1 = \mu\, j_o \quad . \tag{14}$$

Finally, equating Equations (12c) and (13c) establishes the constants A and B, so that the magnetic field within the conductor is given by

$$\beta_2 = \mu j_o \; \frac{\cosh\,(\mathcal{T}x)}{\cosh\,(\mathcal{T}T)} \quad . \tag{15}$$

The axial magnetic field as a function of time is given by the inverse transform of Equation (15). A general solution could be obtained if the

inverse transform is denoted by $g(t)$,

$$g(t) = \frac{1}{2\pi i} \int_{c-i\infty}^{c+i\infty} e^{pt} \frac{\cosh(\Gamma x)}{\cosh(\Gamma T)} \, dp \; ; \quad (16)$$

then the magnetic field can be expressed as the convolution integral

$$B(t) = \int_0^t i_o(t - u) \, g(u) \, du \; . \quad (17)$$

This expression is convenient for any waveform considered for $i_o(t)$, and the integrations are readily carried through for this simple example. Later examples, however, have sufficiently complex inverse transforms $g(t)$ that it is simpler to calculate the magnetic field directly from equations corresponding to Equation (15) for each waveform considered for $i_o(t)$ rather than to make use of the convolution integral in Equation (17). Thus, for purposes of comparison with later examples we deal with Equation (15) directly in this case.

Consider a rectangular current pulse, of height I_o and width t_o; then

$$j_o(P) = \frac{I_o}{P} (1 - e^{-pt_o}) \quad (18)$$

and from the inverse transform of Equation (15) at $x = 0$;

$$B_2(t) = \mu I_o \left[1 - \frac{2}{\pi} \sum_{n=0}^{\infty} \frac{(-1)^n}{\left(n+\frac{1}{2}\right)} e^{-(n+1/2)^2 \frac{\pi^2 t}{\mu\sigma T^2}} \right] \begin{array}{l} 0 < t < t_o \\ \\ (19) \end{array}$$

and

$$B_2(t) = f(t) - f(t-t_o) \qquad t > t_o \qquad (20)$$

where $f(t)$ is given by the expression in Equation (19). If we denote a characteristic frequency for this rectangular pulse ω, where

$$t_o = \frac{\pi}{\omega} \qquad (21)$$

then Equation (19) becomes

$$B_2(t) = \mu I_o \left[1 - \frac{2}{\pi} \sum_{n=0}^{\infty} \frac{(-1)^n}{(n+\frac{1}{2})} e^{- \frac{(n+1/2)^2}{\alpha^2} \frac{\pi^3}{2} (\frac{t}{t_o})} \right] \quad (22)$$

where

$$\alpha = \frac{T}{\delta} \ , \qquad \delta = \sqrt{\frac{1}{\pi f \mu}} \quad .$$

The quantity δ is recognized as the "skin depth" for the particular conductor at the characteristic frequency. It may be observed that the expression in Equation (22) does not converge rapidly for small values of t or large values of α. Another form for this expression may be obtained by utilizing the Poisson summation formula, which results in

$$B_2(t) = 2\mu I_o \sum_{n=0}^{\infty} (-1)^n \ \text{Erfc} \left[(n + \frac{1}{2}) \ \alpha \ \sqrt{\frac{2t_o}{\pi t}} \right] \quad (23)$$

and converges rapidly near $t = 0$. Of course, Equation (20) applies for $t > t_o$.

One other simple waveform for the forcing current is of interest: a current pulse described by one-half of a sine-wave function. This pulse shape closely matches that easily obtained in practice, while the rectangular pulse is considered here for simplicity in comparing various cases. For the half-sine-wave current pulse, one obtains

$$j_o(P) = I_o \ I_m \ \left(\frac{1 + e^{-pt_o}}{p - i\omega} \right) \qquad (24)$$

where I_m indicates that the imaginary part is to be taken. The result for the magnetic field found again from Equation (15) at $x = 0$ is

$$B_2(t) = \mu I_o \ I_m \left[\frac{e^{i\omega t}}{\cosh(\alpha \sqrt{2i})} - 2\pi \sum_{n=0}^{\infty} (-1)^n \ (n + \tfrac{1}{2}) \ \frac{e^{-\frac{(n+1/2)^2}{\alpha^2} \frac{\pi^3}{2} (\frac{t}{t_o})}}{(n + \tfrac{1}{2})^2 \pi^2 + i2\alpha} \right] \qquad (25)$$

where $t_o = \pi/\omega$ as before. Taking the imaginary part, as indicated, gives

$$B_2(t) = \mu I_o \left[\frac{\cosh(\alpha)\cos(\alpha)\sin(\omega t) - \sinh(\alpha)\sin(\alpha)\cos(\omega t)}{1 + \cosh^2(\alpha) - \cos^2(\alpha)} \right.$$

$$\left. + 4\pi\alpha^2 \sum_{n=0}^{\infty} \frac{(-1)^n(n + 1/2) \ e^{-(n+\frac{1}{2})^2 \frac{\pi^3}{2\alpha^2} (\frac{t}{t_o})}}{(n + 1/2)^4 \pi^4 + 4\alpha^4} \right] . \qquad (26)$$

Both of these expressions apply for $0 < t < t_o$, whereas

$$B_2(t) = f(t) + f(t-t_o), \qquad\qquad t > t_o \qquad (27)$$

where f(t) is given by Equation (26).

Before examining the past expressions to see the behavior of the axial magnetic field with time and the thickness of the conductor, one should consider another case with rectangular geometry, which is more realistic than that just considered and would represent a limiting condition of cylindrical geometry with a thin-shelled metal pipe inserted within the solenoid. This case in rectangular co-ordinates is shown in Figure 2. For this case, Equations (12) and (13) describe the fields in regions 1 and 2, while the fields in Region 3 are described by

$$j_3 = 0 \qquad\qquad (23.a)$$

$$\epsilon_3 = - P \, G \, x \qquad\qquad (23.b)$$

$$\beta_3 = G \qquad . \qquad\qquad (23.c)$$

In these equations the expression for the electric field is chosen so that it is zero at $x = 0$.

The constants are again determined by requiring continuity of the tangential fields across the boundaries. The result for the magnetic field on the axis at $x = 0$ is

$$\beta_3 = \mu j_0 \left[\frac{1}{\cosh(\mathcal{T}\mathrm{T}) + (\mathcal{T}\mathrm{c})\sinh(\mathcal{T}\mathrm{T})} \right] \qquad . \qquad (29)$$

This expression actually describes the magnetic field for the complete region inside of the conductor since the field is constant in this region, when a finite propagation velocity is not considered.
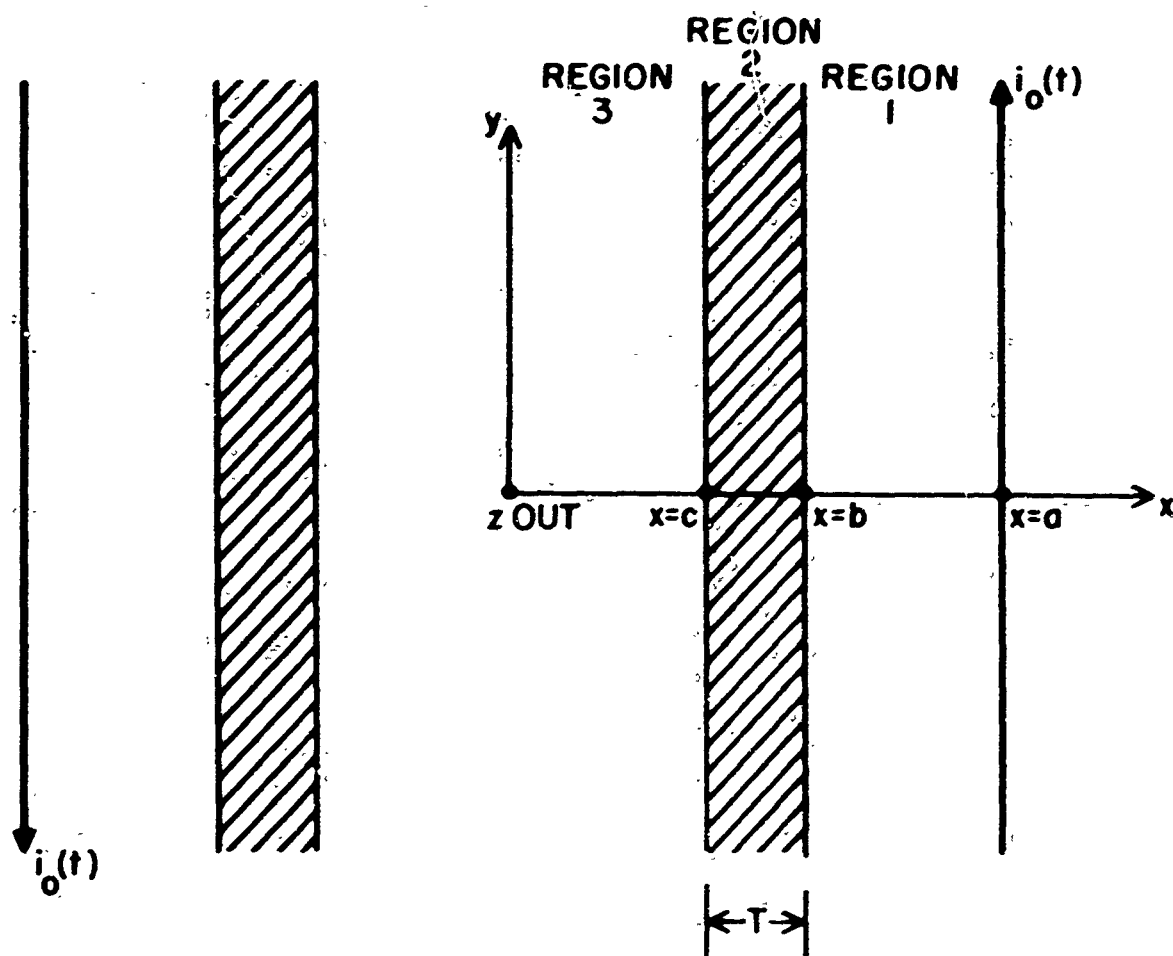
Figure 2. Schematic Structure of a Pulsed Solenoid with a Thin-Walled Conductor in Rectangular Co-ordinates.

For a rectangular forcing current pulse of height I_o and width t_o, Equation (18) applies, and the inverse transformation of Equation (29) yields

$$B_3(t) = \mu I_o \left[1 - 2 \sum_{n=o}^{\infty} \frac{e^{-a_n^2 \frac{\pi^3}{2a^2} (\frac{t}{t_o})}}{\cos(a_n \pi) \left(1 + \frac{T}{C} + a_n^2 \pi^2 \frac{C}{T} \right)} \right] \quad (30)$$

where the quantity a_n is given by the transcendental equation,

$$\tan (a_n \pi) = \frac{1}{a_n \pi \left(\frac{C}{T}\right)} \qquad . \tag{31}$$

The nomenclature here has been chosen so that

$$\lim_{n \rightarrow \infty} a_n = n \quad .$$

If the width of the conductor is much larger than the wall thickness; i.e., $\frac{C}{T} >> 1$, then

$$a_n \pi \approx n\pi + \frac{T}{Cn\pi} \quad , \qquad n \neq 0$$

$$a_0 \pi \approx \sqrt{\frac{T}{C}} \quad .$$

For these conditions Equation (30) is approximated by

$$B_3(t) \approx \mu I_0 \left[1 - e^{-\frac{T}{C} \frac{\pi}{2\pi^2} \left(\frac{t}{t_0}\right)} -2 \sum_{n=1}^{\infty} (-1)^n \frac{e^{-\frac{n^2 \pi^3}{2\alpha^2}\left(\frac{t}{t_0}\right)}}{n^2 \pi^2 \frac{C}{T}} \right] . \tag{32}$$

The results for the hollow conductor for the second current waveform, a half-sine wave, are not presented here. These are sufficiently complicated that it does not seem worth while to develop them, especially since no qualitatively new phenomena arise over those exhibited by the solutions in Equations (22), (26), and (30). If it should be desirable to calculate the axial magnetic field in this case, one need only combine Equations (24) and (29) and calculate the inverse transform.

$$\frac{c}{T} = 0$$

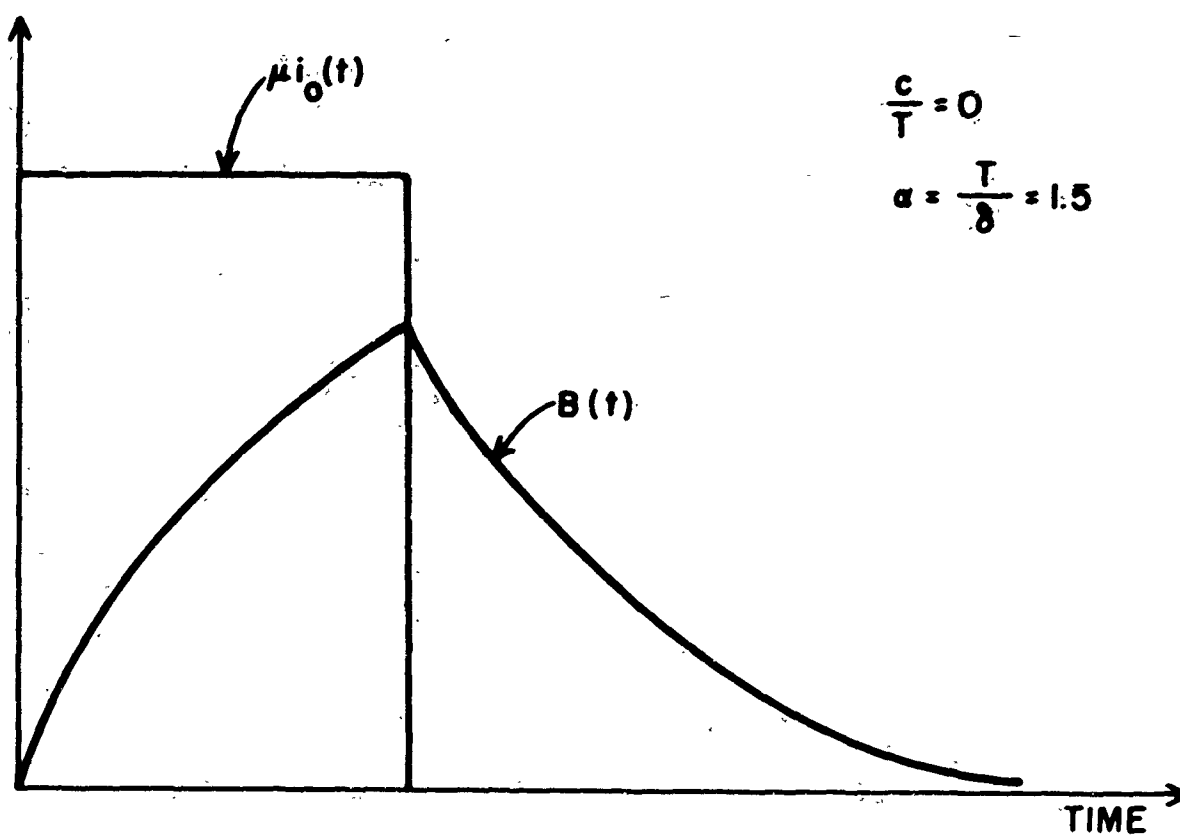$$a = \frac{T}{\delta} = 1.5$$

Figure 3. Axial Magnetic Field Versus Time for Rectangular Current Pulse for Rectangular Geometry.

A typical plot of the axial magnetic field for the rectangular current pulse is shown in Figure 3. For this current pulse, the magnetic field is always a maximum at $t = t_o$; i.e., at the end of the pulse. Thus on this basis, the variations of the maximum magnetic field for both the solid and hollow conductors is shown in Figure 4. In this figure the magnetic field is normalized to μI_o, which is the value that would apply under d-c excitation of the solenoid. The case of the half-wave sine current pulse is considered in detail in the next section where cylindrical geometry is treated.

1.0

0.8

$\dfrac{B}{\mu I_0}$

0.6

$\dfrac{c}{T} = 10$ 1   0

0.4

0.2

I_0

CURRENT
WAVEFORM

O   1.0   2.0   3.0   4.0

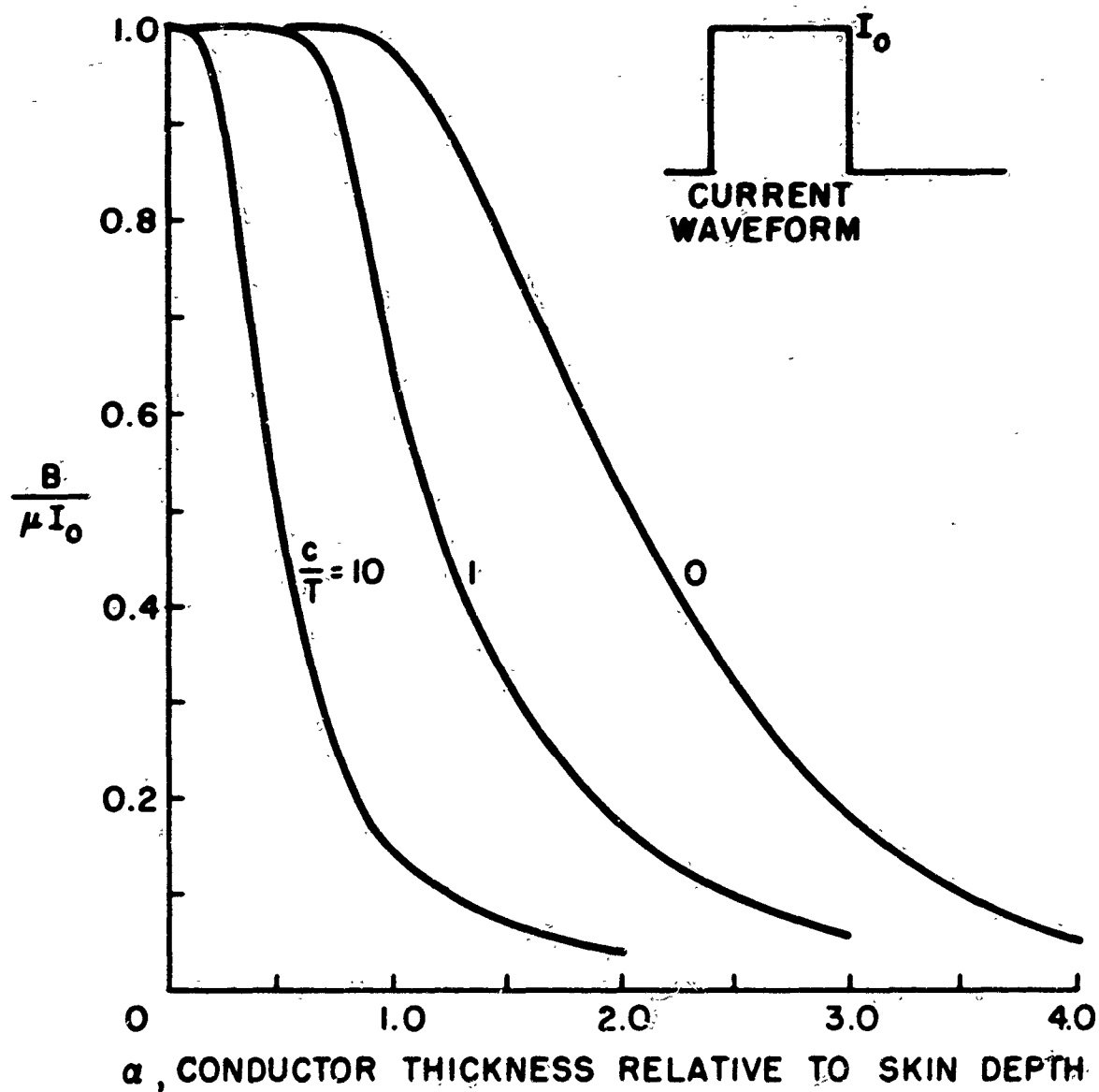a , CONDUCTOR THICKNESS RELATIVE TO SKIN DEPTH

Figure 4. Relative Peak Axial Magnetic Field as a Function of Conductor
Thickness for Rectangular System.

C. SOLUTIONS FOR CYLINDRICAL GEOMETRY

The use of cylindrical geometry in describing a pulsed solenoid system

is much more realistic than the rectangular geometry of the preceding

section, but the arithmetic associated with the cylindrical geometry is

far more complicated. The results of the preceding section provide a

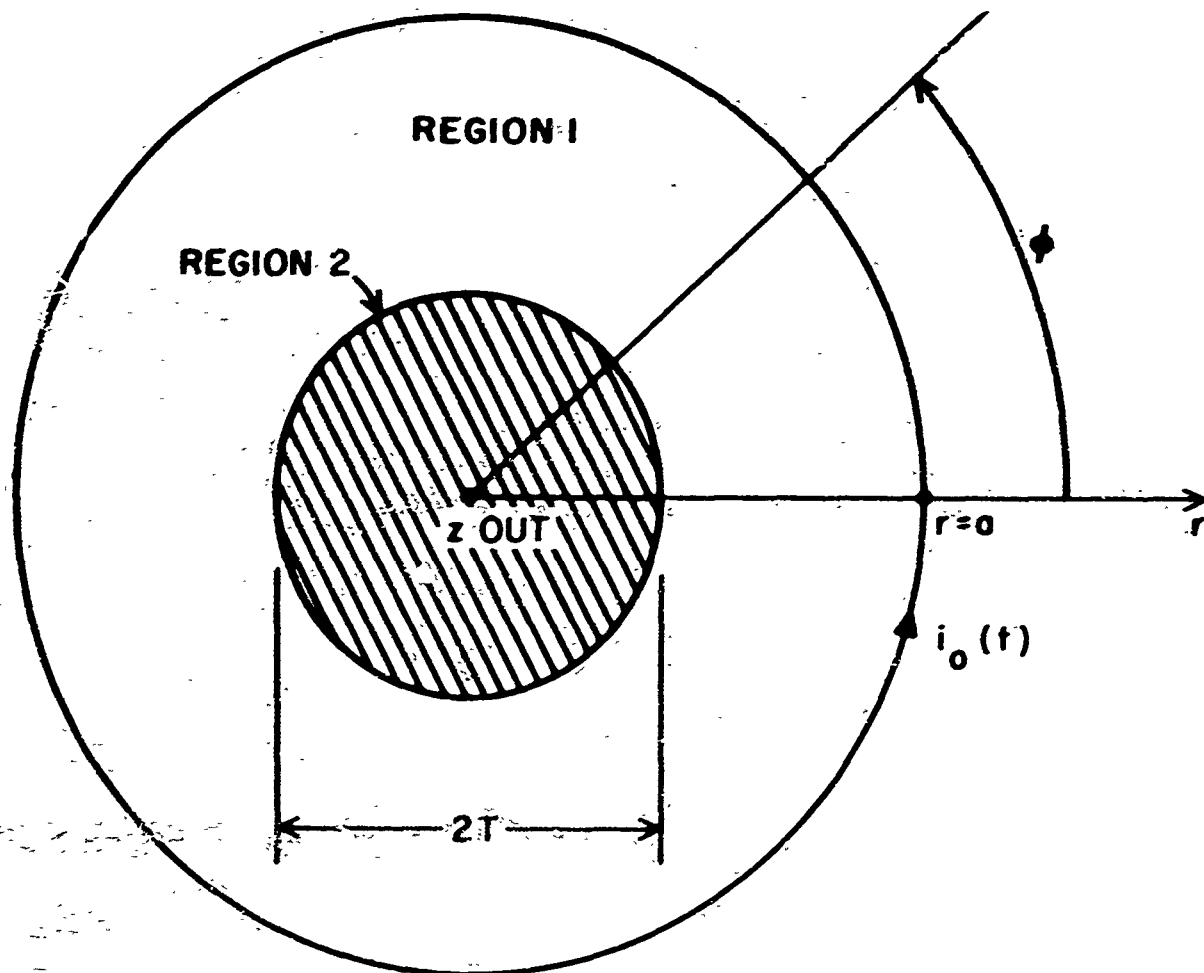useful guide, however, to the behavior that should be expected. Certainly

Figure 5. Schematic Structure of a Simple Pulsed Solenoid System in Cylindrical Co-ordinates.

the same basic expressions in Equation (8) apply, and we again assume nonmagnetic conductors and an ideal, infinitely long magnet system that is finite in the transverse direction.

Let us first examine a solid conductor system as shown in Figure 5. Assuming circular symmetry, the expressions corresponding to Equations (9), (10), and (11) that apply are as follows:

$$\left[\frac{1}{r} \frac{d}{dr} \left(r \frac{d}{dr} \right) - \gamma^2 \right] \beta_z = 0 \qquad (33.a)$$

$$\left[\frac{d}{dr} \frac{1}{r} \left(\frac{d}{dr} r \right) - \mathcal{T}^2 \right] \begin{bmatrix} e_\phi \\ i_\phi \end{bmatrix} = 0$$

(33.b)

$$\frac{1}{r} \frac{d}{dr} (r \, E_\phi) = - P \, B_z$$

(34.a)

$$\frac{d}{dr} B_z = - \mu \sigma E_\phi$$

(34.b)

where

$$\mathcal{T}^2 = \mu \sigma \, P$$

(35)

Appropriate choice of the conductivity σ makes it possible to distinguish between fields internal and external to the conductor.

Following the nomenclature and procedure of the preceding subsection gives two equations. For $0 < r < T$:

$$j_2 = - \frac{A \mathcal{T}}{\mu} I_1 (\mathcal{T} r)$$

(36.a)

$$e_2 = - \frac{A \mathcal{T}}{\sigma \mu} I_1 (\mathcal{T} r)$$

(36.b)

$$B_2 = A \, I_0 (\mathcal{T} r)$$

(36.c)

where solutions involving the modified Bessel function of the second kind are omitted because of a pole at $r = 0$. For $T < r < a$:

$$j_1 = 0$$

(37.a)

-17-

$$c_1 = -P\frac{rc}{2} + \frac{D}{r} \quad , \tag{37.b}$$

$$\beta_1 = c \quad . \tag{37.c}$$

Again, from the boundary conditions for the field within the conductor, one obtains

$$\beta_2 = \mu j_0 \ \frac{I_0(\Gamma r)}{I_0(\Gamma T)} \tag{38}$$

which should be compared with Equation (15) for the rectangular case.

For the rectangular current pulse, Equation (18) applies, and the inverse transform for the axial magnetic field readily gives

$$B_2(t) = \mu I_0 \left[1 - 2 \sum_{n=1}^{\infty} \frac{e^{-\frac{b_n^2 \pi}{2\alpha^2}(\frac{t}{t_0})}}{b_n J_1(b_n)} \right], \ 0 < t < t_0 \tag{39}$$

and

$$B_2(t) = f(t) - f(t - t_0), \qquad t > t_0 \tag{40}$$

where $f(t)$ is given by Equation (39). The new quantity b_n appearing in these equations is defined by

$$J_0(b_n) = 0, \qquad n = 1, 2, \dots \qquad . \tag{41}$$

Equation (39) should be compared directly with the equivalent form for rectangular geometry given by Equation (22). An expression comparable to Equation (23) that converges rapidly for small values of time is not readily obtained directly from Equation (39), since the Poisson summation formula is not easily applied.

If a half-sine-wave current pulse is assumed, Equation (24) applies, and gives for the axial magnetic field

$$B_2(t) = \mu I_0 I_m \left[\frac{e^{i\omega t}}{I_0(\alpha\sqrt{2i})} - 2 \sum_{n=1}^{\infty} \frac{b_n e^{-\frac{b_n^2 \pi}{2\alpha^2}\left(\frac{t}{t_0}\right)}}{J_1(b_n)\left(b_n^2 + i2\alpha^2\right)} \right] . \quad (42)$$

When the imaginary part is taken, Equation (42) becomes

$$B_2(t) = \mu I_0 \left[\frac{ber_0(\alpha\sqrt{2})\sin(\omega t) - bei_0(\alpha\sqrt{2})\cos(\omega t)}{ber_0^2(\alpha\sqrt{2}) + bei_0^2(\alpha\sqrt{2})} \right.$$

$$\left. + 4\alpha^2 \sum_{n=1}^{\infty} \frac{b_n e^{-\frac{b_n^2 \pi}{2\alpha^2}\left(\frac{t}{t_0}\right)}}{J_1(b_n)\left(b_n^4 + 4\alpha^4\right)} \right] \quad (43)$$

where

$$I_0(\alpha\sqrt{2i}) = ber_0(\alpha\sqrt{2}) + i\, bei_0(\alpha\sqrt{2}) \quad . \quad (44)$$
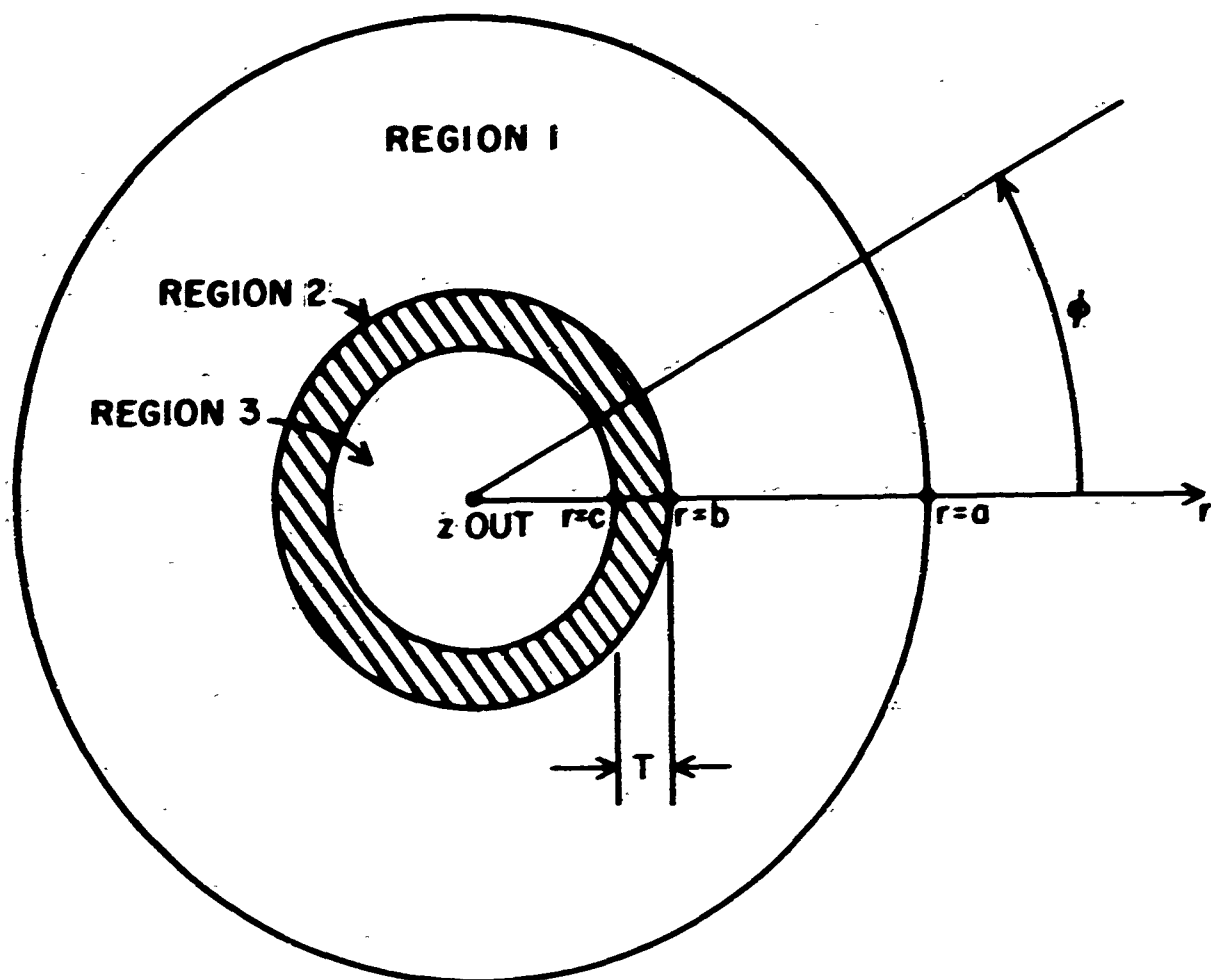
Figure 6. Schematic Structure of a Pulsed Solenoid with a Thin-Walled. Conductor in Cylindrical Co-ordinates.

The result in Equation (42) applies for $0 < t < t_o$, whereas for $t > t_o$ the form for Equation (27) applies.

A pulsed solenoid system with a hollow conductor is shown in Figure 6. The solution for this system for the axial magnetic field becomes very complex in detail, but the form of this solution is readily established. For region 1 where $b < r < a$, Equation (37) expresses the field transform. In region 2, for $C < r < b$, one obtains:

$$j_2 = - \frac{\Gamma}{\mu} \left[A\, I_1(\Gamma r) - B K_1(\Gamma r) \right]$$

(45.a)

$$e_2 = - \frac{\tau}{\sigma\mu} \left(A \, I_1(\tau r) - BK_1(\tau r) \right) \qquad (45.b)$$

$$\beta_2 = AI_0(\tau r) + BK_0(\tau r) \qquad ; \qquad (45.c)$$

In region 3, for $0 < r < c$, one obtains:

$$j_3 = 0 \qquad (46.a)$$

$$e_3 = - P \frac{r}{2} G \qquad (46.b)$$

$$\beta_3 = G \quad . \qquad (46.c)$$

Again using the boundary conditions that the tangential field components

are continuous across the boundaries, we find

$$\beta_3 = \mu j_0 \quad \frac{\left[I_0(\tau c)K_1(\tau c) + I_1(\tau c)K_0(\tau c) \right] \tau \sqrt{bc}}{b\cosh(\tau T) + (\frac{\tau c}{2}) \, b\sinh(\tau T)} \quad . \qquad (47)$$

In this expression the Bessel hyperbolic sine and cosine functions are

as follows:

$$b\cosh \left[\tau(b-c) \right] = \tau\sqrt{bc} \left[I_0(\tau b)K_1(\tau c) + I_1(\tau c)K_0(\tau b) \right] \qquad (48.a)$$

$$b\sinh \left[\tau(b-c) \right] = \tau\sqrt{bc} \left[I_0(\tau b)K_0(\tau c) - I_0(\tau c)K_0(\tau b) \right] \quad . \qquad (48.b)$$

In the limit of large arguments, the Bessel hyperbolic sine and cosine

functions asympotically approach the circular hyperbolic functions.

Also for large arguments the numerator of Equation (47) approaches one.

Thus, for a hollow conducting cylinder with a large diameter, Equation (47) approaches the form of Equation (29) from the rectangular geometry solution.

The time behavior of the axial magnetic field from Equations (39) and (40) for the cylindrical case with solid conductor is very similar to that for the rectangular case illustrated in Figure 3; that is, the maximum magnetic field still occurs at the end of the current pulse for the rectangular current pulse. A comparison of the maximum axial magnetic fields between the solid cylindrical and rectangular cases, for a rectangular current pulse is shown in Figure 7. The corresponding results for the hollow cylindrical case from Equation (47) have not been calculated. The small amount of additional information obtained from this expression does not seem to warrant the gross additional complexities in calculating the inverse transform. It is expected that the peak axial magnetic field for this situation will decrease about as rapidly compared to the cylindrical solid case as for the corresponding situation in rectangular geometry shown in Figure 4.

Finding the peak axial magnetic field for the half-sine-wave current pulse is not as simple as for the rectangular pulse, since the field peak is delayed from the current peak. In addition, the amount of delay is a function of the conductor thickness measured in terms of the skin depth. A few plots of the time behavior of the axial field for the solid conductor from Equation (43) are shown in Figure 8. Figure 9 shows a comparison between the rectangular and half-sine-wave current pulses for the solid conductor in cylindrical co-ordinates.
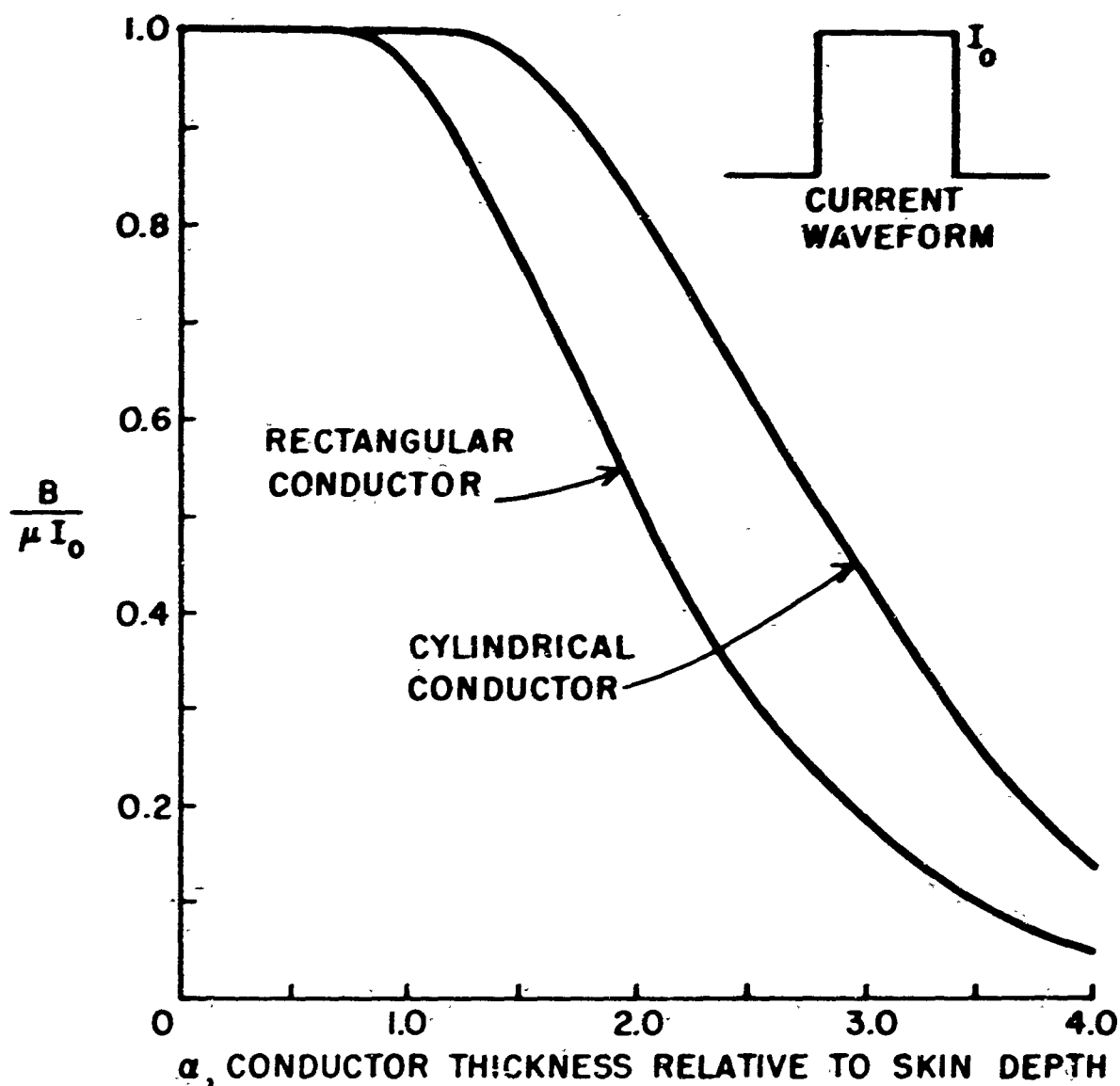
Figure 7. Comparison of Axial Magnetic Fields for Solid Rectangular and Cylindrical Geometries.

It is interesting to observe from Figure 8 that the axial magnetic field is initially negative for sufficiently thick conductors. This simply means that for a given conductor thickness and for a fast enough rise time for the primary magnetic field produced by the current pulse, the secondary magnetic field produced by the integrated effects of the induced currents is momentarily larger than the primary magnetic field. The range of conductor thicknesses for which this occurs may be found
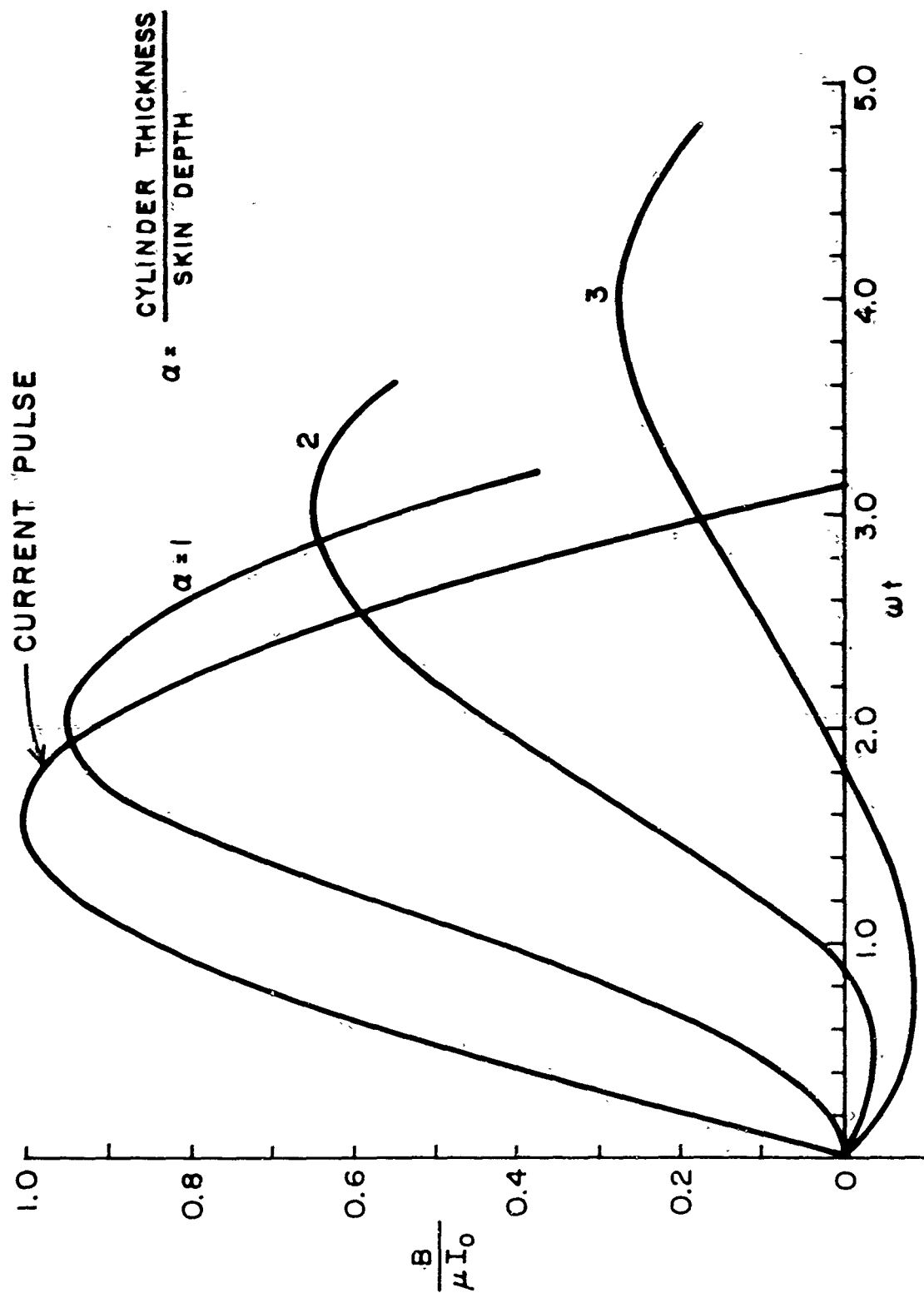
Figure 8. Axial Magnetic Field versus Time for Solid Cylindrical Conductor with Half-Sine-Wave Current Pulse.
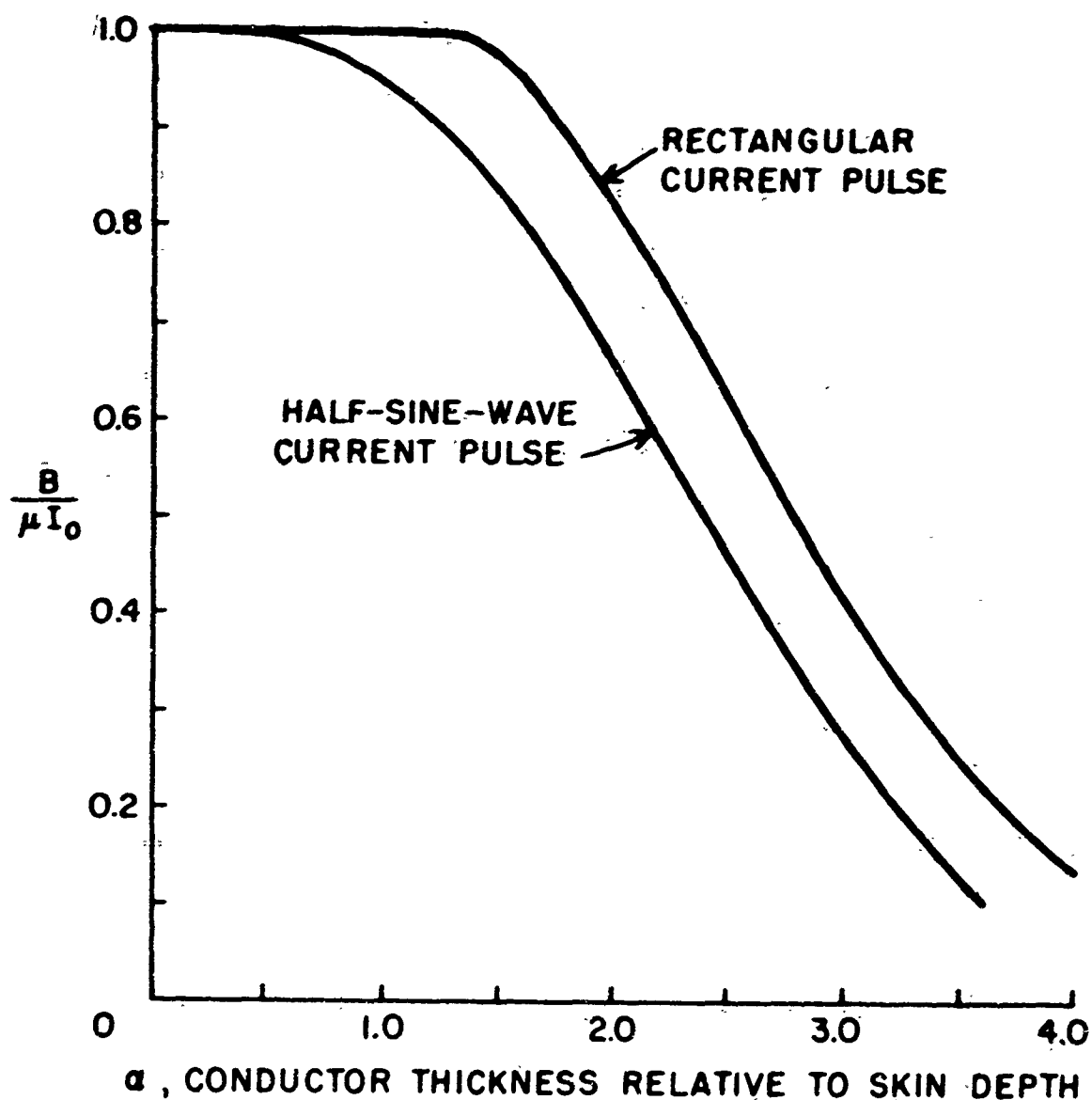
-24-

Figure 9. Comparison Between Current Waveforms for Axial Magnetic Field of Solid Cylindrical Conductor.

from Equation (43). The series in this equation is alternating since $J_1(b_n)$ is an alternating function. In addition the magnitude of the individual terms is monotonically decreasing. When the magnetic field is negative near $t = 0$, the derivative will also be negative; and for positive fields the derivative will be positive. Thus, an estimate of the value of α required to obtain a momentary negative field is found

by setting the derivative of Equation (43) equal to zero, and using only the first term of the series; giving

$$\frac{dB_2(0)}{dt} = 0 = \frac{ber_0\left(\alpha\sqrt{2}\right)}{ber_0^2(\alpha\sqrt{2}) + bei_0^2(\alpha\sqrt{2})} - \frac{2\pi b_1^3}{J_1(b_1)(b_1^4 + 4\alpha^4)} .$$

(49)

and therefore, $\alpha = T/\delta \approx 1.1$. For this and larger values of α, the axial magnetic field is initially negative.

D. DIFFUSION EFFECTS IN SOLENOID

In all the models of the pulsed solenoid system examined so far, the assumption that the pulsed solenoid itself could be represented as a current sheet has been used. However, if the solenoid is sufficiently thick, the magnetic field produced must diffuse through the metallic solenoid to appear inside the solenoid. The decrement in axial magnetic field in this instance will not be as serious as for a passive conductor of the same configuration for two reasons:

1. The solenoid is not solid but consists of layers of wire or tape with insulation and air gaps between layers.

2. The magnetic field produced by the outer layer must diffuse through the entire solenoid, but the magnetic field produced by the inner layer must only diffuse through itself.

The effect on the axial magnetic field may be established from the preceding results in the following way. Consider a solenoid of equivalent

thickness T in the form of one of the conductors treated earlier. Suppose that this solenoid has no passive conductor placed on its axis. Then the pulse current per unit width is approximately $i_o(t)/T$. If the axial magnetic field produced by a current shell of $i_o(t) \frac{\Delta T}{T}$ is denoted by $B(t,T)$, the total field produced by the complete solenoid is

$$B_s(t) = \int_0^T B(t, u) \, du \qquad (50)$$

for either the rectangular or the cylindrical geometry.

To provide as accurate an estimate of this effect as possible, the results for the cylindrical geometry case with hollow conductor should be used in Equation (50). As discussed briefly in Section C, however, this case is so complex in detail that the calculation was not performed. Of the other cases, perhaps the best ones to consider in estimating the diffusion effect of the magnetic field through the solenoid are the hollow rectangular geometry and the solid cylindrical geometry. The first of these treats a hollow conductor while the second shows the effects of the cylindrical geometry.

For the hollow rectangular geometry, consider the situation where C/T is large. Equation (32) describes the axial magnetic field, and from Equation (50),

$$B_s(t) = \mu I_o \left\{ 1 - e^{-\frac{T}{C} \frac{\pi}{2\alpha^2} \left(\frac{t}{t_o}\right)} - \frac{T}{C} \frac{\pi}{2\alpha^2}\left(\frac{t}{t_o}\right) E_1\left(-\frac{T}{C} \frac{\pi}{2\alpha^2} \frac{t}{t_o} \right) \right.$$

$$- \sum_{n=1}^{\infty} \frac{(-1)^n}{\frac{n^2\pi^2 C}{T}} \left[e^{-\frac{n^2\pi^3}{2\alpha^2}(\frac{t}{t_o})} + \frac{n^2\pi^3}{2\alpha^2}(\frac{t}{t_o}) E_i(-\frac{n^2\pi^3}{2\alpha^2}\frac{t}{t_o}) \right] \Bigg\} \quad . \quad (51)$$

For the solid cylindrical geometry, Equation (39) applies, and

$$B_s(t) = \mu I_o \left\{ 1 - 2 \sum_{n=1}^{\infty} \frac{1}{b_n J_1(b_n)} \left[e^{-\frac{b_n^2 \pi}{2\alpha^2}(\frac{t}{t_o})} - \frac{b_n \pi}{\sqrt{2}\alpha} \sqrt{\frac{t}{t_o}} \; \text{Erfc} \left(\frac{b_n}{\alpha} \sqrt{\frac{\pi t}{2t_o}}\right) \right] \right\} \quad . \quad (52)$$

For both Equations (51) and (52) the rectangular current pulse was used.
A comparison between the results in Equations (51) and (52) and those for
a passive conductor is made in Figure 10.

E. SUMMARY AND EVALUATION OF CALCULATIONS

The behavior of the decrease in the axial magnetic as a function
of the different geometries is readily explained in terms of the induced
currents with the conductors inserted within the solenoids. For the
rectangular geometry and the rectangular current pulse, the magnetic
field is affected the least for the solid conductor; then as the width
of the hollow conductor increases, the magnetic field decreases further
and further. This is readily understood by realizing that the induced
current in the solid conductor is zero on the axis; whereas for a hollow
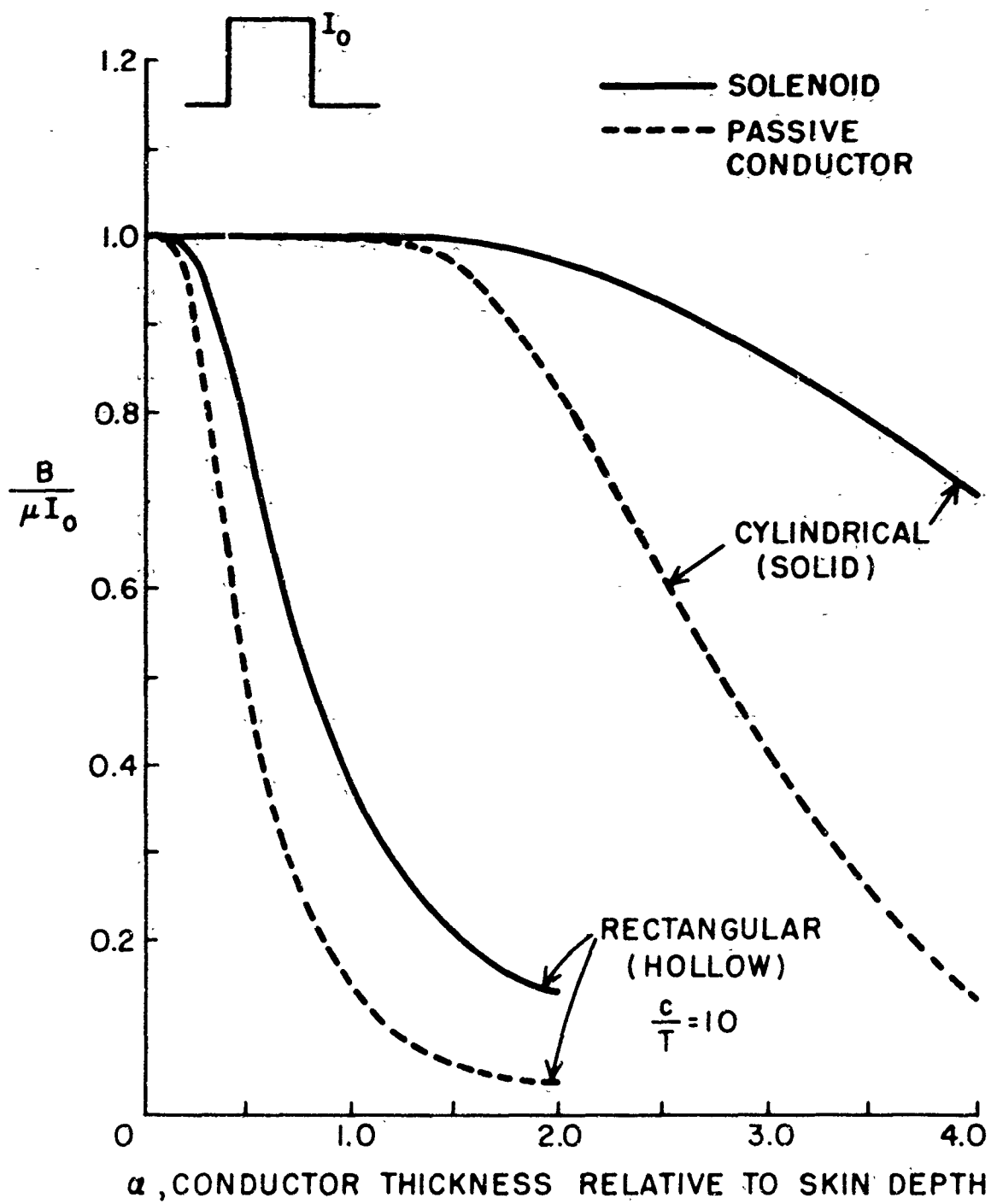conductor of the same thickness, the induced current on the inner wall

Figure 10. Comparison of Magnetic Field Through Solenoid and Passive Conductor of Same Thickness.

is not zero. As a result the total opposing magnetic field produced by
the induced currents is larger for the hollow conductor than for the solid.
A similar argument applies to the solid and hollow conductors in the
cylindrical geometry.

Comparison of the solid conductor cases in rectangular and cylindrical
geometries shows that the magnetic field decreases more slowly for the
cylindrical geometry. This is expected on the basis that as a result of
the curvature in the cylindrical geometry, the induced current decreases
more rapidly towards the conductor center than it does for the rectangular
geometry. This same behavior should be evident for the hollow conductor
cases until the diameter of the conductor becomes very large compared to
its width. In this event the curvature at the conductor is only slight,
and there will be little difference in the magnetic field calculated from
the rectangular or cylindrical geometry.

An estimate of the decrease in magnetic field for the hollow cylin-
drical conductor can be obtained for the rectangular current pulse by
scaling the results in Figure 4 to those given in Figure 7. Such scaling
will tend to give a low estimate, since in the limit of large radius-to-
thickness ratio (C/T) both the rectangular and cylindrical geometries
will give similar results, as discussed in the previous paragraph.

The results for the half-sine-wave current pulse follow the same
trend with geometry as does the rectangular current pulse. The peak
value of magnetic field for a given peak value of current, however, is
slightly smaller than for the rectangular current pulse because the peak

current is maintained during the rectangular pulse. The most notable
difference is in the long time delay between the current and magnetic
field peaks. Of secondary interest is the momentarily negative magnetic
fields for sufficiently thick conducting described in the Section C.
Estimates of the peak magnetic fields for the hollow cylindrical conductor
are readily obtained by scaling of the results in Figures 4, 7, and 9.

The effect of magnetic field diffusion through the solenoid is not
nearly as serious as through a passive conductor as illustrated in Figure
10. The reason for this is discussed in Section C. A rough but workable
estimate of the decrease in the axial magnetic field for the hollow
cylindrical geometry can be obtained by applying the correction shown
in Figure 10. The results in Figure 10 for the cylindrical case will give
a low estimate because of the solid conductor.

It should be realized that a complete picture of the axial field
behavior in the cylindrical case even for an infinitely long structure
requires one step beyond those presented here. A hollow finitely thick
solenoid should be considered, and the field resulting from this should
be used as the exciting field for the expressions in Equations (37), (45),
and (46). The resulting expressions, however, are very complex and
unwieldly, which is the reason for the piecemeal approach presented here.
The complete problem of the finitely thick solenoid with a hollow
cylindrical conductor is perhaps best left for a computer solution, where
end effects could be included if desired. Without resorting to a computer
solution, the simple calculations made here give quantitative results
sufficiently accurate for a practical design.

III. DESIGN OF PULSED SOLENOIDS

The actual design of a pulsed solenoid is straightforward, but it involves a little trial and error. The exact starting point depends on what information is known and what must be determined; e.g., a particular pulse current supply may already be available. The following quantities are pertinent to the design:

B = peak axial magnetic field desired,

B_o = peak axial magnetic field for d-c excitation,

N = number of turns per inch for the solenoid,

I_o = peak solenoid current in amperes,

t_o = pulse current length,

L_s = self-inductance of the solenoid,

C = equivalent capacity of the pulse circuit,

V_o = charging voltage for the pulse current supply,

R = equivalent series resistance of the pulse circuit,

f = natural resonant frequency of pulse circuit,

1 = length of solenoid in inches.

It is assumed that the equivalent circuit of the solenoid and the current pulse supply is as shown in Figure 11. For this case the results for the half-sine-wave current pulse are appropriate.

In general, the design procedure is as follows. The peak axial magnetic field desired would be known and the time duration of the pulse would also be known on the basis of the intended use of the field; that is, only a small region of the magnetic field pulse is usable depending on the requirements for field variation with time. Thus, B and t_o are

R

**INITIALLY
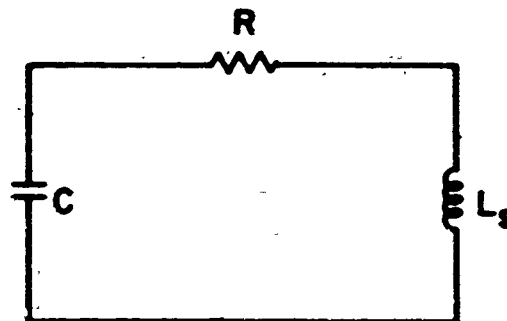CHARGED
TO V_o**

C

L_s

Figure 11. Equivalent Circuit of Pulsed Solenoid and Power Supply.

fixed, which in turn fixes the resonant frequency of the circuit in Figure
11 by

$$f = \frac{1}{2t_o} \quad .$$

(53)

If the details of the conductor to be inserted in the solenoid are known;
i.e., dimensions and material, the decrease in the peak magnetic field
resulting from diffusion effects is readily estimated from Figures 4, 7,
and 9. As an aid in this process, the skin depth as a function of frequency,

$$\delta = \sqrt{\frac{1}{\pi f \mu \sigma}}$$

(54)

ir shown for copper and stainless steel in Figure 12. Then, as a first
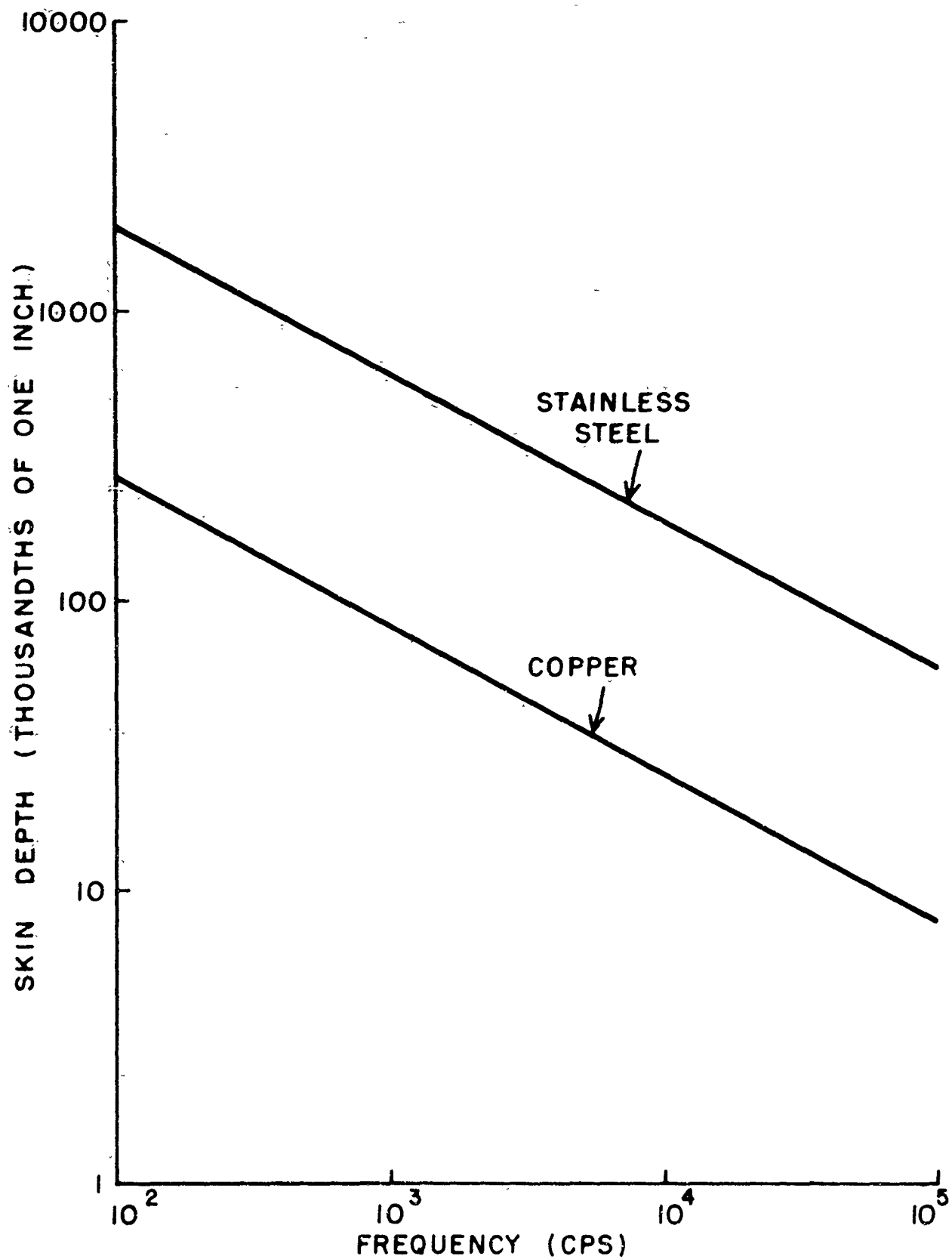estimate 10 - 15 per cent could be taken as the decrease in magnetic field

Figure 12. Skin Depth versus Frequency for Copper and Stainless Steel Conductors.

$$B_o = \frac{N\,I_o}{2} \quad \text{gauss} \quad . \tag{55}$$

Also, the self-inductance of the solenoid is found from the power supply capacitance by

$$L_s = \frac{t_o^2}{n^2 C} \quad . \tag{56}$$

The peak solenoid current is related to the charging voltage V_o approximately as follows:

$$I_o \approx e^{-\frac{R t_o}{4 L_s}} \; \frac{V_o}{\omega_o L_s} \tag{57}$$

where it is assumed that the circuit resistance is sufficiently small that it does not affect the resonant frequency. If this is not the case, Equation (53) fixes the frequency, but Equation (56) must be replaced by

$$f^2 = \frac{1}{2\pi L_s C} \; \left(1 - \frac{R^2 C}{4 L_s}\right) \tag{58}$$

and the maximum current is calculated from

$$i_o(t) = e^{-\frac{R t}{2 L_s}} \; \left(\frac{V_o}{\omega L}\right) \quad \sin \omega t \quad . \tag{59}$$

All of the auxiliary information is now known about the solenoid except for its dimensions and number of turns. The turns per inch N can be found from Equation (55), and the self-inductance can be related to the dimensions (see page 443 of Reference 1) as follows

$$L_s = \frac{a^2 \, N^2 \ell^2 \, 10^{-6}}{9a + 10\ell + 8.4T + 3.2 \frac{T\ell}{a}} \tag{60}$$
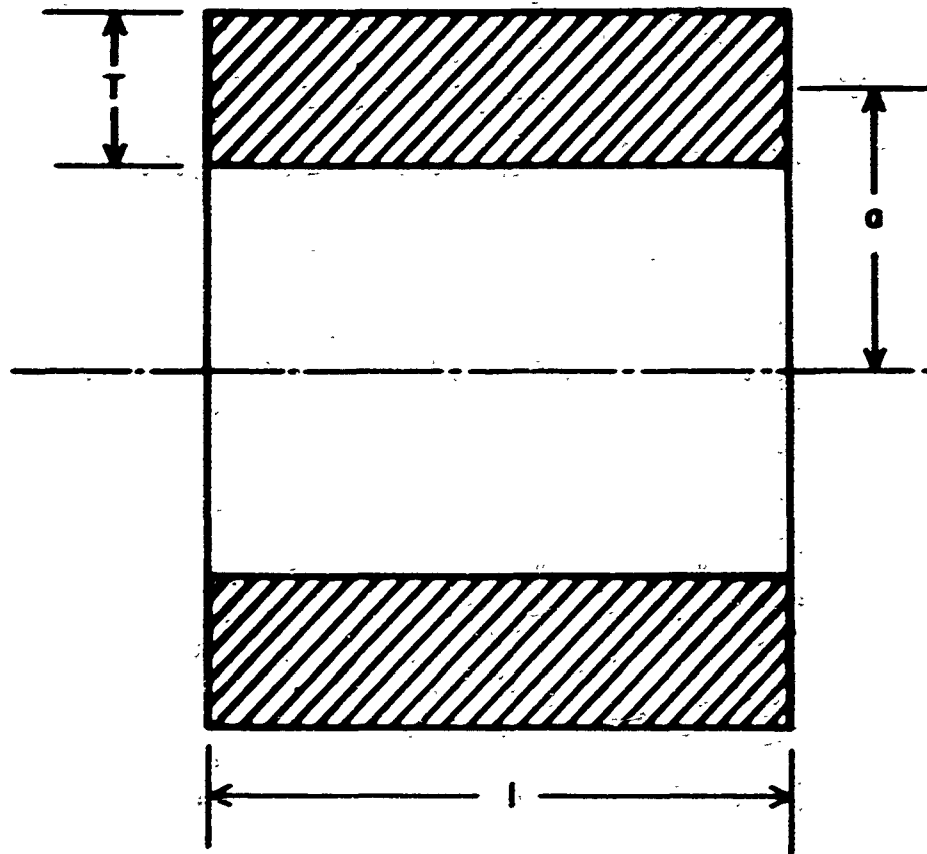
-35-

Figure 13. Dimensions of Pulsed Solenoid.

where the dimensions are defined in Figure 13. This expression applies where the coil diameter is less than three times the length. A trial-and-error procedure is required at this point to yield a consistent set of values for N and L_s. Once this is done the results in Figure 10 can be used to give a better estimate of the decrease in magnetic field resulting from diffusion effects within the solenoid, and an appropriate change in the charging voltage V_o can be determined.

It is possible to increase the available axial magnetic field for a given coil inductance by using a Helmholtz coil arrangement. In this case the past results apply except that the total inductance of the two coils in series must account for the mutual inductance between the coils.

The coupling coefficient for various spacings between the two coils is given on page 447 of Reference 1.

If the solenoid is to be operated on a low duty cycle it is possible to apply very large peak pulse currents. As an example, peak currents of up to 3300 amperes have been applied using no. 14 copper wire for a single-shot solenoid. This is twenty times larger than the approximate fusing current for this wire listed on page 55 of Reference 2.

One other aspect of the solenoid design which has not been considered is the mutual inductance between the pulsed solenoid and the conductor on its axis. It is possible to calculate this effect from the results of Section II, where this appears in terms of an electric field acting on the solenoid to produce an added current component. However, this effect has been neglected for the calculations presented here.

IV. EXPERIMENTAL RESULTS

For purposes of comparison with some of the calculated results, a simple solenoid was constructed. This consisted of 165 turns of no. 14 enameled copper wire wound on a 7/8-in. bakelite form. The wire was wound in 5 rows to give a total winding length of 2.2 in. The nominal winding thickness was 0.335 in. This solenoid had approximately a one-inch working length and an inner diameter of 3/4 in. The turns per inch were calculated as

$$N = 75 \text{ turns/in.}$$

The inductance for this coil calculated from Equation (60) was 291 μh. This coil was to be used with a pulsed power supply whose nominal capacitance was 360 μf, which from Equation (58) gave a ringing frequency of approximately 491 cps. This meant a half-period duration of 1.02 msec. The resistance of the coil was not calculated since it would be small compared to the equivalent power supply resistance, for only low-Q capacitors were available for the supply.

A schematic of the supply used for testing the coil is shown in Figure 14.[*] The rated maximum voltage which can be initially applied to the storage bank is 3000 V. A special feature of this supply is the provision for quenching the output current at the end of the first half-cycle of oscillation, so that the output current does not simply decrease to zero after oscillating for a number of cycles at the ringing frequency.

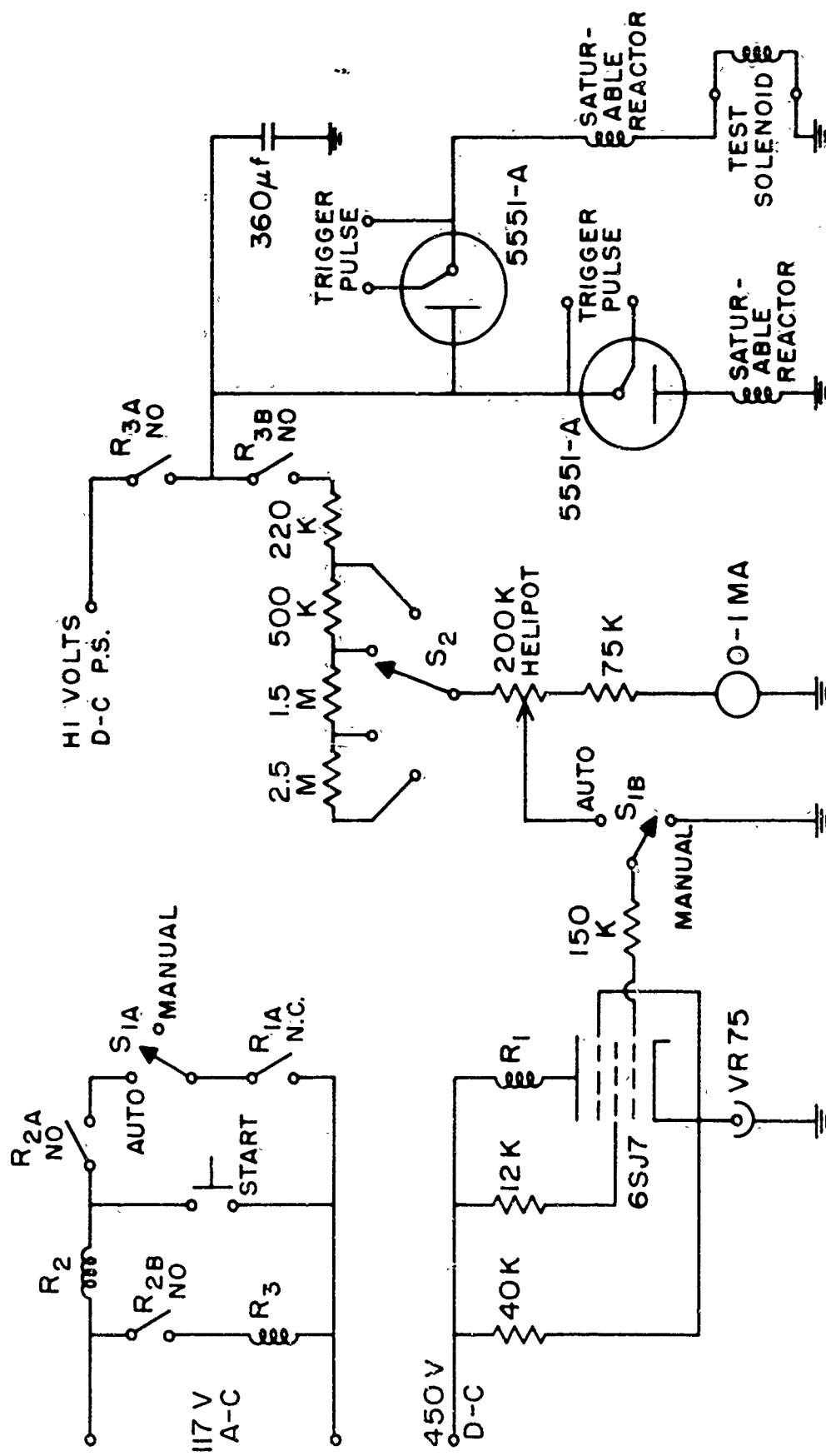[*]This circuit was designed and developed by D. M. Stevenson.

Figure 14. Schematic of Pulse Current Supply for Pulsed Solenoid.
(Circuit Designed by D. M. Stevenson).

The pulsed solenoid current was monitored with a series resistance in the form of a stainless steel strap with appropriate voltage indicating points attached. With a d-c bridge the resistance of this strap between indicating points was measured to be 0.0129 Ω.

The pulsed magnetic field was measured with a small search coil attached to a simple integrating circuit as shown in Figure 15. Using the measured values of resistance and capacitance gave a calibration factor of 0.915 mv/kgauss for the device. It should be observed that the integrating circuit should have a time constant long compared to the magnetic field pulse, if an accurate indication of the field pulse as a function of time is to be obtained. For the circuit in Figure 15 this time constant is approximately 0.1 sec, which is much longer than the 0.001-sec. field pulse.

An estimate of the degradation in the peak axial magnetic field can be made as follows. Estimate the equivalent thickness of the solenoid windings on the basis of the cross-sectional area of the wires alone; i.e., the area given by considering an area of solid copper equal to the area of sum of the round copper wires. The wire diameter for no. 14 wire is 0.064 in. Thus, the cross-sectional area of one-half the solenoid is

$$A = \frac{\pi}{4} (.064)^2 165 = 0.531 \text{ in}^2.$$

For a solid mass of copper, the same area is obtained by a thickness given by
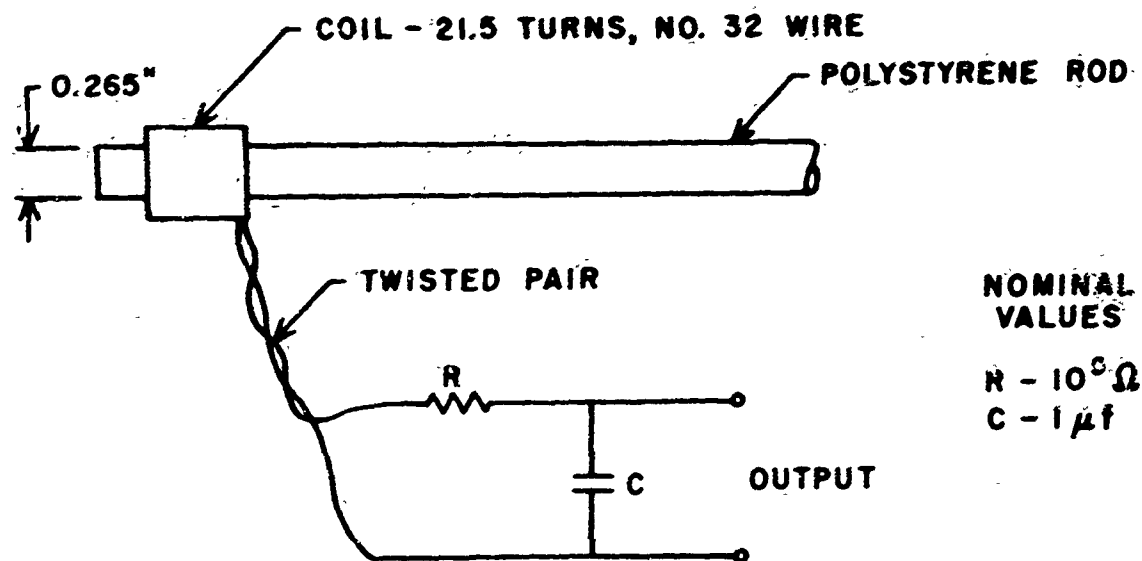
$$T = \frac{0.531}{2.2} = 0.241 \text{ in.}$$

Figure 15. Schematic of Circuit to Measure Pulsed Magnetic Field.

where the winding length of 2.2 inches is used. From Figure 12 the skin depth for copper at 500 cps is approximately 0.120 in.; therefore

$$\frac{T}{\delta} = \alpha = 2.0$$

for the solenoid, and

$$\frac{C}{T} = \frac{0.437}{0.241} = 1.85 \quad .$$

With these parameters, the ratio obtained from Figure 4 of actual to ideal magnetic field for a passive rectangular conductor is approximately 0.16. If this is scaled to the passive cylindrical case by using Figure 7 this ratio becomes approximately 0.41. Then, using Figure 10 to estimate the affect for the solenoid rather than a passive conductor, gives the value of 0.86. These values are for a rectangular current pulse. The peak magnetic field should be decreased slightly from this value for a half-sine-wave current pulse, but it is not clear that this

should scale directly from Figure 9. Consequently, the rough estimate of a 15 per cent decrease in the peak magnetic field from ideal conditions is obtained for the test solenoid.

After the preceding simple design calculations, the solenoid was prepared for testing. Bakelite end plates were glued to the central form to contain the wire; and the loose ends of the coil were epoxied to these end pieces. This simple construction has withstood the magnetic forces experienced by the coil under pulsed magnetic field operation. To check the inductance calculation, the coil was measured with a 1000-cps bridge and the series inductance was 299 μh. This value was about 2.7 per cent higher than the calculated value of 291 μh.

Typical data for the solenoid current and axial magnetic field are shown in Figure 16. The pulse length is approximately 10 per.cent longer than calculated, probably as a result of using the rated capacity rather than the measured capacity of the power supply for the calculations. From the data in Figure 16 the peak current is found to be 1630 a, and the peak magnetic field is 50.2 kgauss. For this peak current the ideal magnetic field from Equation (55) is calculated to be 61.1 kgauss. Thus the experimental decrease of the axial magnetic field resulting from diffusion effects in the solenoid is found to be 17.8 per cent as compared to the rough theoretical estimate of 15 per cent. This measurement indicates that the scaling techniques used to obtain the theoretical estimate of the decrease in the magnetic field are sufficiently accurate for design purposes.

Another simple test was performed with this pulsed magnet to measure experimentally the effect of the magnetic field diffusion through a passive conductor. A hollow brass cylinder, with an outer diameter of 0.75 in. and a wall thickness of 0.105 in. was inserted in the solenoid. Since the resistivity of brass is approximately 3.9 times that of copper (p.45 of Reference 2), the skir depth in brass at 500 cps is

$$\delta = 0.12 \ \sqrt{3.9} = .237 \ \text{in.}$$

and, the parameters for this brass cylinder are

$$\alpha = T/\delta = \frac{0.105}{0.237} = 0.443$$

$$\frac{C}{T} = \frac{0.270}{0.105} = 2.57 \quad .$$

From Figure 4, or Equation (30), the ratio of actual to ideal magnetic field is 0.9 for a hollow rectangular conductor. Scaling to a cylindrical conductor by means of Figure 7 shows that the curve for the cylindrical conductor is just at its knee for this value on the curve for the rectangular conductor (an equivalent α of 1.2 for the solid cylindrical case). Then accounting for the half-sine-wave current waveform from Figure 9 gives a final estimate of 0.90 - 0.91 for the magnetic field ratio. Thus, this scaling technique gives the estimate of a decrease of 9 - 10 per cent in the peak axial magnetic field for the test solenoid when the brass cylinder is placed inside the solenoid. From the discussion of

Section II, this estimate should be somewhat conservative, although it
is not known by how much.

Data comparing the axial magnetic field with and without the brass
cylinder is shown in Figure 17. The peak magnetic field with the brass
cylinder is 43.9 kgauss which corresponds to a 12.5 per cent decrease
with respect to the field without the cylinder. This compares favorably
with the conservative theoretical estimate of a decrease of 9 - 10 per
cent. The data shown in Figure 17 are interesting for other reasons.
First, the current waveform when the brass cylinder is inside the solenoid
is markedly skewed. This is apparently a result of the interaction of
the conductor upon the solenoid. Also the axial field is extended in time
beyond the end of the current pulse, and the magnetic field begins with
a zero or slightly negative slope. This behavior is qualitatively pre-
dicted in Figure 8. In view of the approximate effective value of 1.2
for α as estimated earlier in the solid cylindrical case, the quantitative
behavior agrees well with that calculated. The delay in the peak magnetic
field with respect to the actual current peak is approximately one in
5.5 parts, as shown in Figure 17, while the delay shown in Figure 8 is
approximately six in 31.4 parts. Also, from Equation (49) the value
for α estimated as describing the transition between positive and negative
values for the magnetic field at the beginning of the pulse is 1.1.

The experimental results seem, therefore, to fit the theoretical
values when scaling techniques are used to go from the rectangular to
the cylindrical geometries. Of course, the data presented here are much
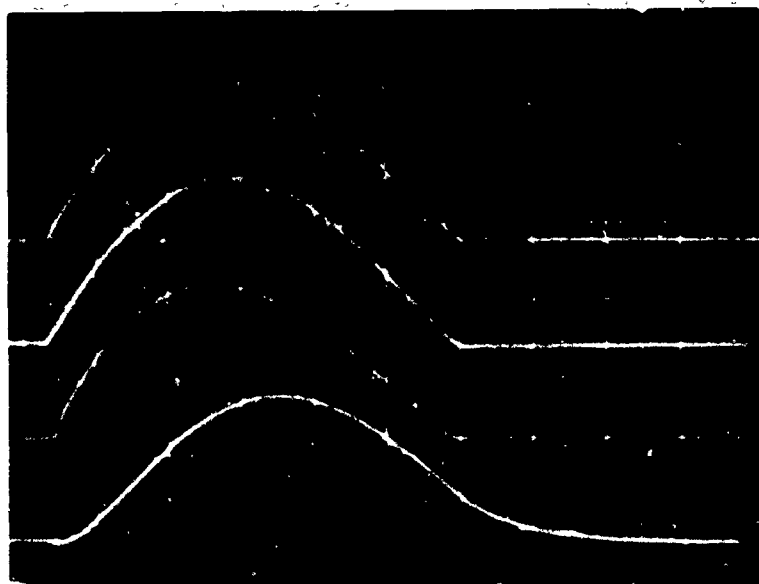
776 a/div.

22.8 kgauss/div.

HORIZONTAL SCALE : 200 μs/div.

Figure 16. Current and Axial Magnetic Field for Test Solenoid.

776 a/div.

22.8 kgauss/div.

776 a/div.

22.8 kgauss/div.

HORIZONTAL SCALE: 200 μs/div.

Figure 17. Current and Axial Magnetic Field for Test Solenoid.
Top Two Traces Without Brass Cylinder, Bottom Two
Traced with Brass Cylinder.

too meager to justify the statement that the theory agrees with experiment for the effects of magnetic field diffusion in pulsed solenoids. At this point, the best one can say is that the indications are that such an agreement exists.

Finally, some data were taken with the test solenoid and the particular power supply considered here to see what ultimate fields could be obtained. Under these conditions the initial voltage was 4.1 kv and the solenoid current was 3300 a. The measured magnetic field without the conducting cylinder was 102 kgauss. The pulse shapes for the current and magnetic field agreed with those shown in Figure 10.

V. CONCLUSIONS

The limited experimental results obtained for test solenoids indicate that the quantitative results obtained are sufficiently accurate for the design and construction of pulsed solenoids. The calculation of the decrease in magnetic field on the axis of a pulsed solenoid have shown that the conductor thickness (on the radius) which can be tolerated without a large degradation in the magnitude of the field is on the order of one skin depth. If low-conductivity conductors are used, this limitation is not especially serious. On the other hand, a much more stringent limitation is placed upon the coil thickness of the pulsed solenoid where copper wire or tape would be used. For a decrease of 10 - 15 per cent in axial field, coil thickness of up to twice the skin depth can be used. As the coil thickness is increased beyond this, the ratio of the axial magnetic field to the ideal field decreases very rapidly.

It is significant that pulsed magnetic fields as high as 100 kgauss were readily obtained with an inexpensive solenoid, although field uniformity was not high.

VI. REFERENCES

1. F. Langford-Smith (ed.), Radiotron Designer's Handbook, Harrison, New Jersey: RCA, 1953.

2. ITT, Reference Data for Radio Engineers, New York, 1949.

HIGH CURRENT-DENSITY BEAMS USING INDIRECT EMISSION
FROM LASER-IRRADIATED CATHODES

D. M. Stevenson

ABSTRACT

An experimental study was made of the emission of electrons from one side of a thin tungsten ribbon when heated by laser irradiation from a pulsed ruby laser incident on the opposite side. The emission obtained in this way was found to be repeatable up to current densities of 400 a/cm^2. Beams with this current density and diameters of 0.005-in were focused using magnetically confined flow in a pulsed magnetic field. The optical properties of tungsten and beam focusing using magnetic fields are discussed.

TABLE OF CONTENTS

LIST OF ILLUSTRATIONS

BLANK PAGE

I. INTRODUCTION

One of several limitations on high-power, high-frequency electronic devices is that conventional thermionic cathodes, when operated for reasonable lifetimes, give maximum emission densities of about 10 a/cm^2 and an order of magnitude greater when operated under certain conditions. Greater beam current densities than this can be produced by convergence, but at the expense of increasing the temperature of the beam and therefore the noise. There is also a limit to the convergence ratio that can be achieved in practice. A high emission density source could therefore be of considerable importance.

Such a source has been realized on a pulsed basis by irradiating tungsten with the high-intensity radiation produced by a ruby laser. The emission obtained in this way has been investigated and reported by Giori et al.[1] Figure 1 shows the laser pulse as detected by a photomultiplier tube together with the corresponding electron emission for several laser energies as observed by these workers. The laser pulse was of 300 µs duration and consisted of approximately one-hundred separate pulses or "spikes" each of less than 1 µs duration with two or three microseconds between the spikes. This spiking pattern can be best seen in Figure 2. When pulsed at constant input energy, the output energy of each pulse was constant, but the details if the spiking pattern were not.

The electron emission shown in Figure 1 was obtained by focusing the laser beam to a spot of approximately 0.002 in. diameter on the
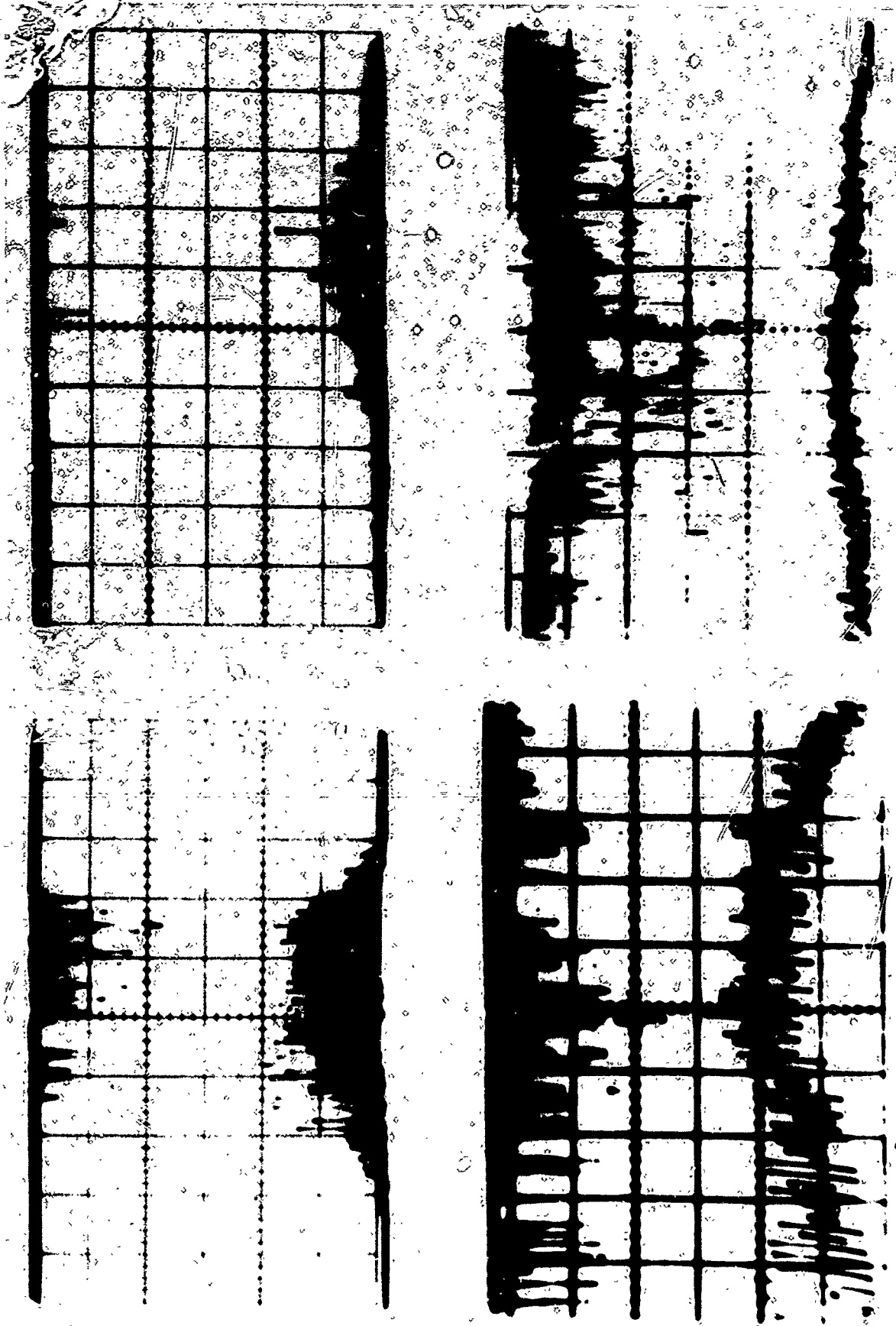
Figure 1. Laser Pulses Detected by Photomultiplier Tube (Lower Traces) with Corresponding Direct Emission from a Tungsten Cathode for Several Laser Energies.

Photomultiplier
Current
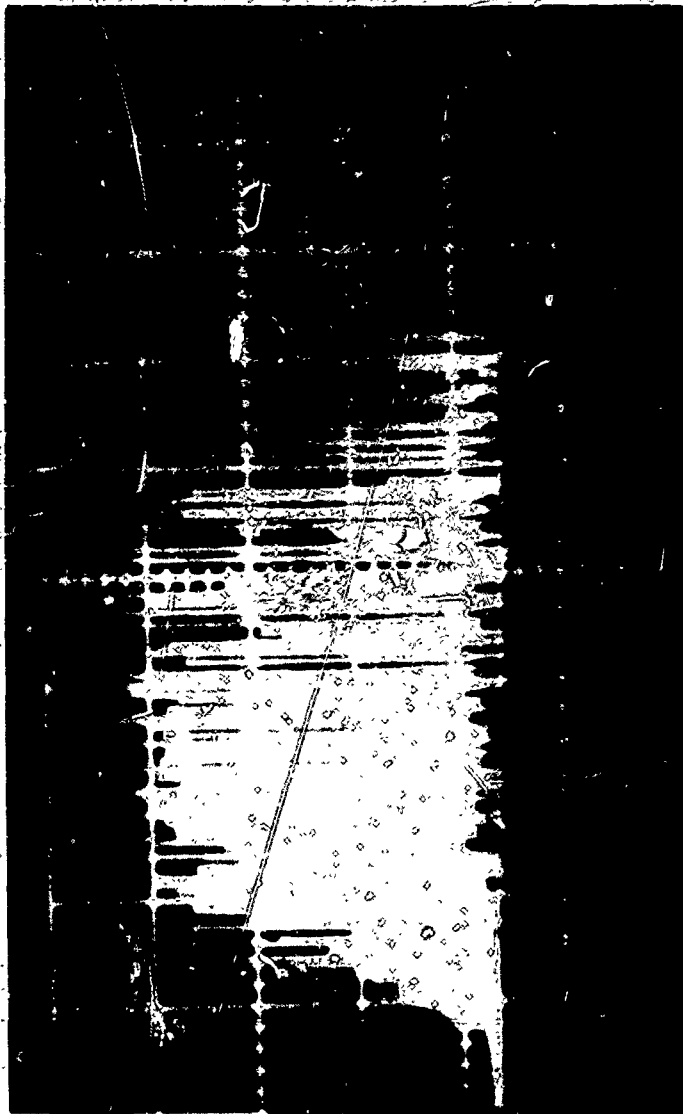
50 μs/cm ➝

Figure 2. Typical Laser Output Pulse.

end of a 0.12-in. diameter tungsten rod. Since the spot size was small compared with the rod diameter, the rod could be considered semi-infinite for thermal calculations. The emission in this case can be seen to follow the individual spikes of the laser pulse. Calculations using a simplified linear theory, that is, neglecting variations of thermal and electrical properties of the tungsten with temperature, show that this is to be expected, since the surface temperature can rise and fall at the approximately 2 Mc/s rate of the laser spikes. In fact, for tungsten, the surface temperature, and therefore the emission would follow the variations up to approximately 200 Mc/s. Even at such increased rates the temperature would follow the rising edge of each pulse but not the falling edge, since it is the cooling process that eventually limits the response. The maximum current densities observed for this direct emission case were of the order of 10^4 a/cm^2, but the spiking pattern made them of little practical use. The problem therefore is to produce a smooth, repeatable pulse.

One of the methods suggested for producing a pulse of this kind is by what has been termed "indirect emission." This involves heating a thin tungsten ribbon by laser irradiation on one side and drawing the emission from the opposite side, where the temperature fluctuations are considerably attenuated. Since a larger mass of tungsten has to be heated than with direct emission and because of the averaging effects of the diffusion of heat across the ribbon, a lower and smoother rate of increase of temperature at the emitting surface results. Also a considerably reduced rate of cooling is

-62-

obtained because of the much reduced conduction path of the thin ribbon compared with that of the relatively large tungsten rod.

This report describes the emission observed under the conditions of indirect emission from the laser cathode and the formation of a magnetically focused beam of moderately high current densities using this emission process.[*]

II. DESCRIPTION OF THE APPARATUS

The fundamental emission process was studied using a simple diode, and two beams were formed using very simple guns with pulsed magnetic field focusing. Each tube was used with the laser head, optical system, vacuum system, and pulsed magnet shown in Figure 3. The associated power supplies and pulsing circuitry are shown schematically in Figure 4.

A. VACUUM SYSTEM

The vacuum system was of stainless steel sections connected together by Varian flanges using copper gaskets. The central section was a stainless steel cross which had a Varian 8/sec VacIon pump on one arm, a vacuum valve on the opposite arm, a glass port for the laser beam to enter the vacuum system on the third arm, and a stainless steel tube with a pulsed magnet fixed on it on the fourth arm. The diode and beam testers were mounted on Varian vacuum flanges and fitted inside the tube on which the magnet was mounted. With this demountable system, each tube could easily be removed either for replacement of the filament or replacement by another tube. If the magnetic field was not required, the magnet section could be removed and the tube attached directly to the arm of the cross. Since each magnet was fixed permanently on its stainless tube, the magnet was changed by replacing this section.
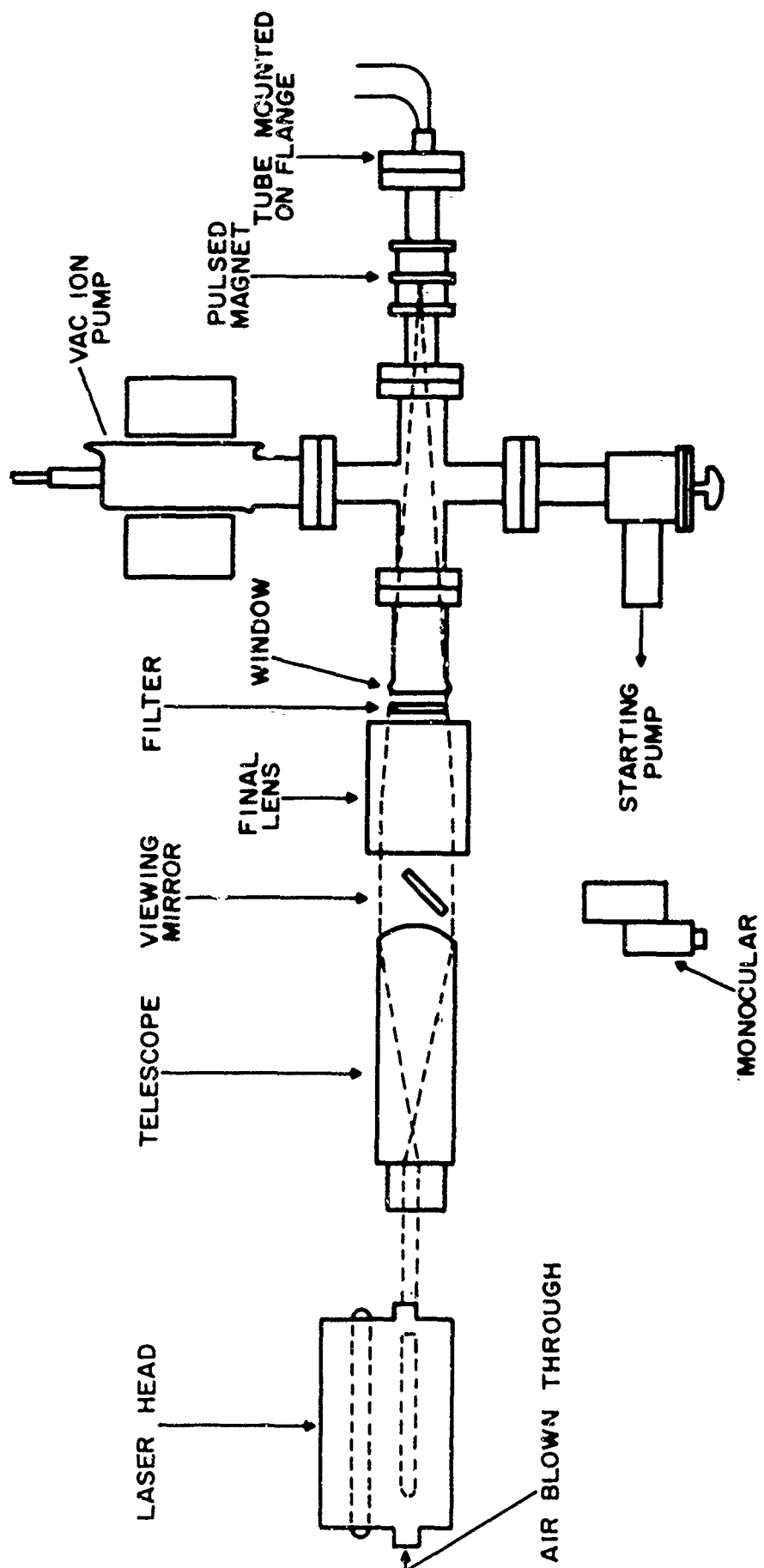
Figure 3. General Arrangement of Apparatus.

LASER HEAD

AIR BLOWN THROUGH

TELESCOPE

VIEWING MIRROR

FINAL LENS

FILTER

WINDOW

VAC ION PUMP

PULSED MAGNET

TUBE MOUNTED ON FLANGE

STARTING PUMP

MONOCULAR
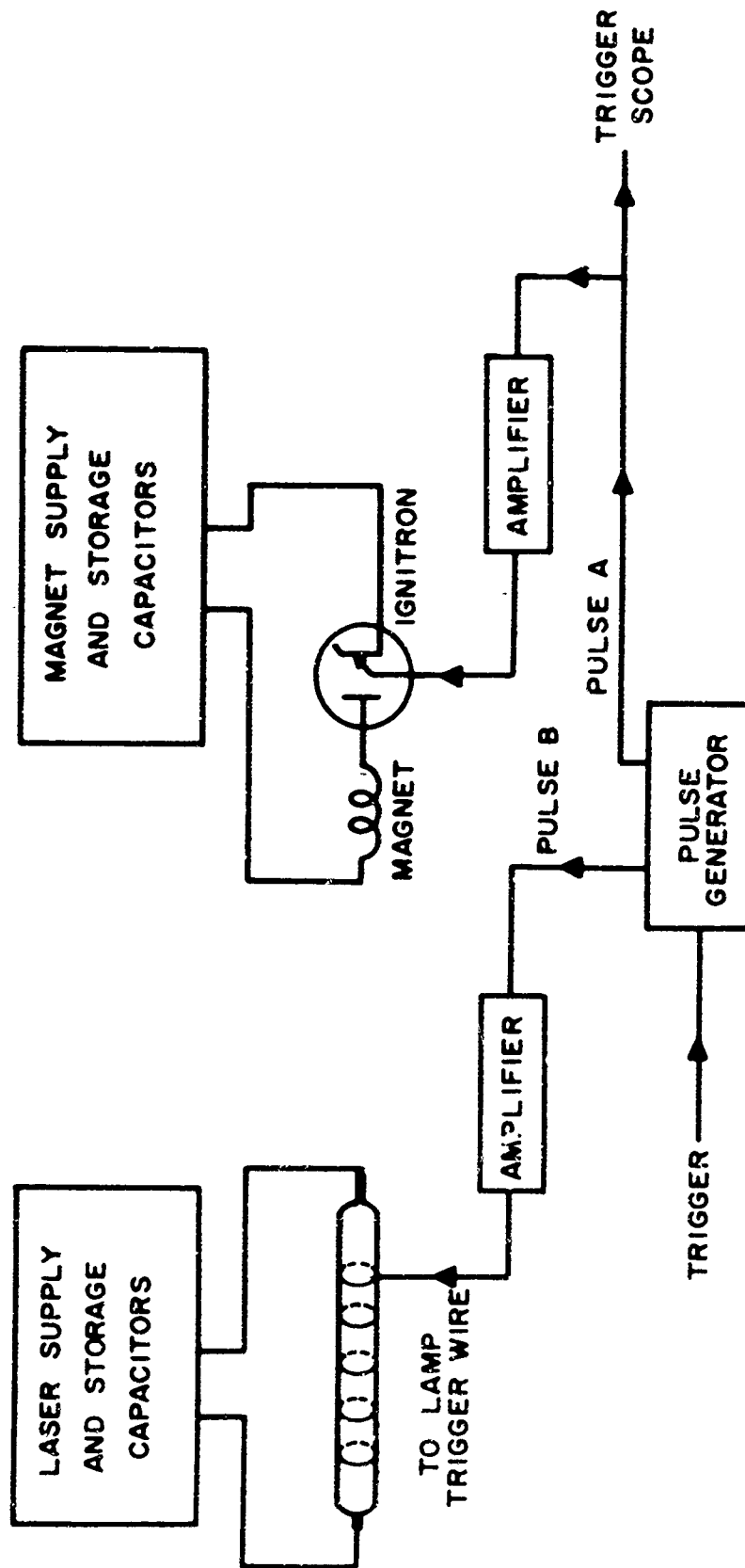
Figure 4. Schematic Diagram of Power Supplies and Pulsed Circuits.

The pressures achieved with the system were around 10^{-7} Torr. At this pressure the monolayer adsorption time was around 10 sec while the time between laser pulses was 100 sec. Several monolayers of gas could therefore condense on the filament between pulses. A pressure of 10^{-9} Torr, giving a monolayer adsorption time of 1,000 sec., would have been much better. In spite of this poor pressure, however, residual gas seemed to have little effect on the emission after the cathode had been aged by the first few laser pulses.

B. LASER

The laser head used for the experiments is shown in an exploded view in Figure 5. This laser was designed and constructed at Cornell University.[3] The pink ruby crystal, with a diameter of 0.25 in. and a length of 6 in., gives radiation at the characteristic wavelength of $6943A^\circ$, corresponding to a photon energy of 1.78 ev. The chromium doping is 0.05 per cent and the crystal has a 90° optical axis orientation; that is, the optical axis is perpendicular to the axis of the crystal cylinder. The transmitting end is flat and uncoated, whereas the opposite end has a two-facet chisel forming a total internally reflecting (TIR) prism. The crystal and a linear Xenon flash tube are contained in an elliptical housing with polished stainless steel reflectors coated with silicon monoxide. The crystal is at one focus of the ellipse and the lamp at the other. This is a relatively efficient arrangement. The laser gives 1 joule for every 300 joules into the lamp above threshold and is therefore
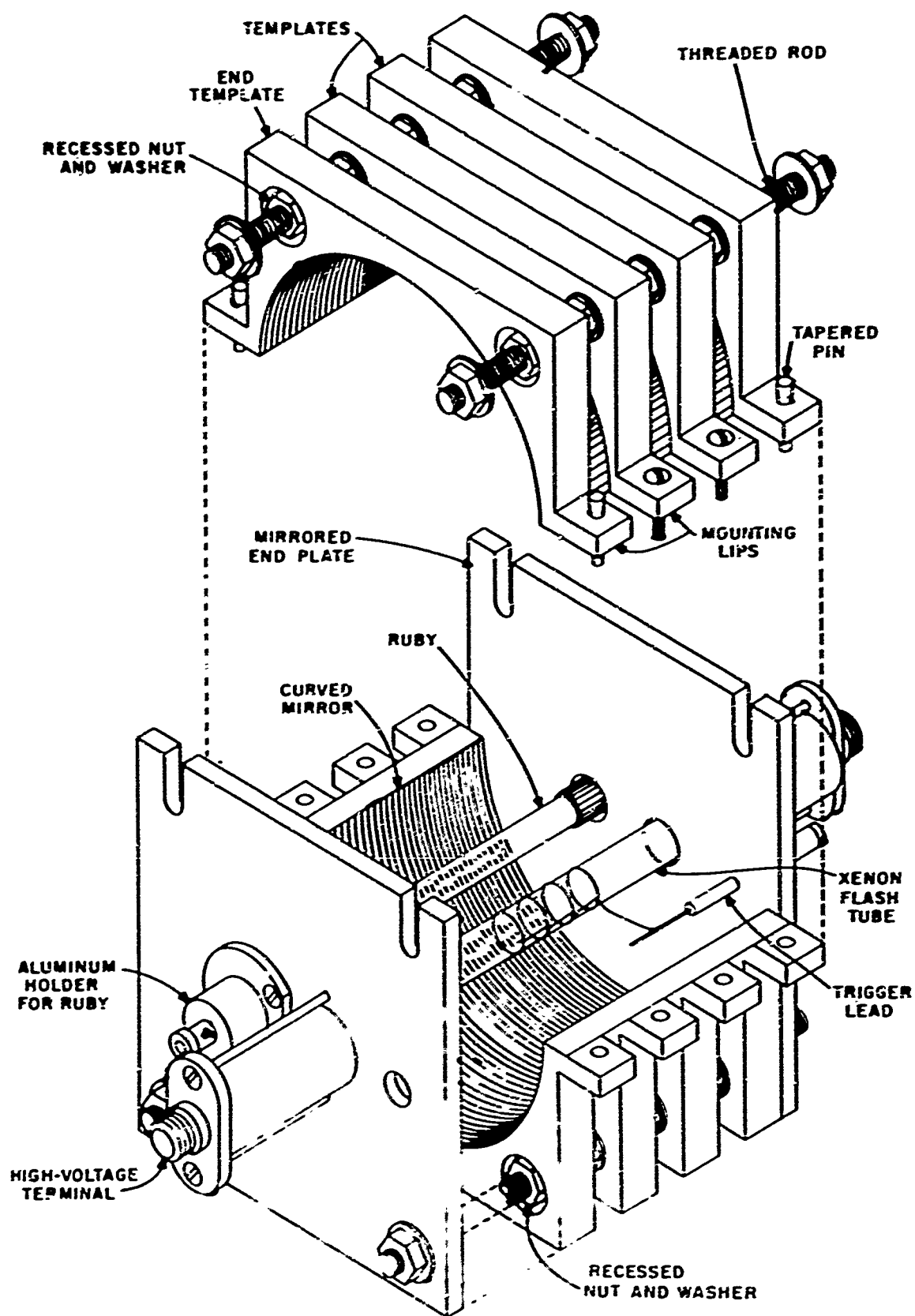
Figure 5.   Exploded View of Laser Head.

0.33 per cent efficient. Only 2.5 per cent of the electrical energy dissipated by the Xenon flash tube is converted to light, which is in a useful wavelength range for pumping the laser; this light is therefore used with an efficiency of 13 per cent once the crystal has been pumped above threshold. The completely uncoated crystal allows high energies to be obtained for many pulses without the deterioration in performance associated with coated crystals, the coating of which can be evaporated off by high laser energies.

The power supply for the laser is a conventional d-c supply, which charges a capacitor bank to a preset voltage. A pulse generator generates two pulses with the time between them variable from 20 μs to 600 μs. Either one of these pulses can be used to trigger the laser, the magnet, or the oscilloscope. This pulse generator was used to make the laser pulse coincide with the center of the magnet pulse. The laser lamp is fired by means of a 15 kv pulse delivered to the lamp trigger wire. This pulse is obtained by discharging a capacitor through the primary coil of a pulse transformer using a silicon-controlled rectifier as a switch, the trigger pulse being taken from the secondary coil of the transformer. The silicon-controlled rectifier is switched by a pulse from the pulse generator. The capacitor bank of the laser supply can be 120 μf, 240 μf, or 360 μf and has an ultimate storage capacity of 2,700 joules.

In order to understand the heating process and also to produce an irradiated spot of the required size, it was found necessary to investigate several of the laser characteristics. Measurements of the

total energy per pulse were made using a calorimetric technique developed by Li and Sims[4]. The basic element was a carbon cone of 0.51 gm mass placed in an insulating enclosure. The cone was raised 2.8°C in temperature by a pulse of one joule. Embedded in a groove around the edge of the cone were three Fenwal thermistors operated at about 2000 Ω each. When this calorimeter was used with the circuit shown in Figure 6a, an output of 31 mv per joule was obtained from the bridge. The main purpose of the d-c amplifier was to provide an impedance transformation between the bridge circuit and pen recorder, since the out-of-balance voltage of the bridge was being measured and this had to be done with a circuit of high impedance compared with the various bridge resistances. With this calorimeter it was found possible to measure energies up to the maximum energy of the laser used, which was a few joules, and down to a few millijoules, corresponding to a temperature rise of the cone of about 0.01°C and an output voltage from the bridge of about 0.1 mv. A typical curve showing the response of the calorimeter to a series of pulses of 0.45 joules at 100-sec intervals is shown in Figure 6b.

The peak deflection, which was obtained 9 sec after the laser pulse, had to be corrected for cooling during the heating time. A logarithmic plot of the deflection as a function of time showed a nearly exponential cooling after the peak deflection had been reached. If the same cooling rate was assumed up to the time of reaching peak deflection, then a correction to this deflection of 26 per cent was required. This last assumption is somewhat suspect, since the cooling
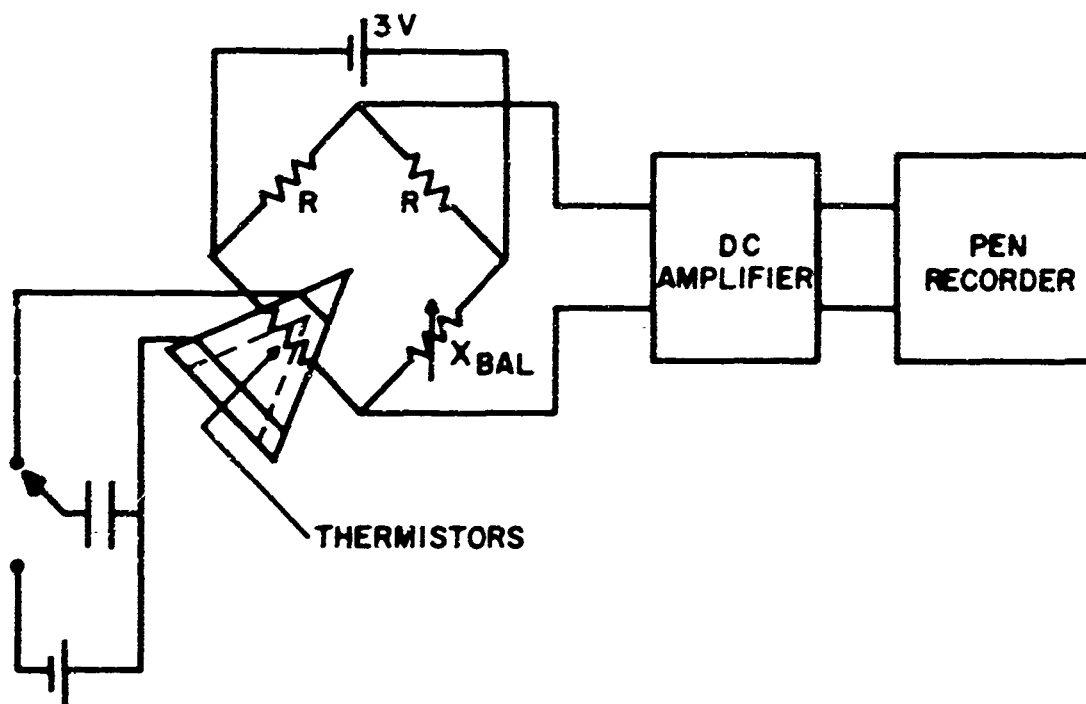
(a)
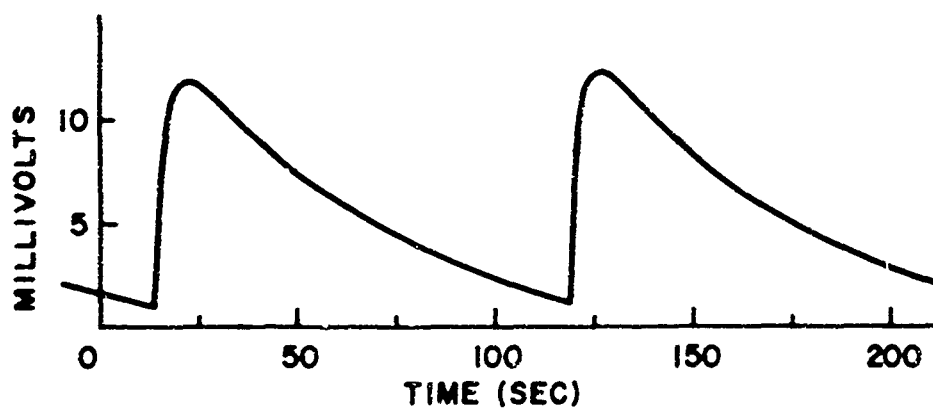
(b)

Figure 6. (a) Circuit for Laser Energy Measurements Using
Carbon Cone Calorimeter. (b) Response of Circuit
in (a) to Two Laser Pulses of 0.45 Joules.

rate may be quite different while the heat is diffusing through the carbon cone. This method cannot be relied on therefore, for absolute values of better than 10 per cent. A reduced rate of cooling of the cone would increase the accuracy of absolute measurements. Relative measurements can be made with much greater accuracy. A calibrating pulse was obtained by discharging a capacitor through a fine wire embedded in the circumference of the cone.

Other workers have used this method of energy measurement. A similar method described by Daman and Flynn[5] uses a liquid of appropriately chosen absorption coefficient as the absorbing medium. This method overcomes the problem of overheating and evaporating the surface of the carbon cone at high energies. For the measurements described here, care was taken to ensure that the laser beam irradiated at least half the surface of the cone so that this problem was avoided.

It is also possible to measure the energy from the laser using a calibrated phototube in conjunction with filters of known transmission coefficient.[6] In this case the filters are necessary to prevent damaging the tube and to ensure operation over the linear part of their range.

With the calorimeter described placed directly in the laser beam, Figure 7 was obtained. This shows the variation of output energy with electrical energy into the flash lamp. The threshold was close to 320 joules with the output energy varying linearly with input energy and an efficiency above threshold of 0.33 per cent. The threshold and efficiency of the laser, and therefore the output power of the laser, are functions of the temperature of the crystal
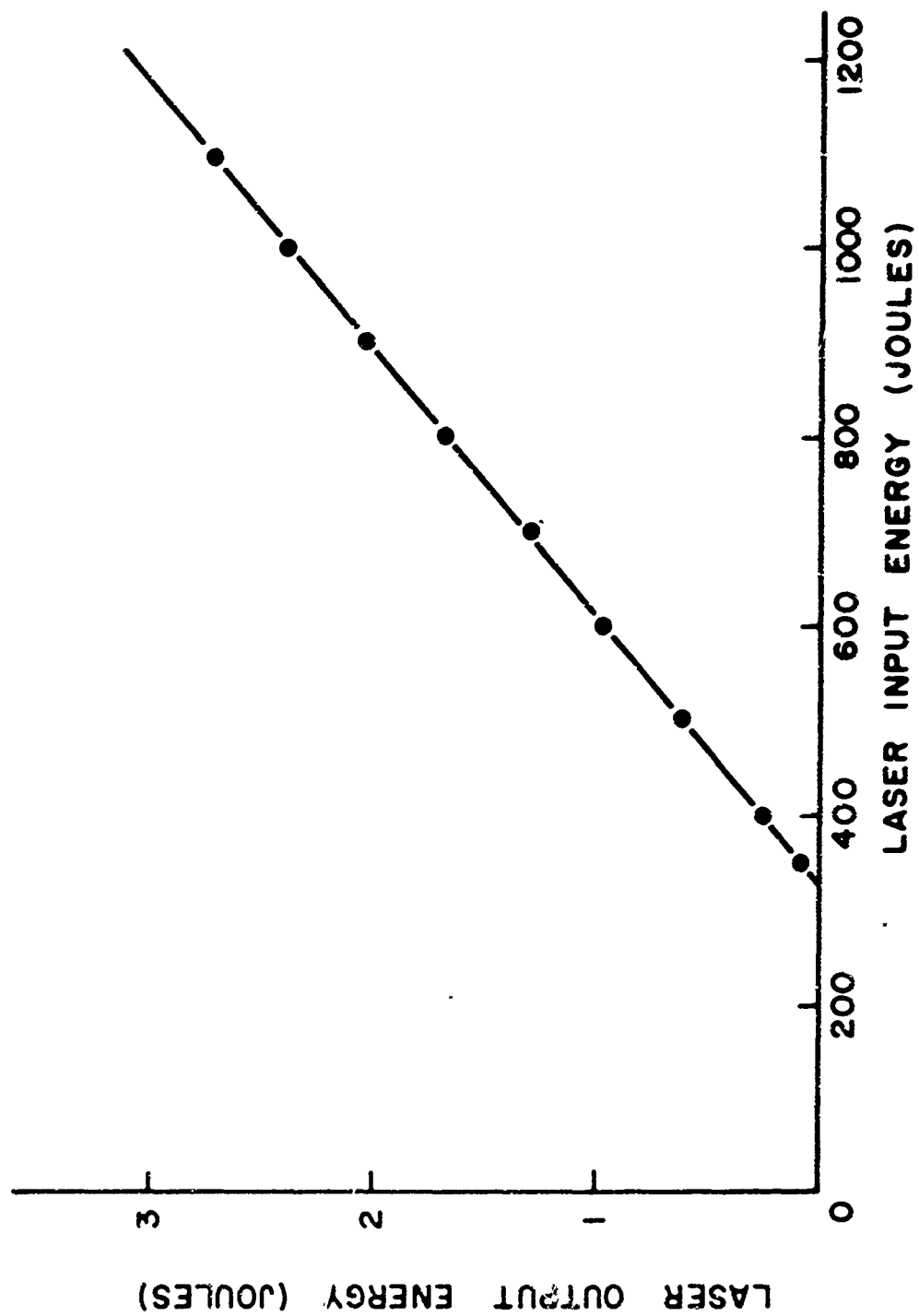
Figure 7. Laser Output Energy as Function of Energy into Flash Tube.

and the rate at which pumping energy is supplied to the crystal.[6]
It is therefore important to keep these quantities constant in order
to obtain a constant output from pulse to pulse. The rate of supply
of pumping energy depends on the inductance, capacitance, and resistance
of the discharge circuit and the constancy of the lamp discharge.
Manufacturers specification of the lamp discharge indicate that it is
constant over some thousands of pulses; therefore this did not present
any problem for the experiments described here. The temperature of
the laser crystal was therefore the most important factor.

Figure 7 shows that several joules of energy were available from
the laser. Calculations show that only 1.7 millijoules of energy are
required to heat a 0.005-in. diameter spot on the ribbon to the
melting point of tungsten and that 15.3 millijoules of energy are
required to heat a spot of diameter equal to the width of the ribbon.
A few tens of millijoules are therefore the maximum required, and the
laser is capable of giving many times more than this.

Figure 8 shows the variation of the laser output with pulse
number when it was pulsed at several different rates. Curves are
shown for three pulsing rates with two different cooling conditions.
The cooling conditions were: (a) the crystal cooled simply by
conduction and convection within the laser head; (b) the crystal
cooled by a stream of air at room temperature blown through the
laser head. Since the lamp and air within the enclosure was heated
by each discharge, cooling under conditions (a) was very slow and
there was a rapid fall off of energy with pulse number at the pulsing
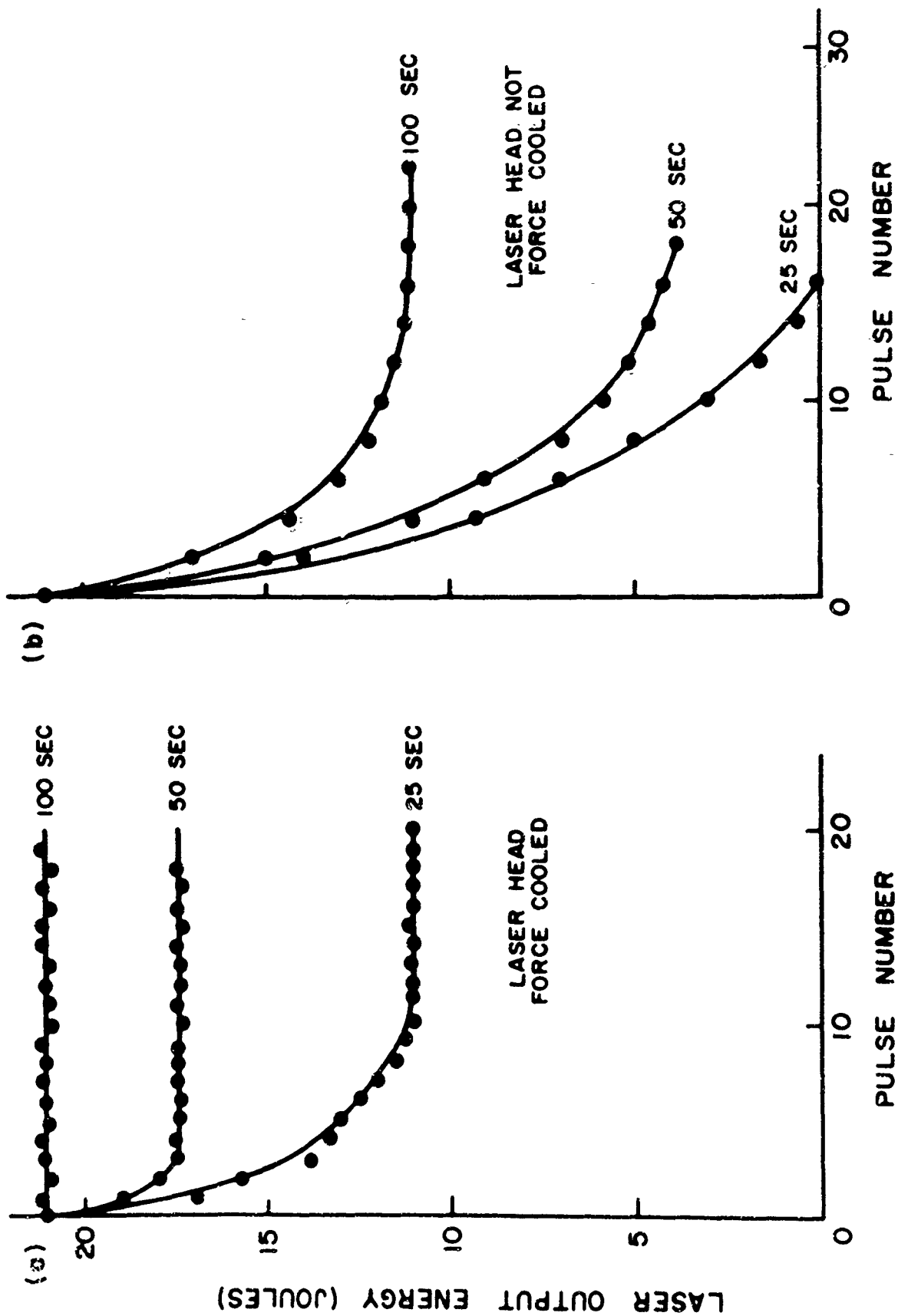
Figure 8. Variation of Laser Output with Pulse Number for Several Pulsing Rates. Times Shown are Times Between Consecutive Pulses.

rates shown. Cooling under conditions (b) were much more rapid;
furthermore equilibrium at a constant pulsing rate was quickly
achieved. With 100 seconds between pulses there was negligible
reduction of energy output with pulse number, so that when a time
between pulses of 100 sec or greater was used, a constant output was
achieved. These therefore were the pulsing conditions used for all
the experiments.

In order to form a spot of the required diameter on a target,
it is necessary to know, at least in a rough way, the variation of the
radiation intensity over the face of the crystal and also the
angular divergence of the emitted beam. These were therefore measured
for the laser being used since they depend on several factors and
cannot be calculated with any certainty.

The output energy is certainly not radiated uniformly from the
face of this or any other laser crystal, principally because the
cylindrical shape of the crystal concentrates the pumping light into
the center. This results in an intensity that is maximum at the
center of laser crystals and that decreases smoothly toward the
circumference. Figure 9 shows the variation of energy passed by a
stop placed near the crystal face with the area of the hole in the
stop. This shows that the emission is a maximum at the center and
falls off towards the perimeter as expected. These measurements
give the sum for the entire pulse train of the energies of the
individual spikes from a given fraction of the crystal face. Hughes
and Young[7] and others have taken photographs of the crystal face
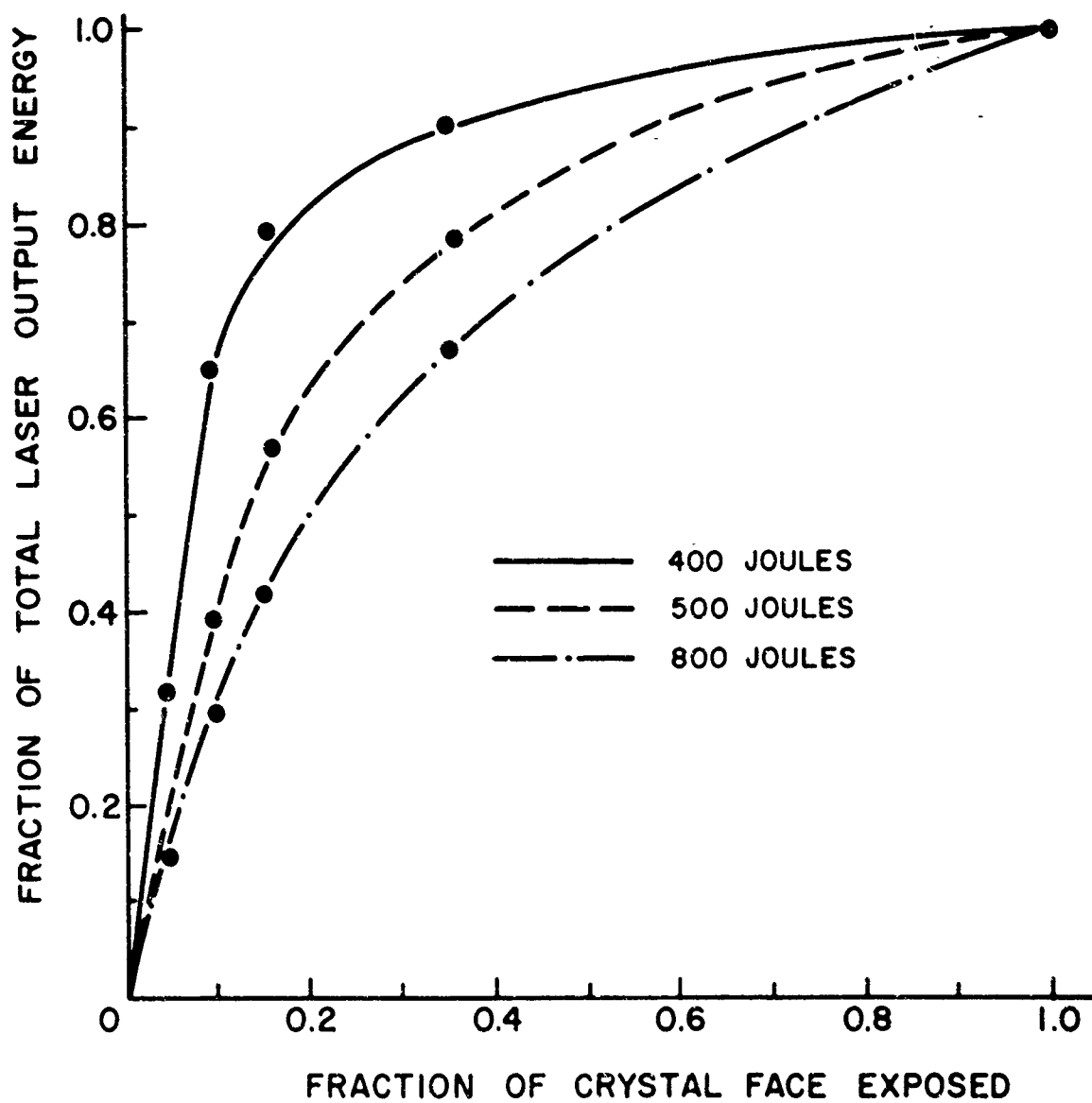
Figure 9. Spatial Variation of Laser Output Over Crystal Force.

using a rotating mirror camera so that they could resolve the individual
spikes. Their results showed that each spike corresponded to a mode
of the crystal. Also different small regions of the crystal face emit
independently of each other with the spatial variation of the emission
varying from spike to spike, but with each emitting region always
emitting its own particular mode sequence. More recent work[6] has
shown, however, that well above threshold the separate emitting spots
couple together, and the emission is more uniform over the face of
the crystal. Both these results were found with the laser used in
this study. When an image of the crystal face was formed on the side
of a razor blade and the laser fired close to threshold, a mark was
made with several small holes dotted over it, presumably corresponding
to the different emitting spots of the laser face. When this was
repeated with the laser fired well above threshold but with the beam
attenuated with a stop so that approximately the same amount of energy
fell on the blade, a much more uniform mark was made confirming in a
rough manner the observations of other workers. For this reason, in
order to obtain a uniformly irradiated area, it is necessary to
operate the laser well above threshold and to attenuate the beam by
stops or filters or both. Another reason for operating well above
threshold is to obtain a constant energy output since small changes
in the threshold level have less proportional effect when working well
above threshold.

With a TIR crystal, the edge of the chisel point and the axis
of the cylinder define a plane of symmetry, and one can think of the

two halves of the emitting face, one on either side of this plane, as corresponding to the two ends of a flat-ended crystal. Because of the way the rays are reflected around the crystal about this plane of symmetry, the two halves of the face should radiate mirror-image image patterns. This could in fact be seen in the pattern of spots described in the preceding paragraph and in marks burned on a polaroid film when placed in the laser beam with the laser fired close to threshold.

The angular divergence of the beam was measured photographically. A ground-glass plate was placed 22ft from the laser. The image formed on this screen when irradiated by the laser beam was photographed using a Polaroid Land oscilloscope camera complete with hood, the ground-glass screen being fixed over the end of the hood in the position which the oscilloscope screen would normally occupy. This proved very effective and simple, since the hood eliminated stray light and the exposure could be adjusted using the camera stops. The alternative to this, which would be to expose the film directly to the laser beam, would involve adjusting the intensity of the beam with filters and achieving a much darker room than was necessary with the present technique. Some of the photographs obtained are shown in Figure 10. From these photographs it can be seen that the beam has a bright central region surrounded by a lower intensity region, and that an interference pattern redistributes the light into a series of parallel bars. The bright central region is not circular but spread symmetrically about a line through the center perpendicular to the long direction of the bright area. The direction
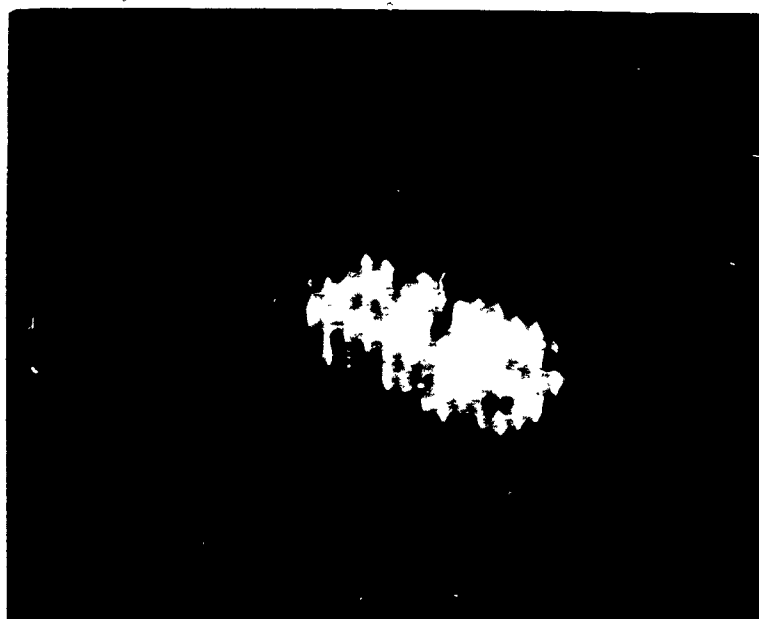
(a)
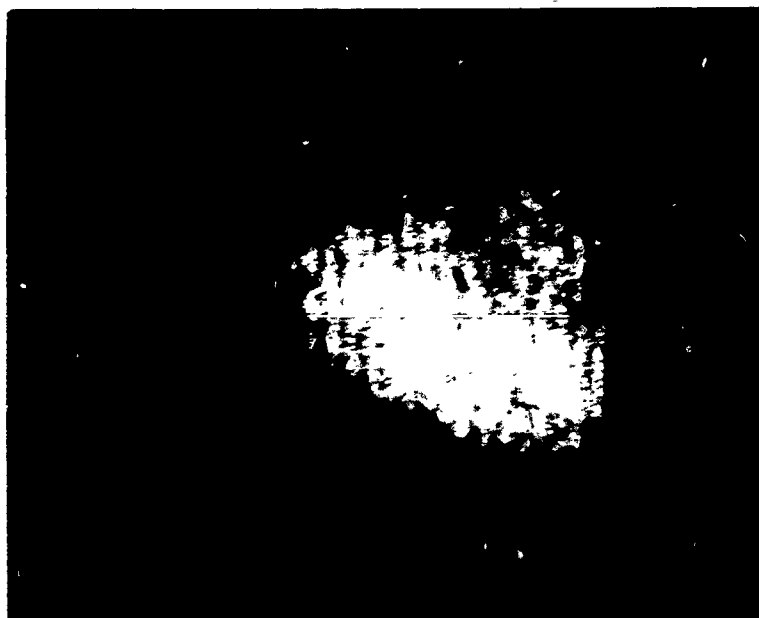
(b)

Figure 10. Far Field Pattern of Laser Beam. (a) Input
Energy of 350 Joules (10 Percent Above
Threshold); (b) Input Energy of 550 Joules
(55 Percent Above Threshold), 1/13
Exposure of (a).

of this line corresponds to the direction of the chisel edge of the IR crystal. The bright region corresponds to a beam of divergence 0.27° by 0.16°, and the outer region corresponds to a beam that falls to negligible intensity at a divergence of 0.7°. These figures are somewhat rough, especially in view of the nonlinearity of response of the Polaroid type 410 film which was used, but they proved adequate.

The interference pattern, although of little consequence to these experiments, was very interesting. A flat-ended crystal gives a pattern which is a series of concentric rings[6] in contrast to the present parallel bars. It is tempting to interpret this pattern of parallel bars as due to interference between the two beams from the two halves of the crystal face as described above. If this were the correct explanation, however, the bars should be parallel to the chisel edge of the crystal, whereas, as can be seen from the photographs, the bars make an angle of 12° with the direction of the crystal edge, which is the short direction of the bright region. This pattern, therefore, is not at the moment satisfactorily explained.

In summary, the laser is capable of delivering up to 10 joules with a threshold of 320 joules and an efficiency above this of 0.33 per cent. The radiation from the crystal is most intense at the center and falls off toward the perimeter of the crystal. The beam has a bright central region of divergence 0.27° by 0.16° with an outer, less intense region of divergence 0.7°.

C. OPTICAL SYSTEM

Once the properties of the laser were determined, it was possible to design an optical system to give the required irradiated spot diameters and radiation intensity at the target.

Because of their small divergence, laser beams normally give the most intense spot at the focal plane of a focusing lens. Since the distance between the target and window was about 12 in. when the magnet section was in place, a lens of at least this focal length was required. A 16-in., three-element astigmatic lens was readily available and was therefore used. With 0.27° for the divergence of the central part of the beam, the beam was brought to a focus at the focal plane of the lens forming an image of 0.075-in. diameter, which was 15 times the required diameter. The size of the image could readily be reduced by reducing the divergence of the beam. This was done by passing the beam through a telescope of 15x magnification, the beam passing from eyepiece to objective as shown in Figure 11. When the divergence of the beam was reduced by a factor of 15, the beam diameter was necessarily increased by the same factor. This increased the beam diameter to a value somewhat greater than the diameter of the objective, so that not all of the beam was passed by the telescope. The best way to consider how the telescope serves as an effective stop is to note that the only rays that can pass through the objective of the telescope are those rays that pass through the image of the objective lens formed in the eyepiece. This image is indicated by I_o in Figure 11. If the diameter of this image is d_i, then

Figure 11. Diagram of Optical System.

$$d_i = \frac{f_e}{f_e + f_o} d_o \quad .$$

Putting in the values used for f_e, f_o, and d_o gives a value for d_i of
0.1 in. Therefore only the part of the beam that passes through this
0.1 in. diameter image is passed by the telescope.

The size of the image I_1 formed at the focal plane of L_3 is given
by

$$d_1 = \alpha \frac{f_e}{f_o} f_3$$

where α is the angle of divergence of the bright part of the beam.
An image of the crystal face is also formed at the plane I_2, and the
size of this image is given by

$$d_2 = \frac{D}{u} \frac{f_e}{f_o} f_3 \quad ,$$

where u is the distance from the laser to the telescope eyepiece,
and D is the diameter of the emitting area of the crystal. The
effective stop of the telescope does not reduce the intensity of
this image uniformly over the image, however, since the light from
the crystal face is not emitted uniformly in all directions.

The exact way in which the intensity over the image is changed
depends on the detailed angular distribution of light from each point
of the crystal face, and this was not known. With u equal to 15 in.,

-84-

however, the diameter of the beam at I_o was twice its diameter at the crystal face. Since only that light that passes through I_o, (whose diameter is 0.1 in.) passes through the telescope, the light passed is mainly from the central 0.050 in. of the crystal face. If this value is used for D; then the diameter of the image is 0.0035 in. This value of D is a minimum value and the calculation therefore shows that the two images are of about the same size.

The distance between the two images I_1 and I_2 is given by

$$x = \left(\frac{f_3}{f_o}\right) \frac{f_3^2}{u} \quad .$$

For the system used

$$f_e/f_o = 1/15 \qquad f_3 = 16 \text{ in.} \qquad u = 15 \text{ in.}$$

therefore

$$x \approx 0.075 \text{ in.}$$

These calculations were checked by placing a piece of exposed polaroid film in the position normally occupied by the target. When the laser was fired, silver was evaporated from the film where it was struck by the laser beam, leaving a white mark. Lens L_3 was moved in steps of 0.020 in. such that the film was initially about 0.1 in.

from I_2 and finally about 0.1 in. from I_1. A spot was produced between I_1 and I_2 and also a short distance beyond these positions, which was of constant size and which increased in diameter with increase in distance away from this central region. The most important result of this was to show that the focusing was not very critical. In practice the end of the laser was illuminated and its image focused on either the cathode or, what was often better since it gave a clearer image, on the anode at the side of the cathode. The focusing was done by moving L_3. The size of the spot evaporated from the film depended on the radiation intensity and varied between 0.005 in. and 0.010 in. When a piece of tungsten ribbon was placed in the same position, however, the irradiated area had a central region of diameter 0.005 in., which had been molten, surrounded by a bright region from which the surface impurities had been evaporated. The diameter of this bright area was 0.010 in. to 0.012 in. so that the entire 0.015 in. width of the ribbon was heated. When the laser was fired near threshold with the tungsten ribbon at I_2, the spots previously described as corresponding to the small emitting regions of the laser face could be clearly seen. When the ribbon was moved to I_1, these disappeared. The size of each spot was of about 0.001 in. diameter corresponding to almost 0.010 in. diameter at the crystal face.

In order to be able to adjust the position of the beam, the telescope was mounted on gimbals, with the pivots in the plane of I_0.

A micrometers were used to move the front of the telescope vertically, and another to move it horizontally. For the lenses used, 0.001 in. movement of each of these micrometers gave 0.003 in. movement of the beam at the target. The position of the beam could therefore be adjusted to within 0.001 in. fairly easily. The gimbal mountings were in the plane of I_o, so that when the front of the telescope was moved, there was no translational movement of I_o and the same part of the beam was passed by the telescope keeping the irradiated spot of constant size and radiation intensity. The slight angular movement of I_o had negligible effect on the light passed by the telescope. The principal alignment of the system consisted therefore in ensuring that the gimbal mountings were in the plane of I_o and that the center of the beam passed through I_o. Once this adjustment was made, L_3 was aligned so that the center of the beam passed through its center. The vacuum system was then aligned so that the beam passed through the center of the window to the target. Finally an image of the laser end was focused centrally on the target. The target was viewed using the monocular shown in Figure 3 in conjunction with a small viewing mirror. Since the target was close to the focal plane of L_3 and therefore when viewed in the mirror was formed at infinity, a telescope in the form of a monocular was required to see it. The viewing mirror was removed from the beam when the target was being irradiated.

Since in order to form a small spot it was necessary to reduce the beam divergence by a factor of 15, the beam diameter had to be

increased by a factor of 15. More generally, for a given beam, the size of the irradiated spot depends only on α_2, the angle of convergence of the beam at the target. The spot size is inversely proportional to α_2 and the smaller the spot size required the greater must be the angle of convergence at the cathode.

For the present experiments the value of α_2 required created no problems. For a beam produced by direct emission, it might be necessary, however, to place a structure around the beam. In this case the laser beam would either have to pass through the structure to the cathode or strike the cathode at an angle. The second alternative might be possible if the anode was well spaced from the cathode so that the change in anode-to-cathode spacing from one side of the beam to the other was not too important. It would not be possible to eliminate the effects of the tilt completely, however, and this might not be a practical approach. The alternative of passing the laser beam through the structure requires a beam of low angle of converge and therefore, paradoxically, of high beam divergence, so that a large spot would be produced. The way to overcome this would be to decrease the divergence of the beam produced by the laser.

This has been done for a ruby laser by two methods.[6] The first method used a long cavity to reduce the beam divergence, the mirrors being up to one meter apart. The second method used a stop in the cavity. Both of these methods have disadvantages. The first method involves using mirrors separated from the crystal, which must be accurately adjusted. The second method results in a considerable

reduction of the laser output energy, and the stop is damaged if the laser is fired at a high level for more than a few shots.

These difficulties, which would be encountered in the production of a beam by direct emission, do not arise in the production of a beam by indirect emission. This shows a considerable advantage for the indirect emission beam although it may be worth while to overcome the problems associated with direct emission by producing a direct-emission beam using the single pulse from a Q-spoiled laser.

D. PULSED MAGNET

The standard method of producing strong pulsed magnetic fields is to discharge a capacitor bank C, charged to an initial voltage V_o, through a magnet coil of inductance L, and resistance R. The damped oscillatory discharge is expressed as

$$I = \frac{V_o}{Z_o} e^{\frac{t}{2\Gamma}} \sin (\pi t/T')$$

where

$$\Gamma = \frac{L}{R} \qquad T = \pi(LC)^{1/2} \qquad T' = T \left[1 - \left(\frac{T}{\pi\Gamma} \right)^2 \right]^{1/2}$$

$$Z_o = \left(\frac{L}{C} \right)^{1/2} \left[1 - \left(\frac{T}{\pi\Gamma} \right)^2 \right]^{1/2} .$$

The peak current is reached at $t = \frac{1}{2} T'$ and is given by

$$I_o = \frac{V_o}{Z_{eff}}$$

where

$$Z_{eff} = Z_o e^{\left(\frac{T}{4\Gamma}\right)'} = Z_o e^{\left(\frac{\pi R}{4Z_o}\right)} \quad .$$

If R is small, the damping is small and the discharge is closely sinusoidal, so that

$$I_c \simeq V \left(\frac{C}{L}\right)^{1/2} \tag{1}$$

and

$$T \simeq \pi (LC)^{1/2} \tag{2}$$

where T is the time for one-half period of the oscillation.

The energy dissipated in joule heating during the first half-cycle is

$$\frac{1}{2} I_o^2 R T$$

when $\Gamma \gg T$; i.e.,

$$R \ll \left(\frac{L}{\pi C}\right)^{1/2} \quad .$$

The design of the magnet coil started from the fact that a half-period T of about 1 ms was required and that three 120 µf, 3 kv capacitors were available. Putting these figures into Equations (1) and (2) gives a value of 280 µh required for the inductance of the coil, and a value of about 3,400 a for the peak current. Two magnets were made using this design data. The first was a simple solenoid wound on a 7/8-in. former which was 2 in. long. Calculations showed that for this size magnet five rows of 33 turns each of no. 14 wire would give the required inductance. With the peak current just given and an infinite solenoid, the peak field on the axis would be about 78 kgauss, which is more than required. The second magnet consisted of two coils wound on a 7/8 in. former each 1/2 in. wide and spaced 1/4 in. apart. The required inductance was given by 50 turns of no. 14 wire wound on each of these coils. Since for this magnet the number of turns per inch was greater than for the simple solenoid, the magnetic field for a given current was somewhat higher. The coil pair arrangement also gave a greater length of uniform field than the simple solenoid and was therefore used for all of the beam-focusing experiments. This magnet and the field configuration are shown in Figure 12. The field varies by only 1 per cent over a 3/4 in. length. This was achieved by careful adjustment of the distance between the two coils and by adjusting the number of turns on the coils to give exactly the same field for the same current when operated separately. This was necessary since there are only 50 turns on each coil so that a one-half turn difference gives a one per cent difference in field.
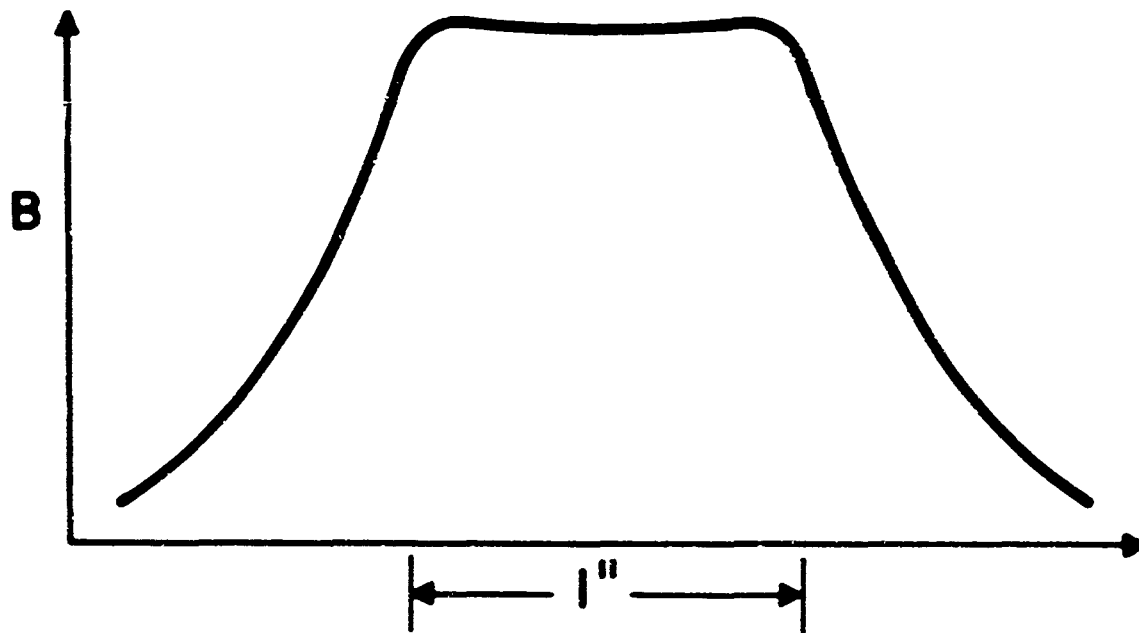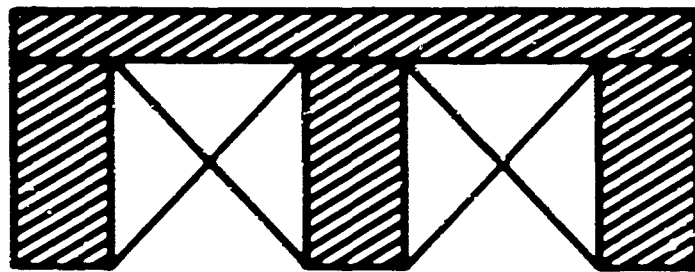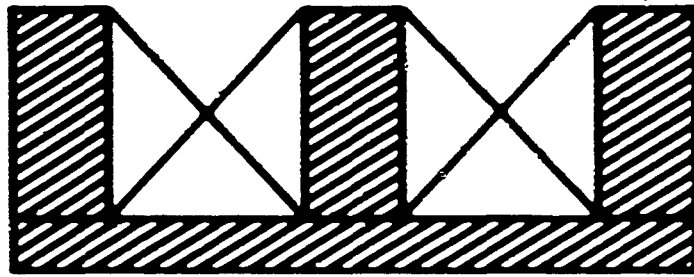
Figure 12. Diagram of Two-Coil Pulsed Magnet with Field Configuration.

As indicated the peak current is several thousand amperes. In order to switch this current a R.C.A. 5514 Ignitron was used. Once this had been fired, it conducted in both directions and therefore allowed the inductance-capacitance discharge to ring until all the energy originally stored in the capacitors had been dissipated in the circuit resistance, and therefore principally in the magnet. Since it was required that the magnet heating be kept to a minimum, this ringing was not desirable. To avoid this a choke was included in the discharge circuit, which saturated at currents of a few tens of amperes, and which had an inductance about two orders of magnitude greater than that of the magnet when not saturated and an order of magnitude less than that of the magnet when saturated. With the use of the choke, the time constant of the discharge was much increased at low currents and altered very little for higher currents. This delayed the pulse while the current was low, keeping the current low at the end of the first half-cycle for a sufficient length of time (about 100 μs) to allow the Ignitron to deionize. This quenched the ringing at the end of the first half-cycle without appreciably altering either the period or magnitude of the discharge current. At the end of this first half-cycle, the capacitors were charged in the reverse polarity. In order to return them to their original polarity, a second discharge circuit was used with an identical Ignitron and choke.

The calculated value of R for the magnet is 0.137Ω giving a value for Γ of 2.08 ms. The amplitude of the oscillation should

therefore fall to $1/e$ in 4.2 ms. During the first half-cycle, therefore, the peak current with losses is only 13 per cent less than the peak current without losses. In fact there were also losses resulting from the finite Q of the capacitors, which increased the circuit resistance to a value of 0.213Ω calculated from the measured damping constant. This corresponds to a 20 per cent decrease of the peak current resulting from damping.

It is worth noting that $\Gamma = L/R$ is a constant for a given size and shape of the copper conductor being independent of the number of turns N, since

$$L \propto N^2 \quad \text{and} \quad R \propto N^2 \quad .$$

Now the Q of the circuit is given by

$$\frac{\text{energy stored}}{\text{energy dissipated/cycle}} = \frac{\frac{1}{2} L I^2}{R I^2 \ T} = \frac{L}{R} \frac{1}{2T} = \frac{\Gamma}{2T}$$

and this is therefore also independent of N for a given T. The Q of an air-cored pulse magnet cannot therefore be altered by altering the number of turns, but only by improving the packing factor or reducing the resistivity. If T is shortened such that skin effects become appreciable, the Q is further reduced. For the value of T and thickness of wire used, skin effects were not important, and the Q was such that about 50 per cent of the energy stored in the magnet

was dissipated in a single half-period. This gives a calculated temperature rise of 3°C per pulse when pulsed at maximum capacitor voltage. Since the laser was pulsed only once every 100 sec, this temperature rise presented no problems.

Figure 13a shows the magnetic field produced by the simple solenoid for several capacitor voltages. From this it can be seen that the delay caused by the saturable reactor varies with voltage and is least for the highest voltage. This is due to less time being required to reach saturation current in the delaying choke as the voltage is increased. The field measurements were made using a coil of a known number of turns wound on the end of a lucite rod and integrating the voltage output from this with a circuit of time constant T*, with T* being very much less than the length of the magnet pulse. Figure 13b shows a field pulse for the two-coil magnet. The change of slope at the two ends of the pulse can be clearly seen. The length of pulse for the simple solenoid was 1.0 ms corresponding to an inductance of 280 μh, and for the two-coil magnet the pulse length was 0.9 ms corresponding to an inductance of 265 μh. The measured peak current for $V_0 = 3$ kv for the two-coil magnet was 2,400 amperes, which gave a peak field of 66,000 gauss. With no resistance in the circuit, the peak current should be 3,500 a; with only the magnet resistance, it should be 3,200 a. The low value of 2,400 a was due to the low Q of the capacitors used. Using high-Q capacitors with the same ratings, this magnet should give 85,000 gauss. As pointed out in the section on beam focusing,

(a) 20 k gauss/div

(b) 20 kgauss/div

200 μs/div
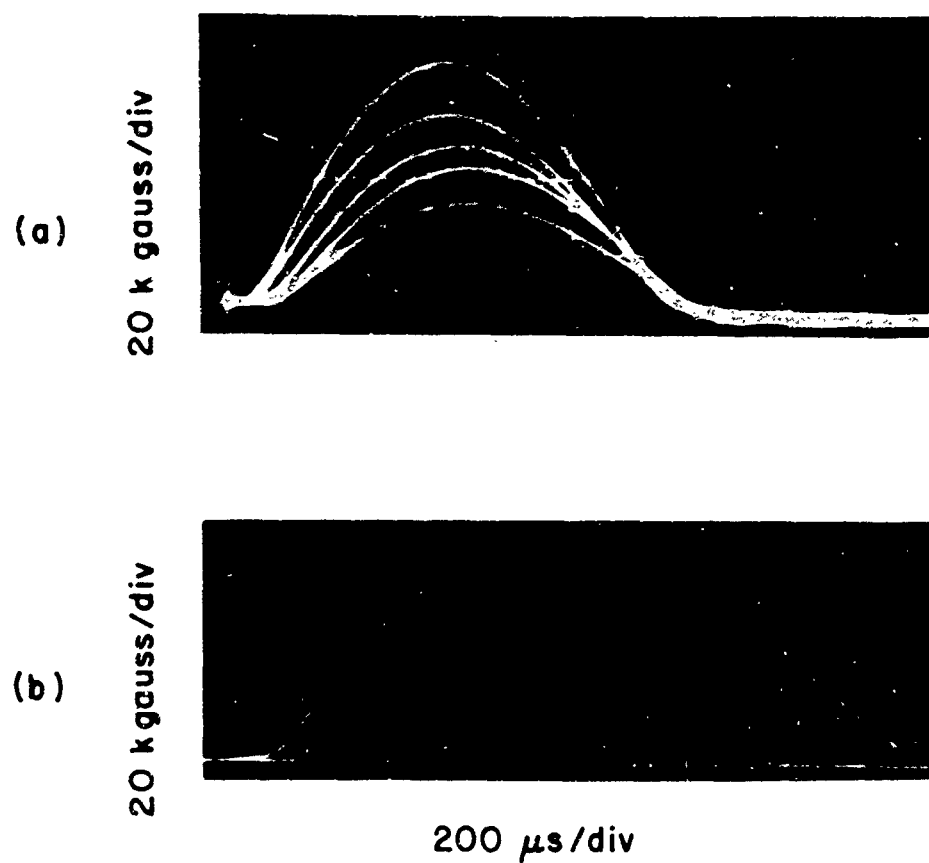
Figure 13. Magnetic-Field Pulses: (a) Of Simple
Solenoid at Several Discharge Capacitor
Voltages; (b) Of Two-Coil Magnet.

these values of magnetic field are well above those required to focus the beams produced by indirect emission.

Since the magnetic field was produced by this pulsed technique, some care had to be taken in the construction of the device that was to fit inside the magnet. In order not to produce large eddy currents and thus reduce the magnetic field, any tubing inside the magnet had to be less than the skin depth in thickness. At the frequency of 500 cps used, the skin depth in copper is 0.3 cm and the skin depth in stainless steel is 2.4 cm. Stainless steel tubing could therefore be used for the tube envelope and copper could not. To check this, a 3/4 in. rod of stainless steel was fitted inside the magnet. This rod had a hole from one end to the center into which the field probe fitted. With this in the magnet, the field was found to be reduced by a negligible amount, as can be seen from Figure 14, which shows the field pulse both with and without the stainless steel rod in the magnet. With the steel rod in place, the field was delayed by nearly 30 µs, this delay being the time required for the magnetic field to diffuse through the metal. This experiment showed clearly that stainless steel could be used for the tube envelope and other parts, and that its use would not lead to any reduction of the magnetic field. The movement of delicate parts, such as the cathode ribbon and its supports, as a result of interaction between the magnetic field and eddy currents or other currents flowing in them presented more of a problem. In order to minimize movement of the ribbon, it was kept as short as possible and one end was insulated from its support to prevent eddy currents flowing through it.
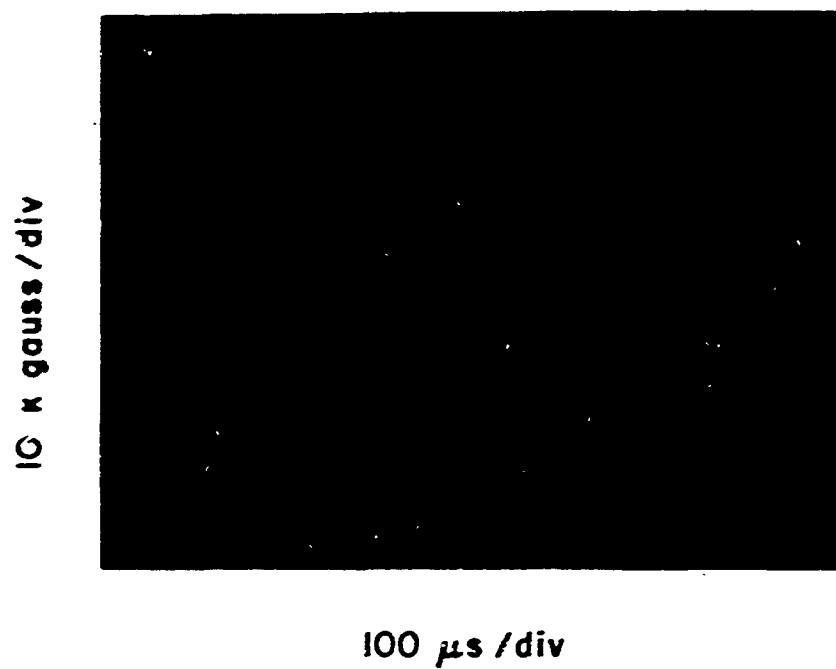
Figure 14. Magnetic Field Pulse, (a) With 3/4-in
Stainless Steel Rod Inserted in Magnet.
(b) Without Stainless Steel Insert.

III. DIODE EXPERIMENTS

The first emission experiments were performed with a simple
diode. This diode had a tungsten cathode ribbon which was 0.0005 in.
thick and 0.015 in. wide. The anode was of copper and could be moved
on its supporting tube to adjust the anode-to-cathode spacing. For
all the experiments, this spacing was 0.005 in. ± 0.0005 in. The
cathode ribbon was mounted in tension from two 0.010-in. thick
molybdenum lugs. The ends of the ribbon were sandwiched between the
two sides of a nickel strip that was bent around the ribbon, and
spot welds were made to the molybdenum lugs. These spot welds were
strong enough to hold the ribbon to the lugs, but could be stripped
off the molybdenum fairly easily, allowing the ribbon to be replaced
when necessary. The tube was mounted from a Varian vacuum flange
so that it could easily be removed from the vacuum system for
inspection and replacement of the filament. The pressure achieved
with this and subsequent tubes was about 10^{-7} Torr.

A. REPEATABLE CURRENT PULSES

Figure 15 shows some typical current pulses obtained with this
diode. They have been presented in this way to show that the results
were repeatable. This figure shows, as was expected, a mean emission
curve with a much slower and smoother rate of rise and fall of emission
than for the direct emission shown in Figure 1. There are however, a
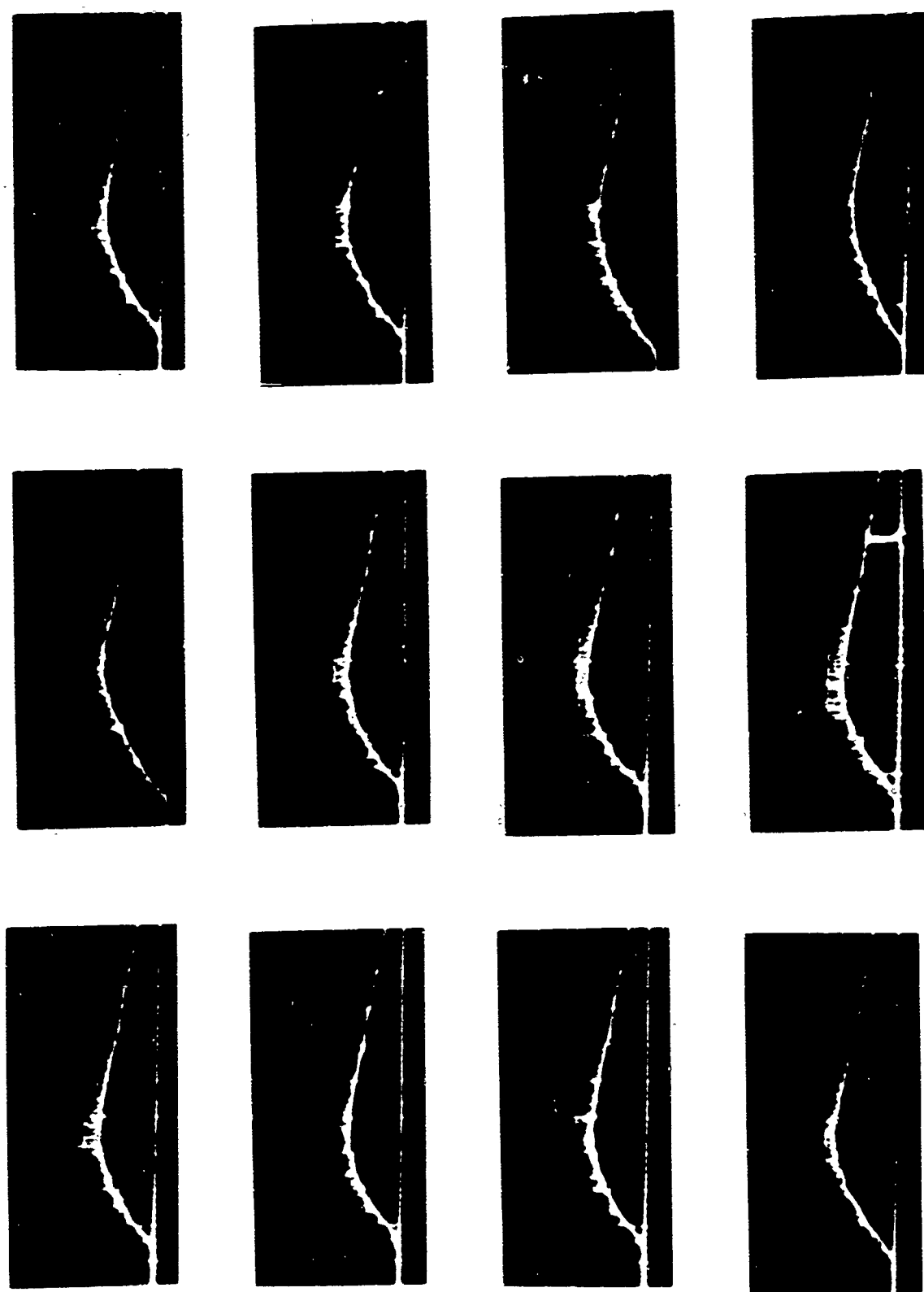
Figure 15. Diode Current-Time Curves Showing Repeatability. $v_a = 200v.$

10 mA/ div

50 μs / div

number of spikes superimposed on these curves. The average rates of rise and fall of emission compare well with theoretical values calculated by M. C. Chen.[8]

Figure 16a shows the variation of cathode current with anode voltage and Figure 16b shows the current as a function of the voltage at three different times during these pulses. Within experimental error, the current varied as the three-halves power of the voltages at the lower voltages, and there was saturation corresponding to temperature-limited emission at the higher voltages. The emission at lower voltages was mainly space-charge limited, but, because of the fall of temperature away from the center of the emitting area, the peripheral regions must have been temperature limited. The areas of temperature-limited emission and space-charge-limited emission depend on the laser input energy, the anode voltage, as well as the time from the beginning of the pulse. Chen's calculations show a very rapid fall of temperature, and therefore an even more rapid fall of emission, away from the irradiated spot, so that under space-charge-limited conditions, the emitting spot must be well defined.

The discussion of Figure 16 treats only the mean current curve and neglects the existence of current spikes that are superimposed on the mean curve. The variation of mean current with voltage has been interpreted as showing that the emission was space-charged limited, but the current spikes are obviously due to temperature fluctuations at the emitting surface produced by the spikes of laser energy. We therefore have emission which is space-charge limited in

20 ma/div

50 μs/div

(a)

200 μs

100 μs

450 μs

DIODE CURRENT (ma)
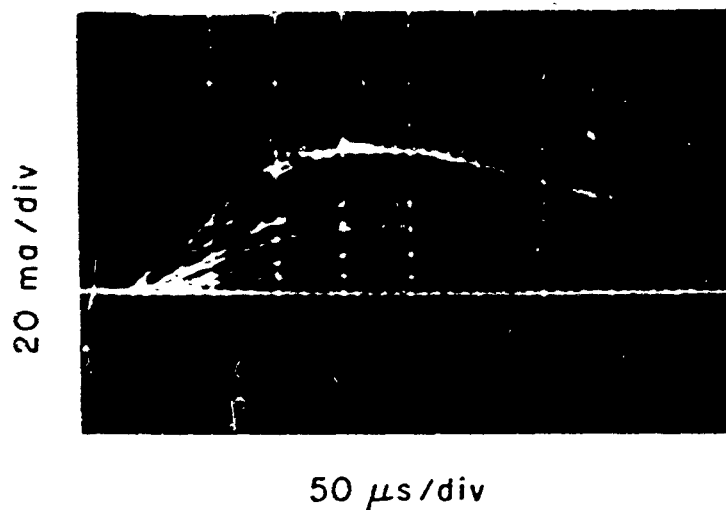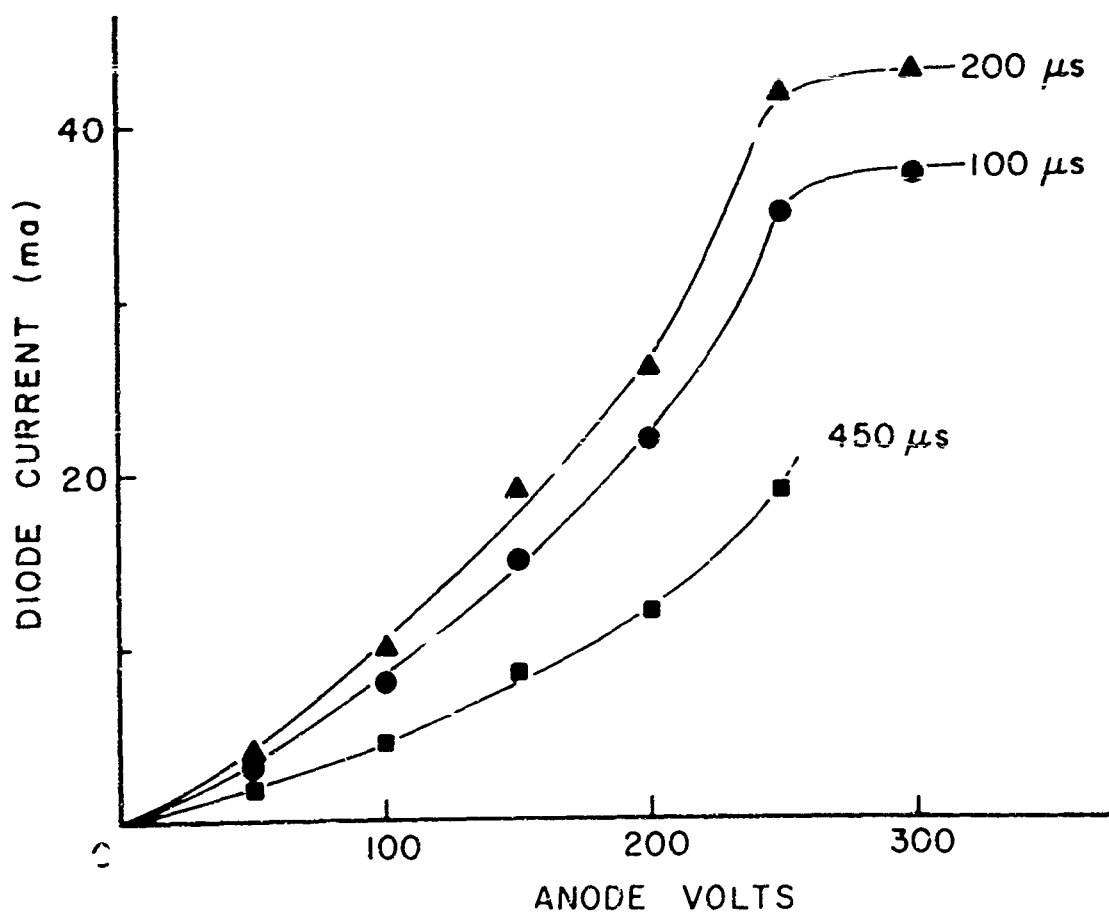
ANODE VOLTS

(b)

Figure 16.   (a) Diode Current at Several Anode Voltages; (b) Current-
voltage Curves from (a) at Different Times During Pulses.

the normally accepted sense, but which is also temperature dependent. This arises because the fluctuations of temperature are much greater than those with which one is normally concerned when treating a continuously emitting cathode.

This situation can perhaps be best understood in terms of Figure 17, which is an estimate of the shape of the equipotentials and field lines in a plane through the center of the beam. Immediately above the center of the emitting area is the usual potential barrier which exists under space-charge limited conditions. The height of this barrier depends on the temperature of the cathode. Only electrons with more than a certain energy can get over this barrier. However electrons can go around this barrier by spreading sideways. The shape of this barrier is a function of the cathode temperature and therefore the amount of beam spreading is dependent on the cathode temperature. In this way the anode current is dependent both on anode voltage and cathode temperature. Such a dependence of anode current on both anode voltage and cathode temperature is predicted for the infinite diode when electron emission velocities are taken into account, but the effect is much smaller than with the present arrangement. No attempt has been made to solve the case of the diode with finite transverse dimensions taking into account initial velocities, as would be required to correlate the changes in anode current with changes in the cathode temperature.

Before comparisons could be made with theoretical emission curves, it was necessary to know the emitting area and cathode current

ANODE

CATHODE RIBBON

——— EQUIPOTENTIALS

——— ELECTRIC FIELD LINES
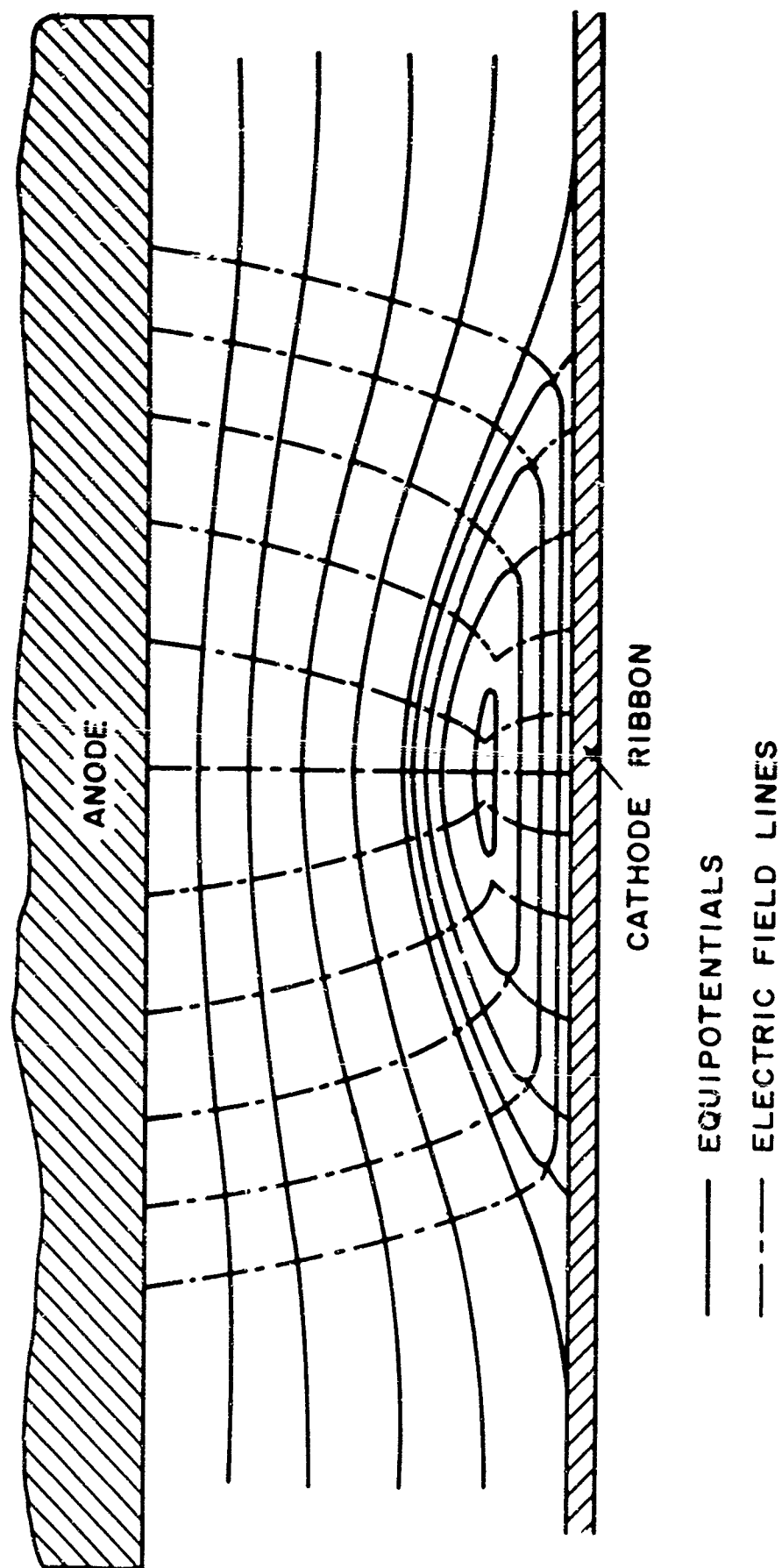
Figure 17. Equipotential and Field Sketch for Laser Diode.

density. The area of the emitting region could not be found from Figure 16 because the amount of spreading of the beam was not known. It was realized, however, that beam spreading could be prevented in the diode simply by applying the pulsed magnetic field developed for focusing a long electron beam. When this field was applied to the diode, current pulses of the kind shown in Figure 18a were obtained. A log plot of the maximum anode current as a function of voltage is given in Figure 13b. The slope of this curve is 1.4 ± 0.2, showing that, within experimental error, the current varies as the three-halves power of the voltage. The emitting area calculated from this curve using Child's law for an infinite diode and neglecting the effect of finite emission velocities of the electrons was $1.03 \pm 0.2 \times 10^{-6}$ cm^2. This corresponds to a circular region of diameter $0.0045 \pm .001$ in. which compares well with the value for the diameter of the intense central region of the beam at the cathode as discussed in Section II on the optical system. This was also the diameter of spots burned in a piece of film when placed in the cathode position. (Further evidence for these values for the diameter of the emitting region was given by the microphotographs of the ribbon after irradiation, which are presented in Figure 19. The peak current of Figure 18a was 3 ma, corresponding to a peak current density of 30 ± 6 a/cm^2 and therefore to a peak temperature over the emitting region of $3,125 \pm 25^\circ$K. This temperature is obtained from the data of Langmuir and Jones[9] for electron emission from tungsten. The peak current that could be obtained in a repeatable manner was 45 ma, corresponding to a current density of 450 ± 90 a/cm^2. This thermionic
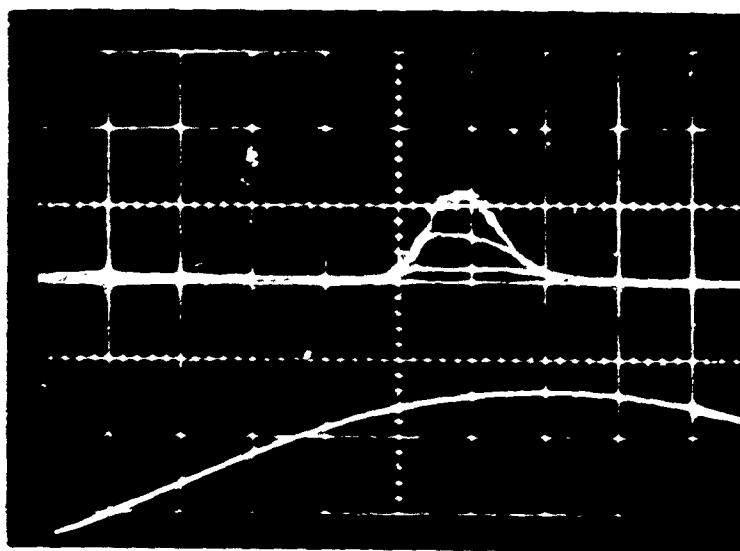
(a)
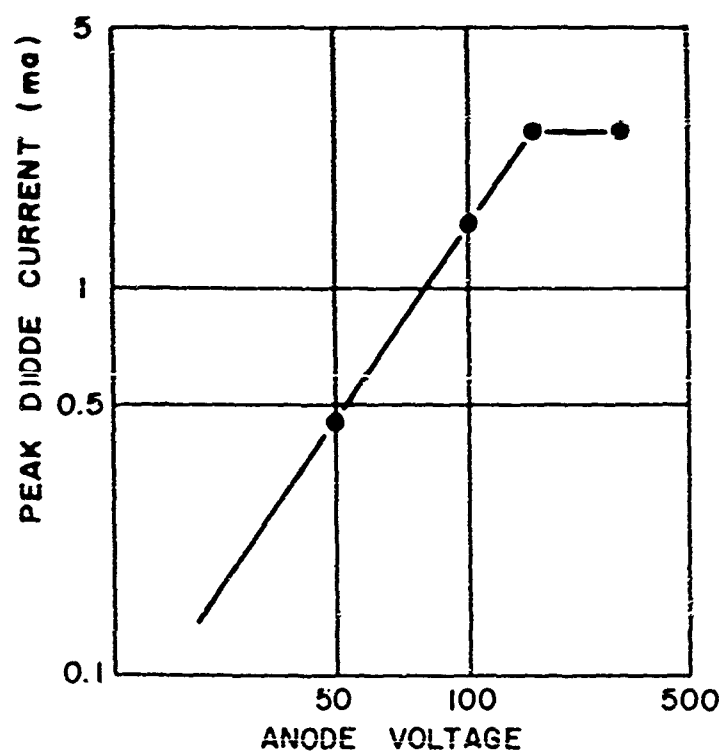
(b)

Figure 18. (a) Diode Current Pulses at Anode Voltages of
50v, 100v, 150v, and 250v with Magnetic Field
Pulses; (b) Log-Log Plot of Peak-Current versus
Voltage Obtained from (a).

current density is given by tungsten at 3,640 ± 30°K. The melting point of tungsten is 3,680°K. This therefore shows that the maximum repeatable emission was obtained when the temperature of the irradiated area was very close to the melting point of the tungsten and suggests that the effects observed when the laser energy was increased above the value which gave this maximum repeatable current were due to the irradiated area melting.

When the magnetic field was applied to the diode, as has been pointed out already, the beam was prevented from spreading. This reduced the anode current for a given anode voltage and led to the almost complete suppression of the current spikes observed when no magnetic field was applied. This is consistent with the explanation of the spikes given earlier. Once the beam is prevented from spreading, there is very little variation of current with cathode temperature under conditions of space-charge-limited emission.

The energy per laser pulse incident on the ribbon that produced the maximum repeatable electron current pulses was 0.03 joules. In Appendix B the value for the reflection coefficient of tungsten, when irradiated with ruby laser light at normal incidence, was found to be 0.56. If this value is correct, then 0.014 joules of the incident energy were absorbed and 0.016 joules were reflected. The figure of 0.014 joules absorbed is to be compared with the value of 1.7×10^{-3} joules required to raise the temperature of a 0.005-in. diameter region of the ribbon from room temperature to the melting point of tungsten. The mass of this region of the ribbon is a mere

3.1×10^{-6} gm. A further 0.8×10^{-3} joules would be required to melt this mass of tungsten at constant temperature. The total energy required to melt the emitting area of the ribbon is therefore 2.5×10^{-3} joules, which is a factor of 5.6 less than the energy absorbed per pulse. The reason for this apparent discrepancy is that not all the laser energy was incident on the emitting area. At the cathode the laser beam had an intense central region of 0.005-in. diameter surrounded by a region of lower intensity. The diameter of this less intense region was approximately 0.015 in. Since the exact distribution of incident energy over the irradiated spot was not known, it was not possible to calculate the temperature distribution that should have been achieved; however, the value of the incident energy is consistent with the emitting region being raised to a temperature near the melting point of tungsten.

Figure 19 shows both sides of the tungsten ribbon after 1, 4, and 16 laser pulses. Unfortunately these were produced before the laser energy measurements had been made, which showed that forced air cooling was necessary to achieve a constant output energy per pulse. The laser was here fired every 100 sec with no forced cooling. Figure 8 shows that under these conditions the laser output falls with pulse number and reaches an equil brium value that is only half the energy of the first pulse. For the one and four pulses the energy of at least the first pulse was sufficient to melt the irradiated area. As can be seen from the photographs the diameter of this region is close to 0.005 in. confirming the figure found earlier for

After 16 shots

After 4 shots

After 1 shot
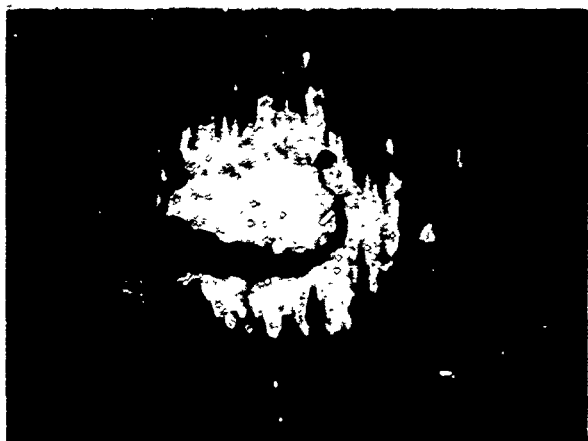
Irradiated Side
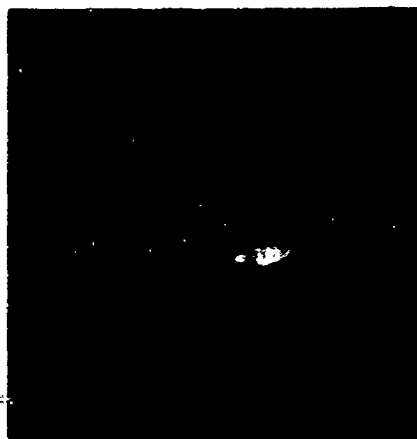
Emission Side

.005"

Figure 19. Tungsten Cathode After Irradiation.

for the diameter of the emitting area. For the 16-shot sequence the first shot was fired only 200 sec after an 8-shot sequence. The crystal did not have time to cool completely and therefore even for the first shot of this sequence the laser energy was not sufficient to melt all the irradiated area. Only the central 0.002 in. was melted. The dark areas on these photographs are not craters or holes but regions with a very smooth surface which reflected little light into the microscope. On the irradiated side there appears to be a mound. This may be due to the extremely rapid cooling of the metal after melting, leading to a microcrystalline or even anisotropic form of tungsten with a lower density than normal crystalline tungsten. These photographs of the cathode after irradiation show that it was possible to melt the central region of the ribbon without destroying the cathode.

Figure 20 shows some of the current pulses corresponding to the shots of Figure 19. Figure 20a is the current pulse corresponding to the single laser shot. This pulse, like all first pulses in any area of the cathode, produced a large burst of gas from the surface and interior of the tungsten. This burst of gas was sufficient to produce a gas breakdown and a consequent large current of peak value 1 A. The breakdown was not quite an arc, since for an arc the voltage across the tube would have been small and the peak current would have been 2A limited only by the circuit resistance. Since the tungsten was molten for at least part of the pulse, evaporating tungsten may have contributed to the possible gas processes. The current pulses of Figure 20b correspond to the second, third, and fourth shots of the

(a) 0.5 a/div

(b)

(c) 10 ma/div

100 μs/div
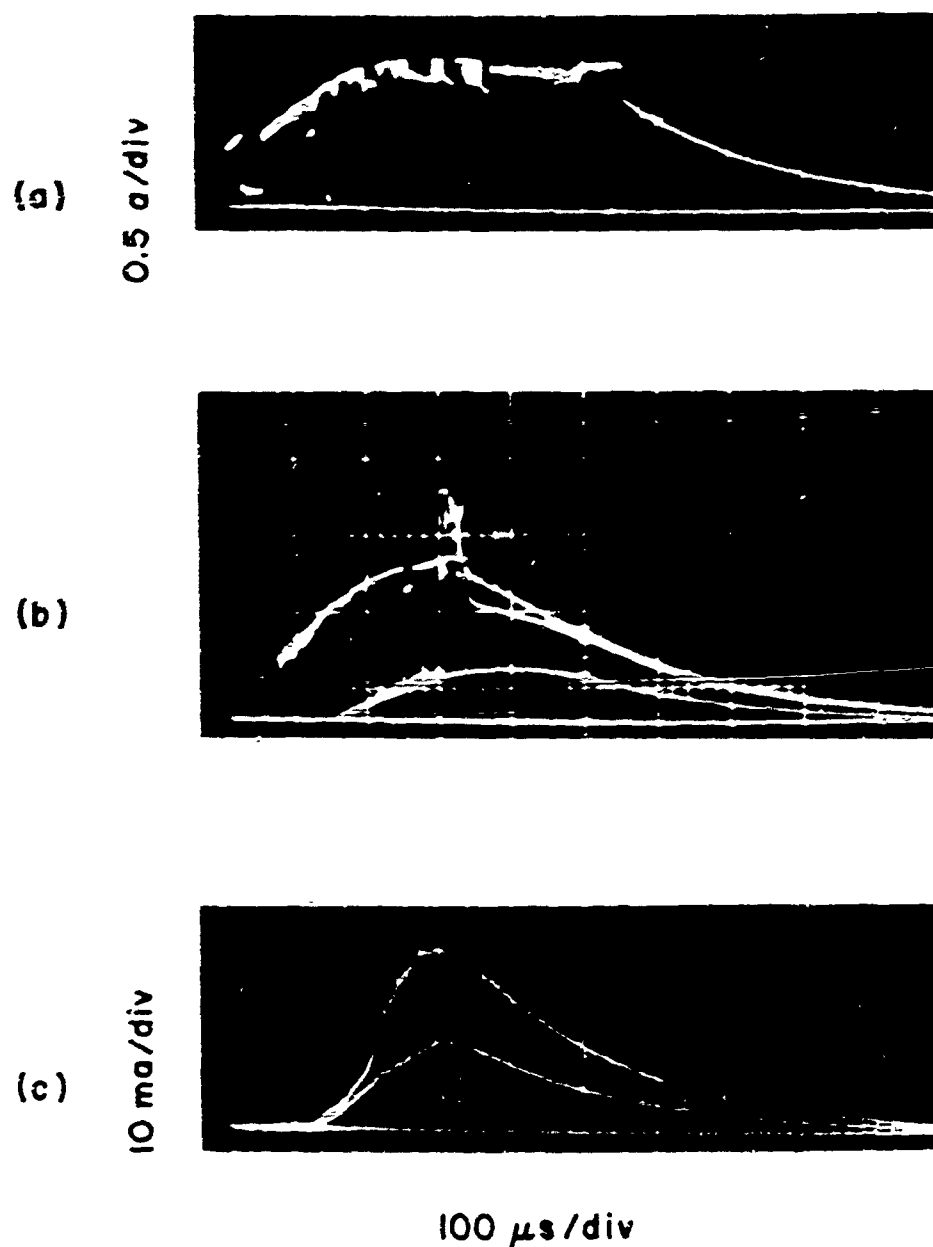
Figure 20. Current Pulses Emitted from Cathode Area Shown
in Figure 19. (a) Corresponding to Single Shot;
(b) Corresponding to Second, Third, and Fourth
Shots of Four-Shot Sequence. Vertical Scale is
0.5a/div for Second Shot and 20 ma/div for Third
and Fourth Shots. (c) Corresponding to Fourth
and Eighth Shots of Sixteen-Shot Sequence.

four-shot sequence. The vertical scale for the upper curve is 0.5 a/cm, which is similar to Figure 20a. The vertical scale for the other two curves is 20 ma/cm. The emission here has reached the stable condition, that is the nonbreakdown condition by the fourth shot. Figure 20c shows the fourth and eighth shots of the 16-shot sequence. The reduction in current is due to the reduction in laser energy. Again the emission had reached the stable condition by the fourth shot and all subsequent shots gave the same shape of curve.

The results presented so far admit of a simple explanation. The tungsten is heated to its melting point or close to this by the laser energy that is concentrated in a spot of about 0.005 in. diameter. The electron emission from this spot is well-understood thermionic emission that can give up to about $450a/cm^2$ in a repeatable manner. The cathode ribbon, which is not processed in any way before mounting in the tube, is outgassed by the first few laser pulses accompanied by large cathode currents. After the first few pulses, there is little further emission of gas, and the electron emission becomes stable.

B. NONREPEATABLE AND BREAKDOWN CURRENTS

Figure 21 shows what happened when an attempt was made to achieve higher current densities by increasing the laser energy. Here the energy is increased by 5 per cent from one curve to the next. The lower curve of Figure 21a corresponds to the smallest laser energy. At a current of 45 ma the current suddently jumps to an appreciably higher value. Figures 21b and 21c show the current pulse resulting
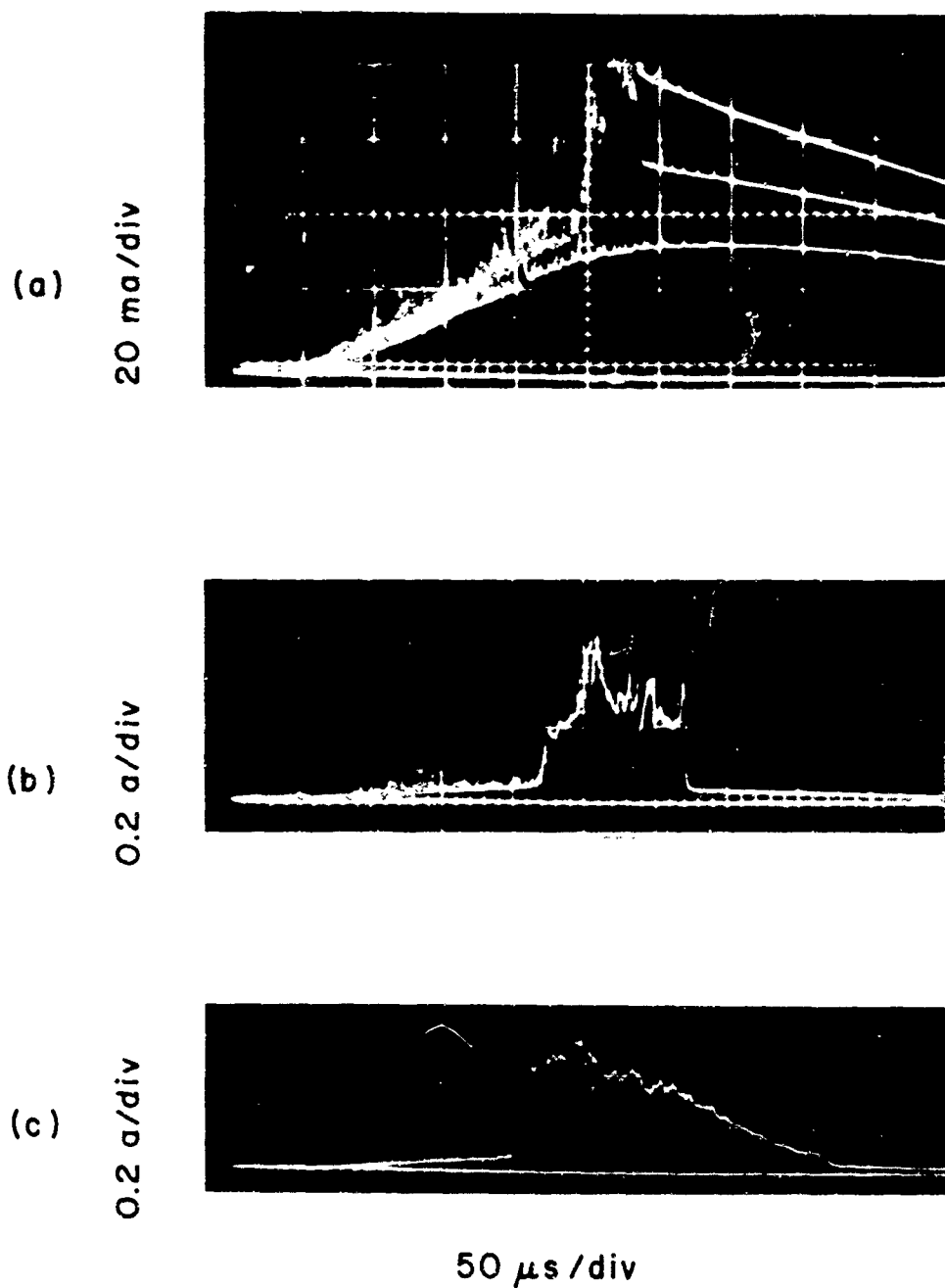
Figure 21. Diode Current Pulses Showing Transition to Very High Current Density Emission. Laser Energy Increased: (a) 5 Percent for Each Pulse; (b) 5 Percent Above Top Curve of (a); (c) 5 Percent Over Curve in (b).

from two subsequent 5 per cent increases in the laser energy. The current scale changes from 20 ma/div to 200 ma/div. Here the breakaway from the smooth curve at about 45 ma can clearly be seen. The peak current reached was about 400 ma corresponding to a cathode current density of 4,000 a/cm^2. The anode voltage for all these curves was only 250 v and no magnetic field was applied, so that the beam could spread and thus reduce space-charge depression. The conduction across the diode of such a large current must, however, involve some degree of space-charge neutralization by ions. A possible explanation of these results is that the lower repeatable currents were obtained up to the melting-point of tungsten, and that the break from the curve occurred as the tungsten melted. The rate of evaporation of atoms from the surface increased appreciably at this point and provided sufficient ions to give space-charge neutralization. The work function of the metal might also change appreciably at the melting point, as would certainly be expected, since the work function depends on the structure of the metal, and it is this which changes at the melting point. If the work function did change, the available electron emission would suddenly rise at the moment the tungsten melted, and this together with the increased ion emission to provide space-charge neutralization would fit the observed results. More work on this aspect of the emission is necessary in order to provide a better understanding of the processes that occur.

Currents of Figure 21 were obtained with an anode potential of only 250 volts. An attempt to increase the diode current under these

conditions by increasing the anode voltage led to the current curves of Figure 22. Here the vertical scale is 2 a/div compared with 0.2 a/div for Figure 21b, c. As can be seen from Figure 22b, c, the current rises to a large value at a time in the pulse that depends on the anode voltage. The voltage across the tube does not fall to a small value immediately with this current jump, but slowly decreases as the current increases. About 100 µs after the peak current has been reached and thereafter, the voltage across the tube is small and the current is determined only by the circuit resistance and capacitance. This is a gas breakdown process which is probably due to the evaporation of tungsten in the form of neutral atoms and ions from the cathode surface. After the initial breakdown the large power dissipation at the anode should produce intense surface heating, which would evaporate material from the anode and could contribute to the formation of an arc. The repeatability of these results, which can be seen in Figure 22a, is quite remarkable.

These results are interesting in that an arc was formed in the diode in a controlled and repeatable manner. More work is required to determine whether the process is entirely dependent on the cathode or whether the anode plays a part in the process. This may be of use in certain switching applications. It may also prove interesting to investigate the extremely high-density plasma that must exist in this arc. If we assume no spreading of the beam from the initial 0.005 in. diameter, then the electron plasma frequency at 750 v is 7×10^{12} cps. Even an order of magnitude less than this would be
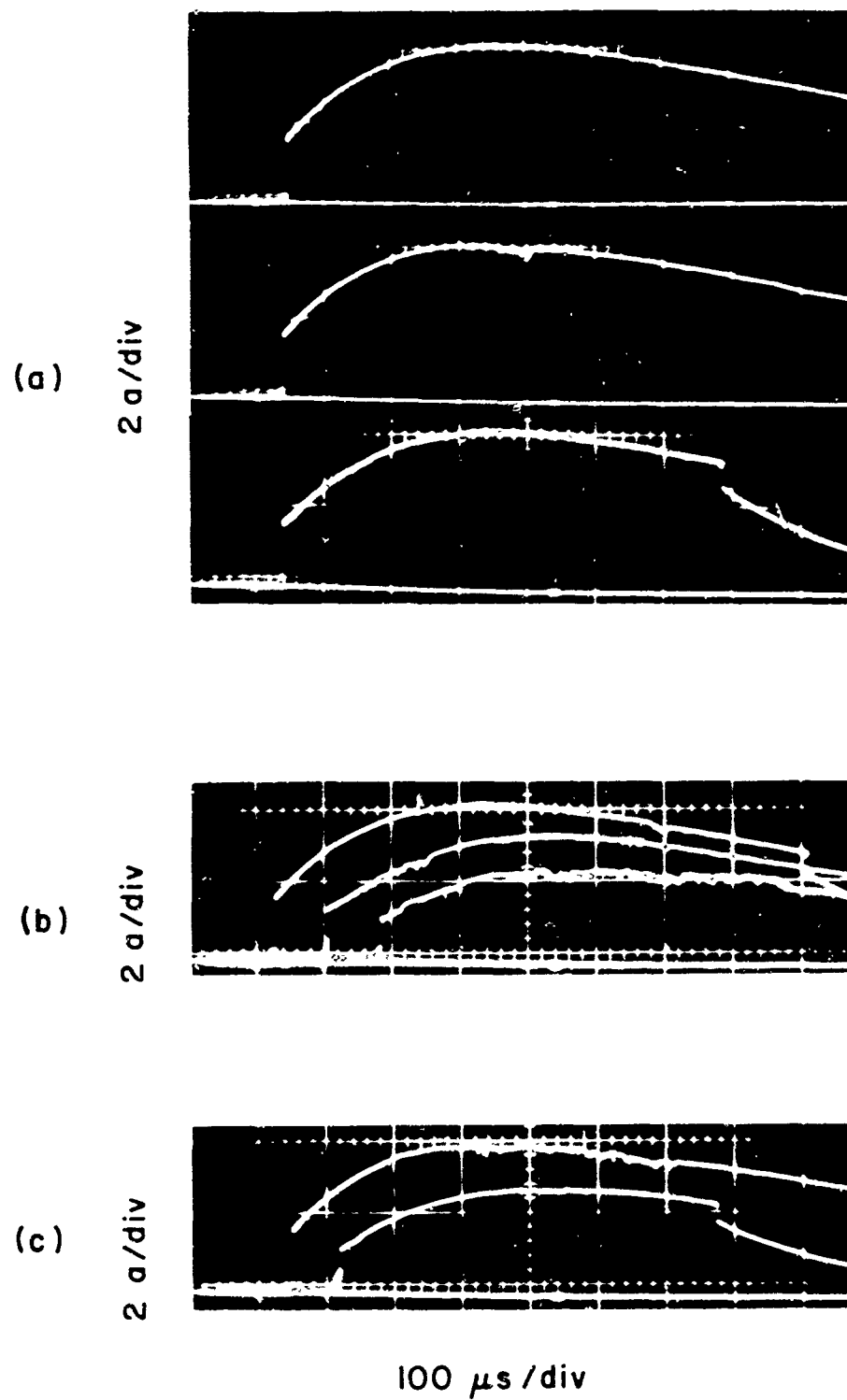
Figure 22. Diode Current Under Breakdown Conditions:
(a) $V_a = 750v$; (b) $V_a = 750v$, $600v$, and
$500v$; (c) $V_a = 750v$ and $600v$.

700 Gc/s. Present interest in the generation of millimeter and submillimeter waves may make further investigation of this plasma arc worth while.

C. SUMMARY OF CHARACTERISTICS OF DIODE EMISSION

When the cathode was irradiated with sufficient laser energy to bring the irradiated spot close to the melting point of tungsten, repeatable current pulses of up to 450 a/cm^2 were obtained. Increasing the laser energy lead to higher current densities that were not repeatable; then increasing the voltage lead to breakdown above 500v anode potential with the current limited only by the circuit resistance and capacitance. This breakdown could, however, be initiated in a well=controlled manner.

Langmuir and Jones[9] data on tungsten is available for temperature up to $3,655^\circ$C. At this temperature the electron emission is 480 a/cm^2, and the atom emission is 2.28×10^{-4} gm/cm^2/sec. This atom emission corresponds to about 10^{-5} cm/sec., and since the ribbon is 10^{-3} cm thick the maximum lifetime would be 100 sec. There is evaporation from both sides of the ribbon, however which would certainly be greater from the irradiated side than the emission side. A lifetime of 10 sec would therefore be expected. With a duty ratio of 0.001, this would be increased to about three hours, which is very short, in terms of the lifetime of useful devices. It should not be too difficult to move the ribbon periodically, however, exposing a new portion of the ribbon to the laser beam at regular intervals. In

this way the lifetime could be made very much longer. A length of about 20 cm of ribbon would give a lifetime of 30,000 hr. In a device that required a very high current density beam, this approach of using a laser-irradiated cathode could be very worth while in spite of the necessity of moving the ribbon periodically.

No attempt was made to determine the lifetime of the ribbon experimentally, since the figure of 10 sec corresponds to 10^5 pulses. Checking this in a reasonable length of time would have required a laser that could be pulsed at rates from several pulses per second to several tens of pulses per second. Although lasers that can be pulsed at these rates have been produced, the laser available for these experiments could be pulsed at a maximum rate of only several pulses per minute.

IV. FORMATION OF LONG BEAMS

Since repeatable electron emission of up to about 450 a/cm^2 had been obtained with the diode, two simple beam testers were designed to show that high current density long beams could be produced. These are shown schematically in Figure 23. Beam tester A consisted of a tungsten ribbon cathode (as used for the diode) spaced 0.005 in. from a molybdenum anode. This anode was 0.02 in. thick and had a hole in it of the form shown in the figure. The diameter of this hole on the side facing the cathode was 0.005 in. A collector was placed behind the anode.

This simple gun produced a small-diameter beam from which information was obtained on the fraction of the beam that passed through the anode aperture to the collector and the fraction intercepted by the anode. No information could be obtained, however, about the behavior of the beam after it passed through the anode. Beam tester B was therefore built to show that the high current density beam could be passed through a tube that had a reasonable length-to-diameter ratio. The cathode-to-anode spacing for this tube was again 0.005 in. and the internal diameter of the anode drift tube was 0.01 in. This tube was in fact a stainless steel hypodermic needle brazed into a stainless steel block. The length of the tube was 0.15 in. giving a length-to-diameter ratio of 15. When the beam had passed through the drift tube it was collected with the same collector used for beam tester A.
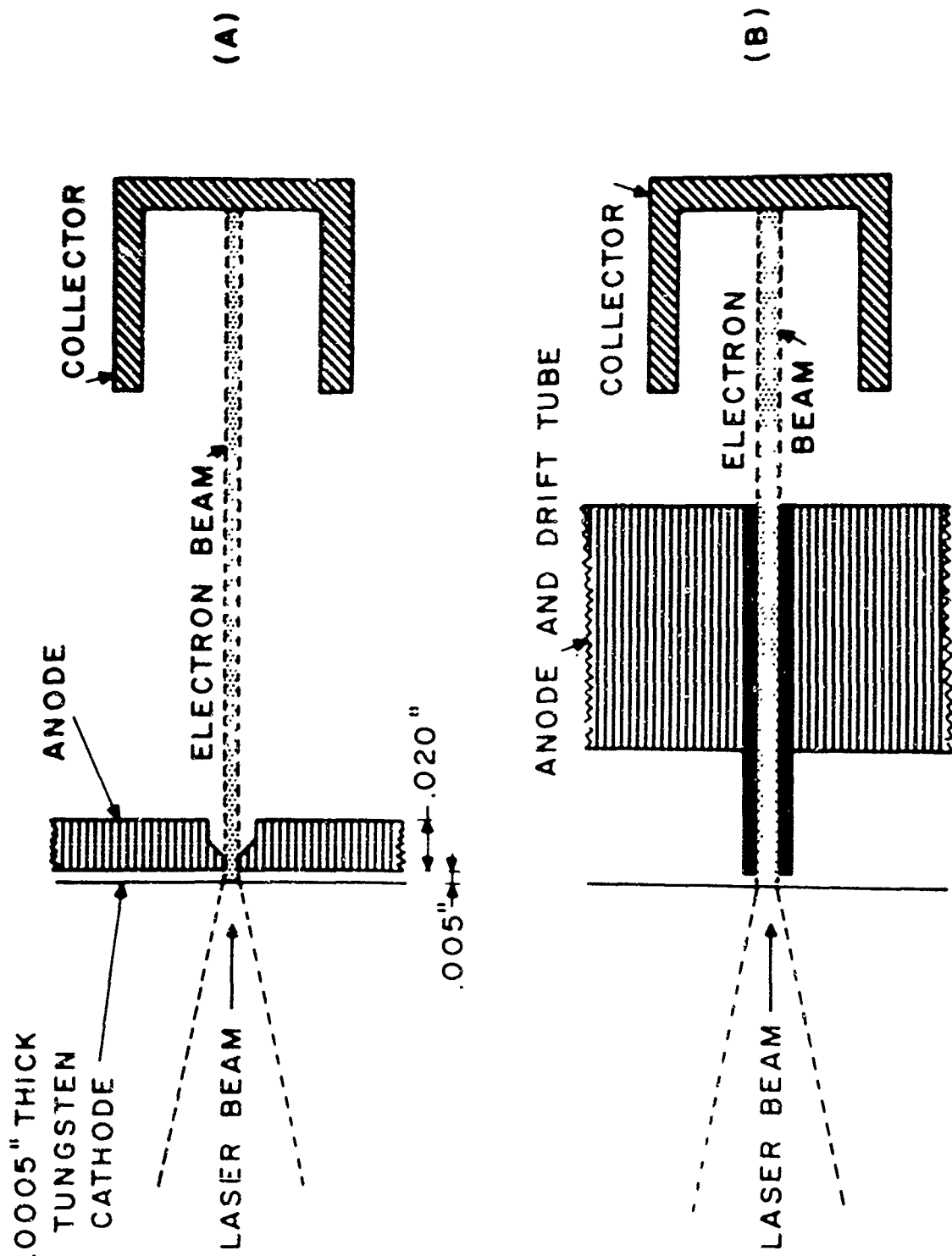
Figure 23. Laser Cathode Beam Testers.

The laser beam targets for the two beam testers is shown in
Figure 24. The target was viewed through the glass port through
which the laser beam enters the vacuum system. As Figure 24 shows,
the cathode ribbon covers the anode aperture in each case. There
was therefore a slight problem in irradiating the cathode so that the
irradiated area and the center of the anode aperture coincided. Two
slightly different techniques were used.

For beam tester A the position at which the laser beam would
strike the target was adjusted by eye. This was done by shining a
light on the end of the laser housing and crystal so that an image
could be seen on the cathode ribbon. The center of this image was
made to coincide with the target as closely as could be estimated by
using the telescope micrometers. This set the laser beam within a
few thousandths of an inch of the required position. The laser was
then fired with the voltages applied to the tube. Some of the beam
passed through the anode to the collector and some was intercepted
by the anode. The laser beam was moved systematically about this
position until the position of minimum interception of the beam by
the anode was found. Once this position had been found, the tube was
pulsed with the magnetic field applied, and most of the emitted
current passed through the anode to the collector.

For beam tester B the technique was the same, except that when
the tube was pulsed with no magnetic field applied, none of the
current passed through the tube to the collector. The 0.01 in.
diameter of the tube, which served both as anode and drift tube,

-121-

BEAM TESTER A

MOLYBDENUM
ANODE

LASER TARGET

TUNGSTEN RIBBON
CATHODE

BEAM TESTER B

ANODE - DRIFT TUBE

LASER TARGET

CATHODE RIBBON
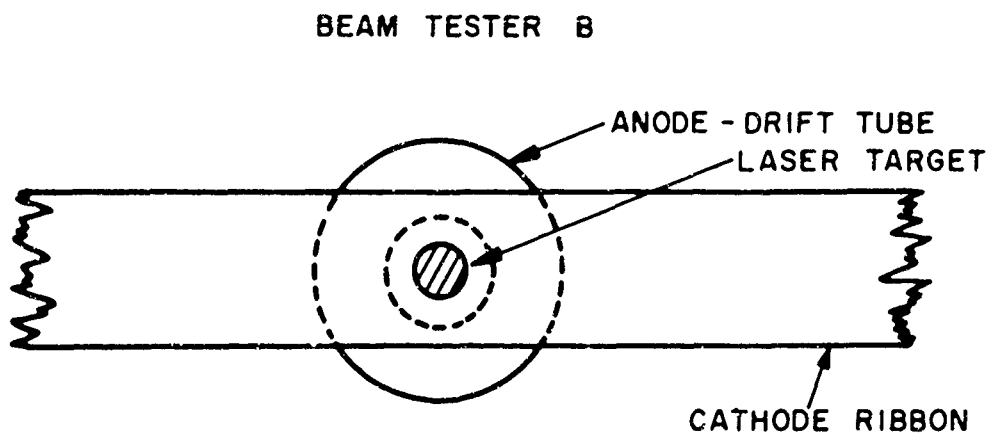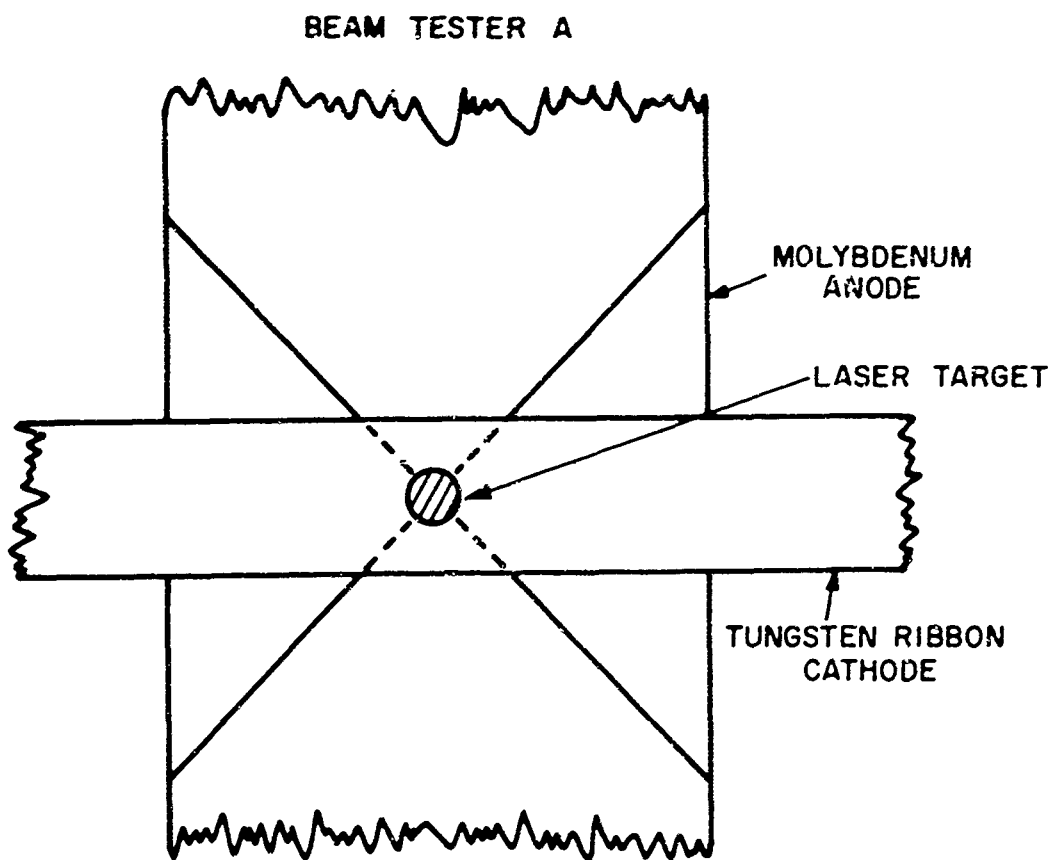
Figure 24. View of Laser Beam Targets.

was large compared with the anode-to-cathode spacing of 0.005 in., so that the electric field at the cathode was smaller opposite the center of the tube than opposite the edges of the tube. As the laser beam was moved about the cathode in small steps, the current pulse decreased when the irradiated spot moved towards the center of the tube. The central position was therefore found by finding the position of minimum cathode current with no magnetic field applied. When this position had been found, the laser was fired with the magnetic field pulse applied to the tube and most of the emitted current then passed through the drift tube to the collector.

Figure 25 shows the maximum current pulse obtained without break-down for beam tester A. The peak emission current was 60 ma of which 50 ma passed through the anode to the collector, the remaining 10 ma being intercepted by the anode. The beam transmission through the anode was therefore 85 per cent. This current pulse was obtained with a 500-v anode voltage and therefore the maximum beam perveance was 4.5×10^{-6}. This perveance is appreciably higher than the perveance of beams used in most microwave device applications. The current pulse shown in Figure 25 is somewhat jagged. This was found to be due to misalignment of the telescope, which resulted in some of the laser spikes being transmitted by the optical system with less attenuation than others. The effect of these spikes was thus enhanced and the temperature fluctuations at the cathode were increased, producing the jagged emission pulse. As a result of this, the method discussed in Section II for aligning the system was developed.

Collector 25 mA/div

Anode Current 10 mA/div
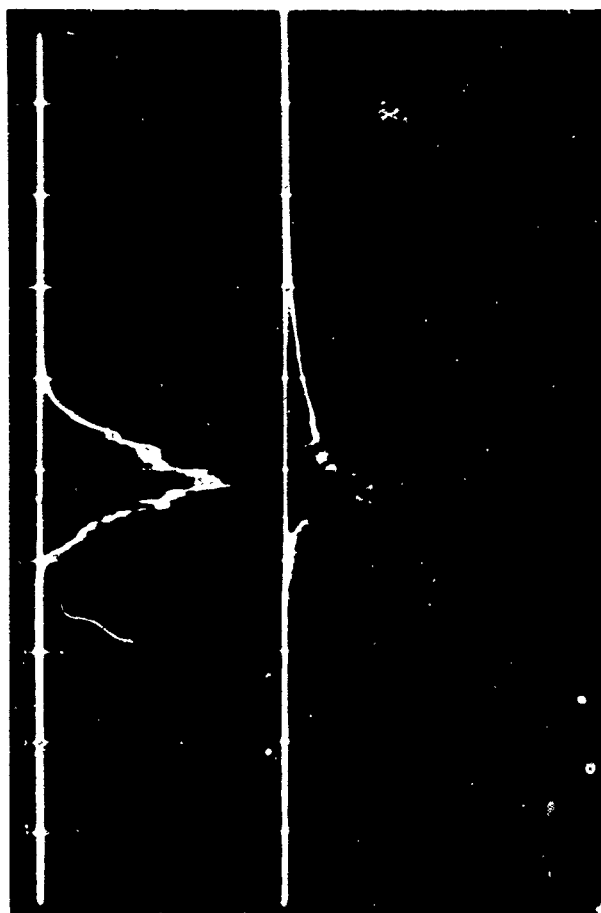
100 μs/div

Figure 25. Typical Current Pulse for Beam Tester A.

Figure 26 shows the result of increasing the laser energy in an attempt to obtain more emission. The current suddenly increased after it had reached 50 ma. This result is exactly the same as was observed for the diode when the laser energy was increased above the level that gave 45 ma peak current. As suggested in Section III on diode experiments, this sudden increase in current probably coincided with the melting of the emitting area.

Figure 27 shows the variation of anode and collector currents with anode voltage. There is an approximately three-halves-power variation of current with voltage up to 200 v on the anode above which there is little increase of current with voltage. Under space-charge-limited conditions there are virtually no current fluctuations resulting from temperature fluctuations at the cathode. As the anode voltage is increased and the emission becomes temperature limited, the current fluctuations increase in magnitude.

Figure 28 shows typical anode and collector current pulses obtained with beam tester B. The peak current passing through the drift tube was 30 ma with only 2 ma to the drift tube. This corresponds to a beam transmission through the drift tube of 94 per cent. The anode voltage was 600 v and therefore the beam perveance was 2.0×10^{-6}. If uniform current density in the beam and a diameter ratio of 2 is assumed between drift tube and beam, then Equation (26) shows that the outer edge of the beam would be a potential 4.4 percent or 26 v below that of the drift tube and that the axial electrons would be at a potential 1.6 per cent or 9.6 v below the potential of the outer

25 ma / div
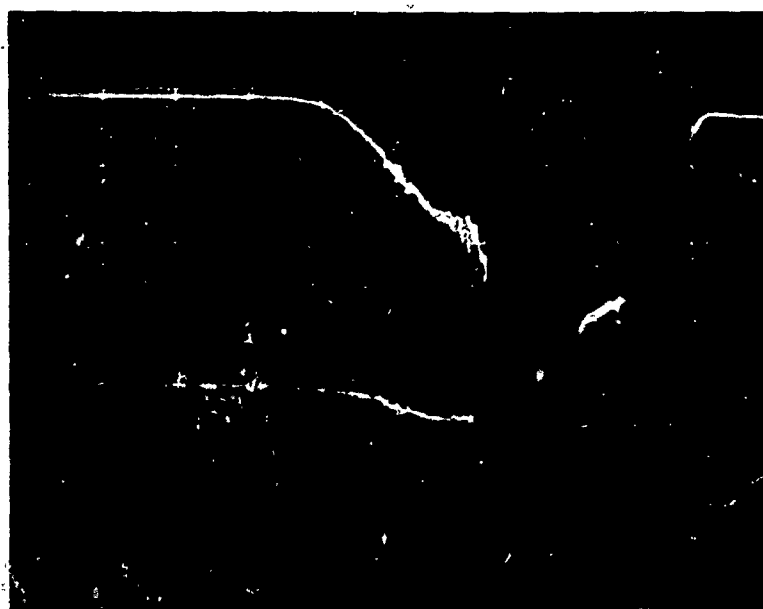
100 μs / div

Figure 26. Current Pulses for Beam Tester A Under Breakdown Conditions. Upper Trace is Collector Current. Lower Trace is Anode Current.

Anode
Current

Collector
Current

$V_a = 50\ V$

100 V

150 V

200 V

300 V

400 V

500 V
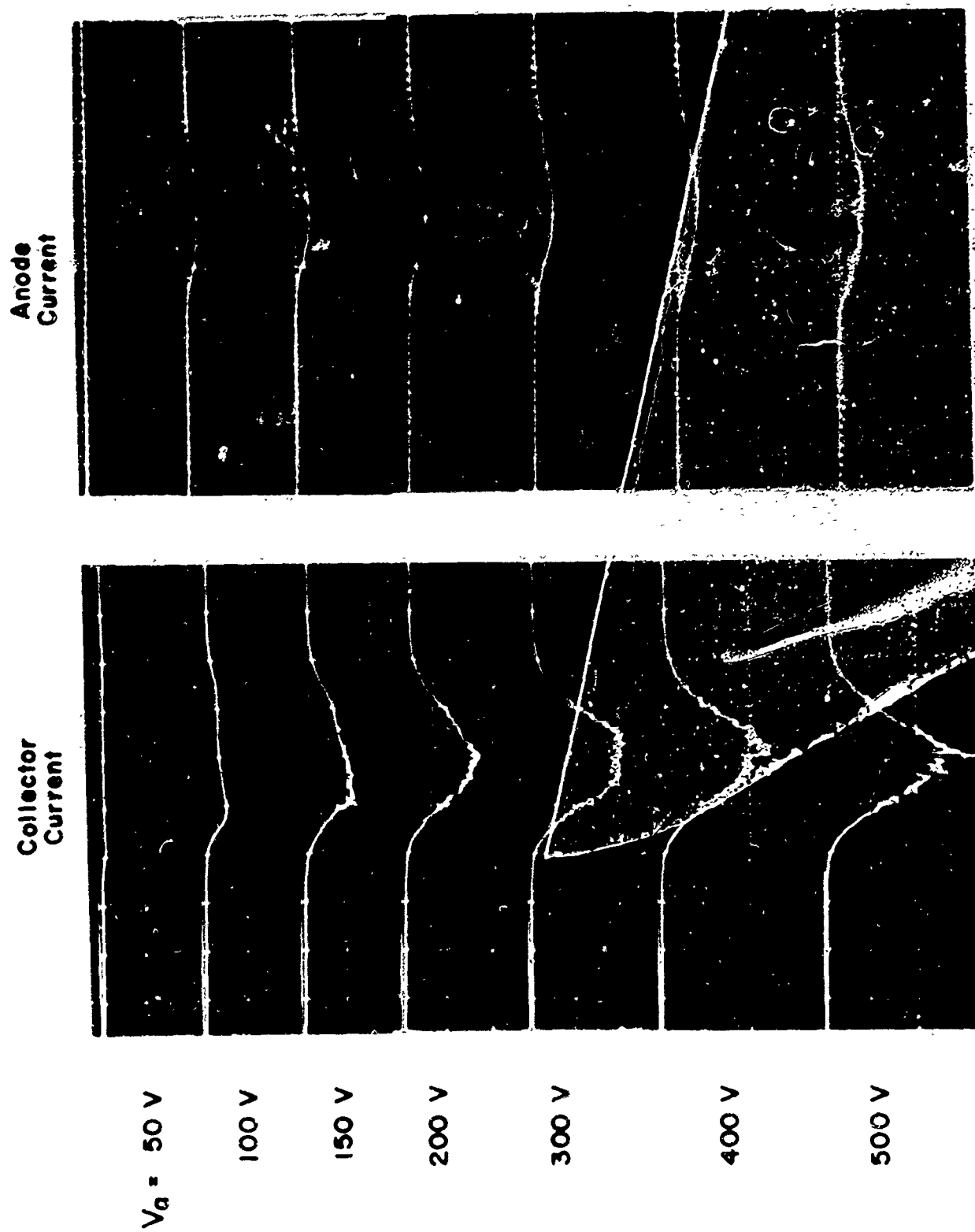
Figure 27. Beam Tester A. Collector and Anode Currents at Several Anode Voltages. $V_c = V_a + 300v.$

Anode and
drift tube
current

10 mA/div

Collector
current

100 μs/div

Figure 28. Typical Current Pulse for Beam Test...

electrons. The Brillouin field for this beam was therefore 4,680 gauss.

When the magnetic field was pulsed at the Brillouin value, most of the current was intercepted by the tube, serving as both anode and drift tube, and only 10 per cent was transmitted to the collector. When the magnetic field was increased to twice the Brillouin field, however, the high transmission shown in Figure 28 was obtained. Increasing the magnetic field to four times the Brillouin field, that is to $18,700$ gauss, resulted in no further change in beam current or beam transmission.

From Equations (18) and (22) we find that with $B_z = B_B$ and $k = 2$; then $\sim$ $1/2$ and $r_{max}/r_{min} \sim 3.0$. The mean diameter of the scalloping beam would therefore be 0.01 in., which was the diameter of the drift tube, and the maximum diameter of the beam would be 0.015 in. This fits in well with the fact that most of the current was intercepted by the drift tube under these conditions. Increasing the magnetic field to $2B_B$ gives $r_{max}/r_{min} \sim 1.12$; therefore the maximum diameter of the beam would be about 0.0055 in. This again fits the experimental data that under these conditions the interception of the beam by the drift tube was small. Further increase in the magnetic field reduces the scallop ratio and therefore should affect the interception only slightly, if at all. From this it can be seen that the behavior of the beam was as predicted theoretically and that the required focusing field was about 10,000 gauss.

The effect of increasing the laser energy above the value which gave the pulse of Figure 28 is shown in Figure 29. The beam current

(a) 20 ma/div

(b) 20 ma/div

100 μs/div
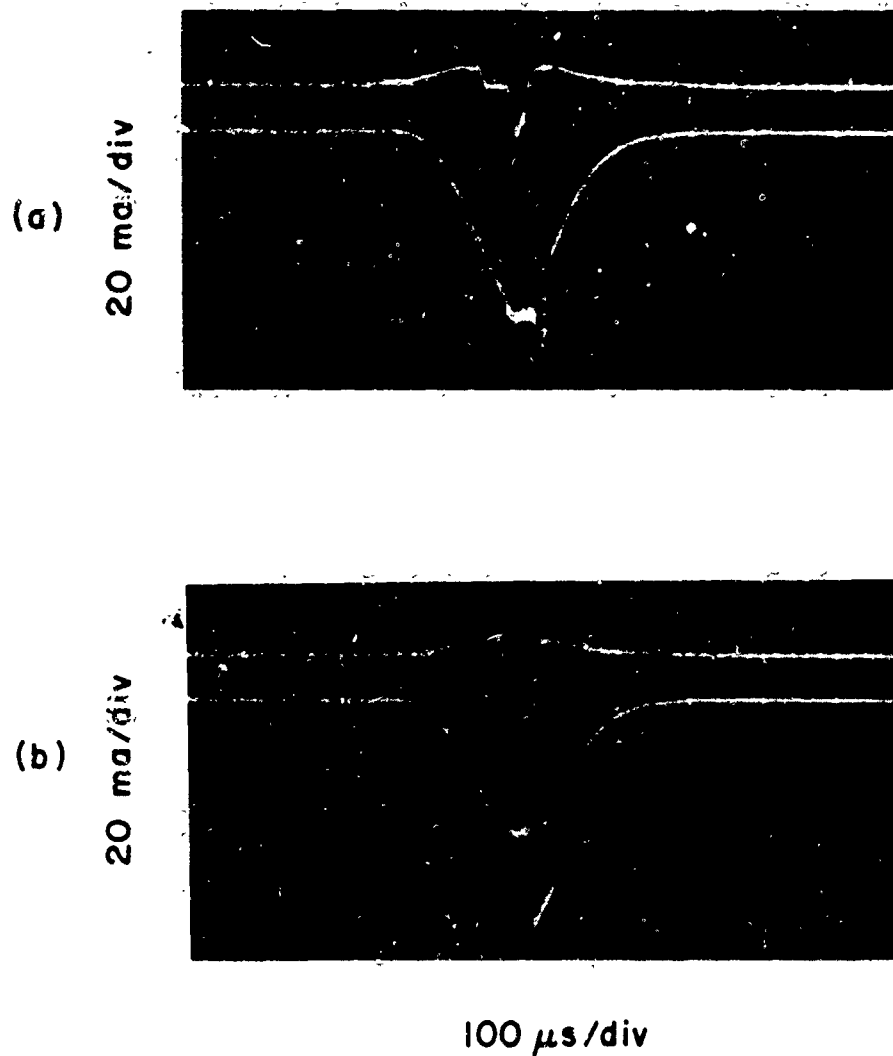
Figure 29. Current Pulses for Beam Tester B. Upper Traces
are for Anode (and Drift Tube); Lower Traces
are for Collector. (a) V_a = 570v, V_c = 800v;
(b) V_a = 600v, V_c = 800v.

increased but at some time during the pulse there was a sudden increase
in the collector current and an equal and opposite change in the
collector current. (These changes appear separated by 30 μs in
Figure 29 but this is due to one of the traces being displaced with
respect to the other). These discontinuities are due to a gas
discharge in the region between these two electrodes. A discharge of
the Penning type is likely to form fairly readily in this region
because of the strong axial magnetic field and the high current density
in the main electron beam.

V. CONCLUSIONS AND RECOMMENDATIONS

The aim of this work was the investigation of indirect emission from a laser-irradiated tungsten cathode, since it was thought that this would give much smoother current pulses than those given by direct emission. This has been found to be the case. Smooth repeatable current pulses of up to 450 a/cm^2 have been obtained from such a cathode and it is thought that these repeatable current pulses were emitted by the cathode when the temperature of the emitting surface was below the melting point of tungsten. The high current density emission obtained when the laser energy was increased above the value that gave the repeatable results has not been studied in any detail, mainly because breakdown occurred very readily under these conditions. Two beams were formed using indirect emission from a laser cathode. These beams, which were focused by a pulsed magnetic field, had current densities up to the repeatable value of 450 a/cm^2 and were of high perveance. High current density beams produced in this way may find application in the generation of millimeter waves.

This study of indirect emission from a laser cathode is part of a larger study of the feasibility of producing high current density electron beams by irradiating metals with a laser beam. As pointed out in the introduction, the laser pulse used for the experiments consisted of about 100 separate spikes and indirect emission was used to average out the effect of these separate spikes. Laser pulses can now be produced, however, which consist of a single spike instead of.

a train of spikes. Pulses of this kind were produced using the technique of Q spoiling. These pulses can be produced with repeatable amplitude and length and therefore may produce repeatable electron emission of very high intensity directly from the irradiated surface. If this proved to be the case, then the beams produced may be more useful than those produced by indirect emission. The next step in this program will therefore be a study of electron emission from metal surfaces when irradiated by the single pulses from a Q-spoiled ruby laser. When this stage of the program has been completed, it will be possible to make a comparison of the relative merits of the beams produced by each method and therefore to decide which is the best for a particular device application.

APPENDIX A, MAGNETIC-FIELD FOCUSING OF LONG ELECTRON BEAMS

In order to focus the high current density beams produced by emission from a laser cathode, it is necessary to use a strong magnetic field. Two principal methods for focusing a beam using a magnetic field are Brillouin focusing and confined focusing.

When using Brillouin focusing the beam is injected from a field-free region into the focusing field. For confined focusing the gun is immersed in the focusing field. Each method has its advantages.

1. BRILLOUIN FOCUSING

Consider a beam of uniform current density with no angular variation of field or beam parameters. This beam is injected from a cathode at which the magnetic field is B_O into a region in which the magnetic field is B_z.

The Lorentz force equation for an electron a distance r from the axis is

$$\ddot{r} - r \dot{\theta}^2 = - \eta(E_r + B_z r \dot{\theta}) \qquad (3)$$

where η is the charge-to-mass ratio for an electron, $\dot{\theta}$ is the angular rotation frequency for the electron, and E_r is the radial electric field at a radius r. From Busch's theorem,

$$r^2 \dot{\theta} = \frac{\eta}{2} (B_z r^2 - B_o r_o^2) \qquad (4)$$

r_o being the distance of the electron from the axis at the cathode. The radial electric field inside a beam of radius r_b and current I_o is given by Gauss's theorem:

$$E_r = \frac{I_o}{2\pi \epsilon_o U_o} \left(\frac{r}{r_b^2} \right) \tag{5}$$

The current density in the beam and the axial electron velocity U_o are assumed to be uniform. The equation of motion for an electron at r is therefore

$$\ddot{r} = \frac{\eta I_o}{2\pi \epsilon_o U_o} \frac{r}{r_b^2} + \left(\omega_o^2 \frac{r_o^4}{r^4} - \omega_2^2 \right) \tag{6}$$

where $\omega_o = (\eta/2)B_o$, the Larmor frequency at the cathode and $\omega_L = (\eta/2)B_z$ the Larmor frequency at the electron. From this it can be seen that $\ddot{r}$ is a minimum for fixed values of the other parameters when ω_o is zero, that is when there is no magnetic field at the cathode. This condition leads to the most efficient use of the magnetic field and will therefore be assumed in the following analysis.

If $\ddot{r}$ is set equal to zero for all electrons, then for nonscalloping beam to be produced, one condition required is

$$\omega_L^2 = \frac{\eta I_o}{2\pi \epsilon_o U_o r_b^2}$$

and therefore

$$B_z^2 = \frac{2I_o}{\pi \eta \epsilon_o U_o r_b^2} = B_B^2 \qquad . \tag{7}$$

The value of the magnetic field that satisfies this condition is called the Brillouin field and is denoted B_B as indicated. A second condition on the formation of a nonscalloping beam is that the beam be injected from the cathode region into the uniform field region such that at the equilibrium radius the radial velocity $\overset{\shortmid}{r}$ is zero, that is, so that $\overset{\shortmid}{r} = 0$ when $\overset{\shortparallel}{r} = 0$. The injection conditions are therefore important in the formation of a nonscalloping beam.

For an equilibrium beam we have from Equations (5) and (6),

$$-E_r = \frac{\partial v}{\partial r} = \frac{r}{\eta} \omega_L^2 \qquad .$$

Integrating this gives

$$V = V_a + \frac{r^2}{2\eta} \omega_L^2$$

where V_a is the potential on the beam axis. Now

$$(\overset{\shortmid}{z})^2 + (r\overset{\shortmid}{\theta})^2 = 2\eta V$$

but from Equation (2), when

-136-

$$\omega_o = 0, \qquad \overset{\text{\tiny i}}{\theta} = \omega_L$$

then

$$(\overset{\text{\tiny .}}{Z})^2 = 2\eta V_a + r^2 \omega_L^2 - r^2 \omega_L^2 = 2 \ V_a.$$

Therefore

$$\overset{\bullet}{Z} = \sqrt{2\eta V_a} = u_o \qquad\qquad (8)$$

and all electrons have the same longitudinal velocity u_o corresponding
to the potential on the beam axis. This justifies our earlier
assumption of a single velocity. Putting the value for u_o in Equation
(7) we finally obtain

$$B_B^2 \ = \ \frac{\sqrt{2}\ I_o}{\pi^{3/2}\epsilon_o V_a^{1/2}\ b^2} \qquad . \qquad\qquad (9)$$

A beam which satisfies Equation (7) and has been injected so that
$\overset{\bullet}{r} = 0$ when $\overset{\bullet\bullet}{r} = 0$ is therefore one which does not scallop and in
which all the electrons have the same longitudinal velocity u_o and
the same rotation frequency ω_L. Such a beam is called a Brillouin
beam.

2. CONFINED FLOW

Consider now the case where the cathode is immersed in a uniform
field B_z, so that $B_o = B_z$. Then from Equation (6) with $\omega_o = \omega_L$,

$$\ddot{r} = \eta \frac{\partial V}{\partial r} + r \eta^2 \frac{B_z^2}{4} \left(\frac{r_o^4}{r^4} - 1 \right) \quad . \tag{10}$$

From this, the equilibrium condition for an electron, by putting $\ddot{r} = 0$, is

$$\eta \frac{\partial V}{\partial r} = r' \eta^2 \frac{B_z^2}{4} \left[1 - \left(\frac{r_o}{r'} \right)^4 \right] \tag{11}$$

where r' is the equilibrium radius for this electron. From Gauss's theorem,

$$E_r = \frac{1}{2\pi \epsilon_o r} \int_o^r \sigma(r) \, 2\pi r dr$$

where $\sigma(r)$ is the charge density in the beam which may vary with r. Also

$$\sigma(r) = \frac{J(r)}{u(r)}$$

where $J(r)$ is the current density and $u(r)$ is the electron velocity; therefore

$$E_r = \frac{1}{2\pi \epsilon_o r} \int_o^r \frac{J(r)}{u(r)} \, 2\pi r dr \quad . \tag{12}$$

In the analysis of Brillouin flow it was assumed that the beam was of uniform current density and single velocity so that it had a uniform charge density. It was then shown that under conditions of Brillouin flow these assumptions were valid.

For confined flow however, it is not possible to produce a single-velocity beam. The single-velocity beam of Brillouin flow is due to the combined effects of space-charge depression and beam rotation. The potential increases away from the center of the beam, but this increase in potential is exactly compensated for by an equal increase in rotational energy for all electrons, so that the longitudinal energy remains constant. For confined flow there is less rotation of the beam, and the axial electrons travel more slowly than the outer electrons by an amount that depends on the potential depression.

Therefore an effective electron velocity $u_c(r)$ can be defined by

$$\frac{1}{u_e(r)} = \frac{\displaystyle\int_0^r \frac{J(r)}{u(r)} 2\pi r dr}{\displaystyle\int_0^r J(r) 2\pi r dr} \tag{13}$$

and

$$u_e(r) = \left(2\eta V_e(r)\right)^{1/2} \tag{14}$$

Now

$$\int_0^r J(r) 2\pi r dr = I(r)$$

-139-

where $I(r)$ is the current within a radius r. Combining Equations (11), (12), and (13) gives

$$E_r = \frac{I(r)}{2\pi \epsilon_o u_e(r)r} = \frac{I(r)}{2\pi \epsilon_o r \sqrt{2\eta V_e(r)}} \quad .$$
(15)

Equation (10) then

$$1 - \left(\frac{r_o}{r'}\right)^4 = \frac{\sqrt{2} I(r)}{\pi \epsilon_o \eta^{3/2} B_z^2 V_e^{1/2} r'^2} \quad .$$
(16)

Following Pierce, let

$$k(r) = \frac{1}{\sqrt{2\pi} \epsilon_o \eta^{3/2} B_z^2 V_c^{1/2} r_o^2} \frac{I(r)}{} \quad .$$
(17)

Equation (16) then becomes

$$\left(\frac{r'}{r_o}\right)^4 - 2k(r)\left(\frac{r'}{r_o}\right)^2 - 1 = 0$$

for which the solution is

$$\left(\frac{r'}{r_o}\right) = \left[(k^2 + 1)+k\right]^{1/2} \quad .$$

For usable electron beams $r/r_o \sim 1$ is required; therefore $k \ll 1$, so

$$\frac{r'}{r_o} \sim 1 + \frac{k}{2} \quad . \tag{18}$$

We are essentially concerned with determining the shape of the beam envelope. Let r_b' be the equilibrium radius of the beam and r_{bo} the radius of the beam at the cathode; therefore from Equations (17) and (18)

$$r_b' = r_{bo} \left(1 + \frac{I_o}{2\sqrt{2}\,\epsilon_o \eta^{3/2}\, B_z^2\, V_e\, r_{bo}^2} \right) \quad . \tag{19}$$

As B_z increases for a given cathode current density and beam voltage, r_b' tends to r_{bo}, that is with increasing magnetic field the electrons are constrained more and more to remain at the radius at which they left the cathode.

Now consider the ripple on the beam. Let

$$r_b = r_b' \left(1 + \delta(t) \right) \quad .$$

From Equations (10) and (11)

$$\ddot{r}_b = \omega_L^2 \left[r_b' \left(\frac{r_{bo}^4}{r_b'^4} - 1 \right) - r_b \left(\frac{r_{bo}^4}{r_b^4} - 1 \right) \right]$$

therefore

$$\ddot{r}_b = r_b' \, \omega_L^2 \left[\left(\frac{r_{bo}}{r_b'} \right)^4 \frac{1}{(1+\delta)^3} - (1+\delta) - \left(\frac{r_{bo}}{r_B'} \right)^4 + 1 \right] \tag{20}$$

-141-

Now

$$\ddot{r}_b = r_b' \quad \frac{d^2\delta}{dt^2}$$

and if δ is assumed small, $1/(1 + \delta)^3$ can be expanded in Equation (20) to obtain

$$\frac{d^2\delta}{dt^2} = \omega_L^2 \delta \left[1 + 3 \left(\frac{r_{bo}}{r_b'} \right)^4 \right].$$

The solution to this equation is

$$\delta = C_1 \cos \alpha\, \omega_L t + C_2 \sin \alpha\, \omega_L t,$$

where

$$\alpha = \left[1 + 3 \left(\frac{r_{bo}}{r_b'} \right)^4 \right]^{1/2}.$$

At the cathode $t = 0$, $r_b = r_{bo}$, and $d\delta/dt = 0$; therefore,

$$\delta = \frac{r_b' - r_{bo}}{r_b'} \cos (\alpha\, \omega_L t)$$

and

$$r_b = r_b' + (r_b' - r_{bo}) \cos (\alpha\, \omega_L t).$$

The electron beam envelope is therefore given by

$$r_b(z) = r_b' + (r_b' - r_{bo}) \cos\left(\frac{\alpha\omega_L z}{u}\right)$$

where u is the velocity of the electrons. This beam envelope is shown in Figure 30.

UNIFORM MAGNETIC FIELD, B_Z ⟶
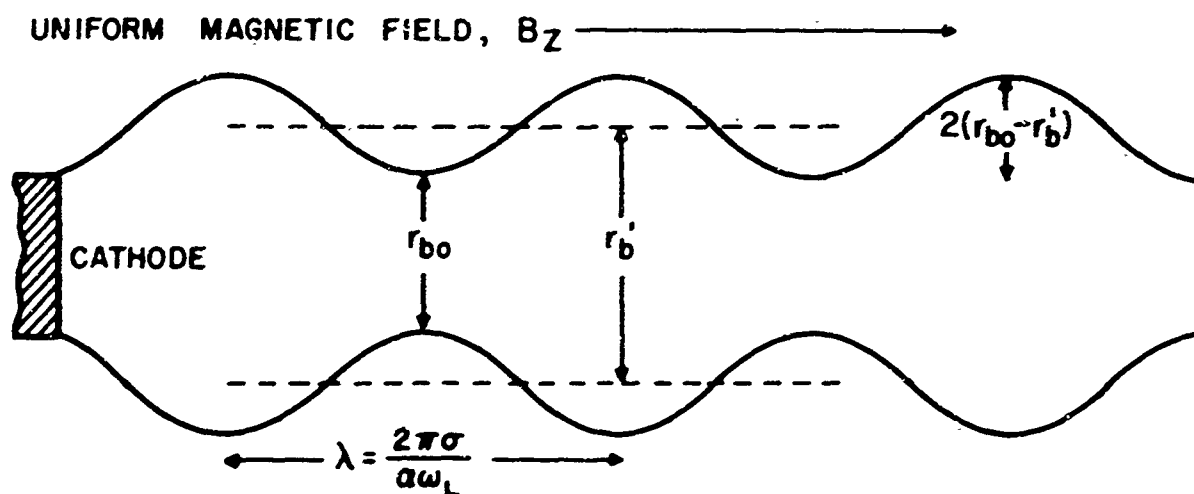
Figure 30. Beam Envelope for Uniform Field Confined Flow.

The minimum beam diameter is r_{bo} and the maximum diameter is $2 r_b' - r_{bo}$; from Equation (21) therefore,

$$\frac{r_{max}}{r_{min}} = 1 + k \quad .$$

In order to compare this focusing with the Brillouin focusing discussed, express k in terms of B_B

$$k = \frac{1}{2} \left(\frac{B_B}{B_z} \right)^2 \left(\frac{r_B}{r_{bo}} \right)^2 \left(\frac{V_a}{V_e} \right)^{1/2} \quad .$$

With the beam radius r_b equal to that of the Brillouin beam, r_B, and with the effective beam voltage V_e, equal to the voltage on the axis of the Brillouin beam, one obtains

$$\frac{r_{max}}{r_{min}} \sim 1 + \frac{1}{2} \left(\frac{B_B}{B_z} \right)^2 \quad . \tag{22}$$

If in

Equation (22) $B_z = 2B_B$, then $r_{max}/r_{min} = 1.12$. A magnetic field with double the Brillouin field strength therefore gives a beam with only 12 per cent scallop and a mean diameter only 6 per cent greater than the diameter at the cathode.

It is now possible to compare the two methods of focusing. Brillouin focusing gives a single-velocity beam with zero scallop and requires the minimum magnetic field to focus a given beam. It is necessary, however, to shield the cathode from the magnetic field and to design the gun so that the beam is injected into the magnetic field with the appropriate radius. Confined focusing produces a beam in which the axial electrons travel more slowly than the outer electrons and in which there is always some scalloping. A confined flow gun can be extremely simple, however, since there is no problem of injecting the beam into the magnetic field, and by increasing the

field to only double the Brillouin value, an acceptable scallop ratio
is obtained. A further important point is that for confined flow
the stronger the magneticfield the better the focusing, and therefore
the value of the magnetic field is not critical. For Brillouin flow
on the other hand, the value of the magnetic field is critical. If
the field is increased above the Brillouin value with the same
injection conditions, these injection conditions will be unsuitable
and the beam may scallop more than a confined flow beam with the same
magnetic field. Also for Brillouin focusing, when B_z is greater than
B_B, the outer electrons travel more slowly than those on the beam
axis and in an extreme case these electrons can stop altogether and
turn back. For these reasons and because very strong magnetic fields
generated on a pulsed basis were available, confined-flow focusing
was adopted. This allowed the use of a very simple gun with which
beams with a wide range of currents and voltages could be readily
focused. Putting some numerical values into Equation (9) gives

$$B_B = 8.3 \times 10^{-4} \ \frac{I_o^{1/2}}{V_a^{1/4} \, r} \tag{23}$$

and

$$B_B = 8.3 \times 10^{-4} \ \frac{I_o^{1/3} \, p^{1/6}}{r} \tag{24}$$

where the perveance p is defined by

$$p = \frac{I_o}{V^{3/2}} \quad .$$

The total current I_o is simply given by

$$I_o = \pi r^2 J \qquad\qquad (25)$$

where J is the current density.

Equations (23), (24) and (25) are plotted in Figure 31 for a value of $r = 0.0025$ in. Equation (23) is plotted for several values of V_a and Equation (24) is plotted for several values of p.

For a confined-flow beam in an infinite magnetic field, the maximum theoretical perveance is 32.5×10^{-6}. When this perveance is reached, the potential on the beam axis reaches an unstable value at which it drops abruptly to zero. The $p = 32.5 \times 10^{-6}$ line of Figure 31 therefore represents the maximum value that can be achieved theoretically. In practice for a solid beam it would not be desirable to use a perveance much greater than about 5 because of the velocity spread in the beam. The repeatable current densities achieved with indirect emission were about 450 a/cm^2 corresponding to a current of 50 ma. At perveance 5×10^{-6} the Brillouin field for this beam is 6,000 gauss and therefore a field of twice this strength is 12,000 gauss. With a pulsed magnet, a field of 70 kgauss was easily produced so there was no problem in focusing this beam. With this magnetic field and beam radius and a perveance value of 5×10^{-6}, it should be possible to focus a beam of 7 a at 10 kv. The current density in this beam would be 6×10^4 a/cm^2. Current densities approaching this value have been obtained using direct emission. Such a beam, if it
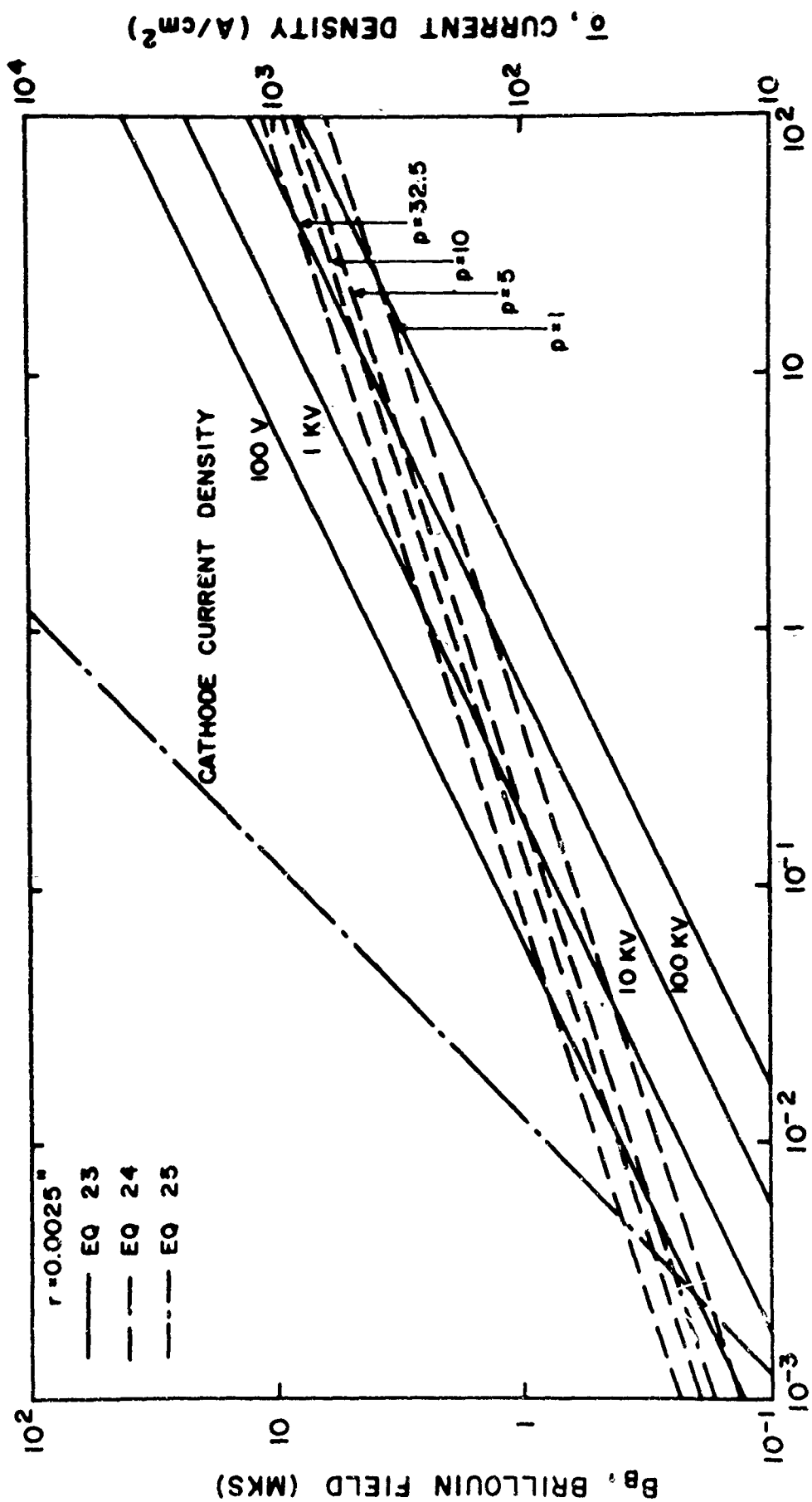
Figure 31. Plot of Equations 23, 24 and 25.

could be achieved, would have a power of 70 kw and would therefore
be extremely useful in generating millimeter waves at high powers.
Equation (23) shows that for constant voltage, B_B is proportional
to the square root of the beam current density. By increasing the
beam diameter therefore, even larger currents could be focused using
this magnet field. These figures illustrate clearly that using a
pulsed magnetic field of 70 k gauss it should be possible to focus
beams with current densities very much larger than have been achieved
using indirect emission and larger even than those which have been
achieved using direct emission.

3. POTENTIAL DEPRESSION RESULTING FROM SPACE CHARGE

For a cylindrical beam of uniform current density J and radius
r_a traveling through a metal cylinder of radius r_o at a potential
V_o the potential on a diameter is of the form shown in Figure 32.
It can readily be shown that outside the beam, the potential is
given by

$$V_r = V_o - \frac{1}{2\pi(\frac{2e}{m})^{1/2} \epsilon_o} \, p \, V_o \, \log\left(\frac{r_o}{r}\right)$$

and inside the beam the potential is given by

$$V_r = V_o - \frac{1}{2\pi(\frac{2e}{m})^{1/2} \epsilon_o} \, pV_o \left[\log\left(\frac{r_o}{r_a}\right) + \frac{1}{4}\left(1 - \left(\frac{r^2}{r_a^2}\right)\right)\right]$$
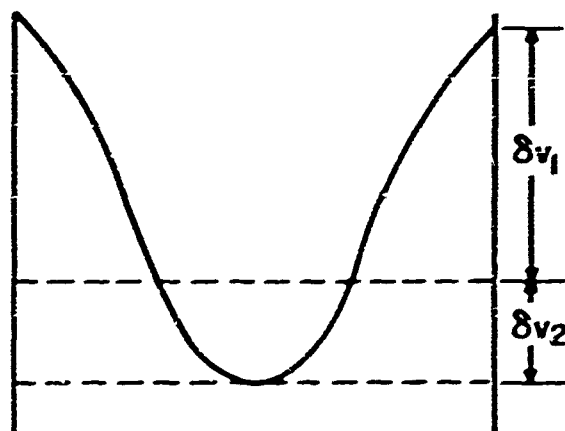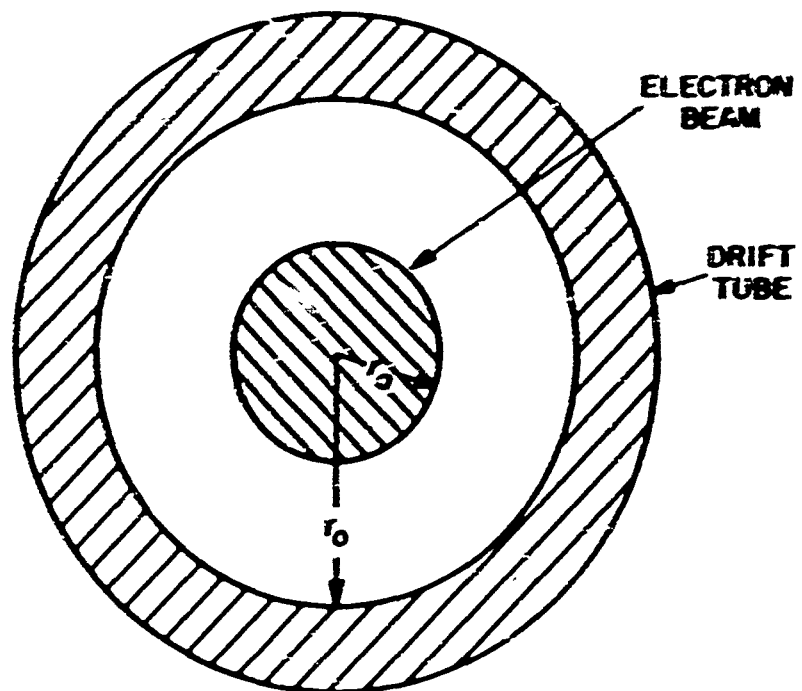
Figure 32. Potential Depression Resulting from Space
Charge of Beam Inside Metal Cylinder.

therefore

$$\frac{\delta \overline{V}_1}{\overline{V}_0} = \frac{1}{2\pi(2e/m)^{3/2} \epsilon_0} \quad p \log_e \left(\frac{r_0}{r_a}\right) = 3.16 \times 10^4 \log_e \left(\frac{r_0}{r_a}\right)$$

and

$$\frac{\delta \overline{V}_2}{\overline{V}_0} = \frac{1}{2\pi(2e/m)^{3/2} \epsilon_0} \quad \frac{p}{4} = 3.16 \times 10^4 \frac{p}{4} \quad .$$

For beam tester B of the experiments, $(r_0/r_2) = 2$; therefore

$$\frac{\delta \overline{V}_1}{\overline{V}_0} = 3.16 \times 10^4 p \log_e 2 = 2.19 \times 10^4 p \qquad (26)$$

$$\frac{\delta \overline{V}_2}{\overline{V}_0} = 3.16 \times 10^4 \frac{p}{4} = .79 \times 10^4 p \qquad . \qquad (27)$$

In this case therefore the potential depression from the walls of
the tube to the beam was nearly three times the depression inside
of the beam.

From Table 1 it can be seen that a beam of perveance 5 has
only a 4 per cent change of voltage from the axis to the outer edge.
Corresponding to this voltage range there would be a 2 per cent
spread in velocities. The potential at the outer edge of such a

beam would be 11 per cent below that of the drift tube. With a hollow beam, the velocity spread for a given value of perveance can be considerably reduced. The potential drop from the drift tube to the beam can also be made small by keeping the beam close to the drift tube walls.

TABLE 1

$p \times 10^6$	$\delta \bar{v}_1/\bar{v}_o \times 100$	$\delta \bar{v}_2/\bar{v}_o \times 100$	$\delta \bar{v}/\bar{v}_o \times 100$
1	2.19	.79	2.98
5	10.8	4.0	14.8
10	21.9	7.9	29.8
30	65.7	23.7	89.4

APPENDIX B. ABSORPTION OF LIGHT INCIDENT ON A METAL SURFACE

1. THEORY

The optical properties of a metal of interest are:

a. The fraction of the incident light absorbed, 1-R, where R is the reflection coefficient and is a function of the angle of incidence, the polarization of the light, and the frequency ω.

b. The characteristic absorption depth or skin depth δ in which the electromagnetic fields fall to $1/e$ of their value at the interface.

c. The photoelectric current expected for a given radiation intensity.

Properties a and b, which are relevant to the heating of the surface and thermionic emission are the main topics dealt with in this section, and only a few comments relevant to photoelectric current are made.

In the most elementary treatment of the optical properties of a metal, a macroscopic model is used.[10,11] The electromagnetic radiation is considered incident on an isotropic medium characterized by a complex refractive index $\underline{N}$, or by what is equivalent, a complex dielectric constant $\underline{\epsilon}$, then

$$\underline{N} = n + ik$$

and

$$\underline{\epsilon} = \epsilon_1 + i\,\epsilon_2$$

where n is the real refractive index, k is the extinction coefficient, and ϵ_1 is the real and ϵ_2 the imaginary part of the complex dielectric constant. The propagation in the medium of a plane electromagnetic wave of frequency ω and amplitude E is described by:

$$E = E_o \, e^{-\frac{k\omega x}{c}} \, e^{i\omega(t - \frac{nx}{c})}$$

$$= E_o \, e^{i\omega(t - \frac{Nx}{c})} \quad . \tag{28}$$

The skin depth and reflection coefficient are related to n and k as follows:

$$\delta = \frac{c}{k\omega} \tag{29}$$

$$R = \frac{(n-1)^2 + k^2}{(n+1)^2 + k^2} \quad . \tag{30}$$

Equation (29) follows directly from Equation (28) and Equation (30) is obtained from the condition of continuity of the tangential component of E and the normal component of H at the vacuum-metal interface. By applying Maxwell's equations to the metal, n and k can be related to the macroscopic properties of the metal; that is, to σ_o, the d-c electrical conductivity, μ the magnetic susceptibility (which is taken to be one for nonmagnetic materials), and ϵ the

dielectric constant. This gives

$$\epsilon_1 + i\,\epsilon_2 = (n^2 - k^2) + i2nk = \mu\epsilon + i\,\frac{\sigma_0\mu}{\omega\epsilon_0}\quad.$$

Equating real and imaginary parts gives

$$\epsilon_1 = n^2 - k^2 = \mu\epsilon \simeq 1$$

$$\epsilon_2 = 2nk = \frac{\sigma_0\mu}{\omega\epsilon}\quad.$$

For frequencies for which this approximation is valid and for metallic conductivities,

$$\left(\frac{\sigma_0\mu}{2\omega\epsilon}\right) >> 1$$

and therefore

$$n \simeq k \simeq \left(\frac{\sigma_0\mu}{2\omega\epsilon_0}\right)^{1/2}$$

$$\delta = \left(\frac{1}{\pi\sigma_0\,\nu\mu\mu_0}\right)^{1/2}$$

$$R \simeq 1 - 2\left(\frac{\sigma_0\mu}{2\omega\epsilon_0}\right)^{1/2}$$

These are the classical relationships found to be valid for metals for wavelengths up to 10^{-3} cm, that is up to the far infrared. If they are applied to tungsten at about room temperature for the radiation from a ruby laser, the following values are obtained:

$$n = k = 20.4$$

$$\delta = 54.4 \ \AA^{\circ}$$

$$R = 0.9 \qquad .$$

The radiation, of which 90 per cent is reflected, is absorbed in a depth of 54.5°A; that is, a few tens of atomic layers; and the wavelength in the metal is 350°A compared with 7,000 $\overset{\circ}{A}$ for free space.

These values for tungsten have previously been used to calculate the thermal response of the metal to laser irradiation and fortunately are of the right order of magnitude, although the theory is not valid at this high frequency. In order to see why the theory is not valid it is necessary to consider the microscopic model of a metal and the processes involved in the interaction of radiation with the metal.

The metal consists of a regular array of atomic cores; which are the atomic nuclei with their inner electron shells. One or more of the electrons of the outer shells of each atom are virtually free to move through the metal and form an electron "gas." By neglecting the interaction of these electrons with each other and considering the electrons to be in states described by wave functions that have

the space periodicity of the lattice (Bloch waves), each electronic

state can be characterized by a wave vector $\underline{k}$. In the periodic

potential of the lattice, it is found that only certain energy bands

are available to the electrons, and between are energy gaps or

forbidden bands. Electronic wave functions with the periodicity of

the lattice are not scattered by lattice centers in their equilibrium

positions and therefore energy cannot be transferred from the lattice

to the electrons or vice versa. It is only when the lattice centers

are disturbed from their equilibrium position that they can scatter

electrons, and they are disturbed from equilibrium only when excited

into one of the quantized oscillator states. The electrons therefore

interact only with the excitations of the lattice, these excitations

being called phonons. When an electron interacts with a phonon there

is a transfer energy $h\nu$ either from phonon to electron or vice versa;

electrons cannot make elastic collisions with phonons. We now consider

the interactions of quantized radiation, i.e., photons, with the

electron-phonon system.

When a photon and electron "collide," the electron is excited

to a higher energy state in a quantum jump and the photon is annihilated

only if empty states are available at the appropriate level into which

the electron can be excited. Another condition on this excitation is

that, in the so-called reduced $\underline{k}$ space, $k = k'$, or in other words,

$\Delta \underline{k} = 0$. This is an expression of the conservation of momentum (the

momentum of the photon is negligible compared with that of the electron)

and restricts the electrons to jumping only between states in different

bands with the same value of wave vector.

For a simple photon-electron collision therefore, only interband excitations are allowed; intraband excitations, that is excitations between states in the same band, are forbidden. For a system in which the bands do not overlap or for which there is a gap between the highest occupied level in one band and the lowest unoccupied level in the next band, there must be a threshold frequency for this process. This is in fact the c se for all metals. In order to explain absorption of radiation at low frequencies, therefore, we need to look at another process, that of the simultaneous interaction of a photon, an electron, and a phonon. In this interaction, momentum is conserved without the restriction $\Delta \underline{k} = 0$, so that intraband transitions are possible if appropriate electronic states are available into which the electrons can be excited. Simultaneous interaction of a photon and an electron with the surface potential barrier also allows intraband excitations. Having been excited, an electron may, if it has gain sufficient energy and is close to the surface, escape from the metal. This is the photoelectric effect. All other excited electrons undergo interactions with the phonons giving up their energy to the lattice until the electron and phonon gases are in thermal equilibrium. Another possible process is the collision of the excited electrons with other electrons with the transfer of a much larger fraction of their excitation energy per collision than for collisions with phonons. Electrons close to the Fermi surface can only exchange energy with a few other electrons which are also close to this surface and therefore in general (for example at low frequencies and especially for d-c conductivity

calculations) the electron-electron mean-free paths are long compared with electron-phonon mean-free paths. However an electron in a highly excited state can interact with many other electrons, since it can raise these above the Fermi level in a collision, that is to an energy region where there are many unoccupied states. Hence the mean-free path for highly excited electrons is very much less than for electrons near the Fermi surface, and electron-electron collisions become an important process of energy exchange for these electrons. It is possible that electron-electron collisions are more powerful in preventing highly excited electrons from escaping from inside the metal near the surface than the electron - phonon collisions, which are nearly elastic.

Two other possible processes are of interest.

1. The interaction of two photons simultaneously with an electron and either a phonon or the potential barrier at the surface; this would make possible photoelectric emission for incident frequencies lower than the normal photoelectric threshold, so long as the frequency was more than half the normal threshold value.

2. Interaction of a photon and a phonon with an electron that had been excited to a higher level and had not undergone sufficient collisions to return it to an equilibrium state. This could influence photoelectric emission as in process 1.

The probability of process 1 taking place is proportional to the square of the incident phonon flux or the square of the radiation intensity and is therefore possibly of interest in the radiation

intensities achievable with a pulsed ruby laser. Process 2 is also proportional to the square of the incident photon flux. In the very high temperatures produced by laser irradiation, there may also be sufficient high-energy electrons on the tail of the Fermi distribution to give appreciable photoelectric emission. Under the conditions of high temperature created by laser irradiation, it is difficult to see how photoelectric and thermionic emission could be differentiated experimentally.

In order to calculate the optical properties of a metal it is necessary to calculate the probability of the various possible processes described above using simplified models. For the relatively simple alkali metals of the noble metals which do not have the Fermi surface in an overlapping band structure, much of this has been done and good experimental agreement has been achieved. For other metals, however, most of which have an overlapping band structure (as does tungsten), the problem is even more complex and had not been solved.

Although the full quantum mechanical problem has not been solved, a useful method is the semi-classical approach. In its simplest form, this gives good agreement with theory for the noble and alkali metals, but not for more complex metals. By extending it in a somewhat empirical way, however, the model used can be made to fit these other metals.

Following Drude 12 the electrons in the metal are assumed to be free and to have a mean collision time T with the lattice. The electrons are accelerated in the incident electromagnetic field

and give up the energy they have gained in colliding with the lattice.
The equation of motion is

$$\frac{\partial v}{\partial t} = \frac{e}{m} E - \frac{1}{\tau} v \quad .$$

If E depends on the time as $e^{i\omega t}$, a solution of this is

$$v = \frac{e\, E}{m \left(i\omega + \frac{1}{\tau} \right)} \quad .$$

Hence the current density is

$$J = \frac{ne^2}{m(i\omega + \frac{1}{\tau})}\, E = \frac{\sigma_o}{1 + i\omega \tau}\, E$$

$$J = \frac{\sigma_o}{1 + \omega^2 \tau^2}\, (E - \tau \frac{\partial E}{\partial t}) \quad .$$

The first term is the conduction current, the second the displacement current; therefore

$$\sigma_\omega = \frac{\sigma_o}{1 + \omega^2 \tau^2}$$

and,

$$\epsilon_1 = 1 - \frac{4\pi r \sigma_o}{1 + \omega^2 \tau^2} \quad .$$

-160-

Therefore for

$$\omega\tau \ll 1, \qquad \sigma_\omega = \sigma_0$$

indicating that the classical theory given earlier is valid.

In order to make this model fit the experimental values of the measured optical properties for tungsten and nickel over the wavelength range 0.365 μ to 2.65 μ Roberts,[13] following Drude, assumed not just one class of free electrons but two, each with a different relaxation time. This is a somewhat empirical extension of the theory and Roberts does not attempt to fit the second group of electrons to any excitation process in the metal. The first group having the longest relaxation time, are mainly responsible for the d-c and low-frequency conductivity of the metal; the second group, having a relaxation time more than an order of magnitude less than the first group, make significant contribution to the conductivity only at high frequencies (infrared and optical). Perhaps the short relaxation time of the second group of electrons is due to electron-electron collisions, which become important only for highly excited electrons and therefore for high frequencies. For these highly excited electrons the mean-free path should be of the order of the interatomic spacing 14, which is of an order of magnitude that agrees with Robert's data.

2. EXPERIMENTAL DATA

Since we are concerned with the reflection and absorption of

radiation at a surface, the conditions at the surface are, from the experimental point of view very important. Without care the results can be more dependent on the surface than on the bulk metal. A polished surface, for example, has been shown to consist of a layer of amorphous material a few Angstrom units thick below which is a microcrystalling layer that can be up to several hundred Angstrom units thick; that is, thicker than the skin depth. The lack of order in the amorphous layer and the many crystal boundaries in the micro-crystalline layer profoundly affect the optical properties.

The most important data available for tungsten is that of Roberts who used tungsten, recrystallized by heating in a vacuum and then chemically etched. From Roberts' data, plotted in the form of curves of the real and imaginary part of the dielectric constant obtained by measuring the reflection coefficient as a function of angle of incidence for light polarized perpendicular and parallel to the surface,

$$k = k' - ik''$$

$$\sqrt{k} = n - ik$$

therefore

$$k' = n^2 - k^2 = \epsilon_1$$

$$k'' = 2nk = \epsilon_2 \qquad .$$

From these are obtained

$$n = \sqrt{r} \ \cos \phi/2$$

$$k = \sqrt{r} \ \sin \phi/2$$

where

$$r^2 = k'^2 + k''^2$$

$$\tan \phi = \frac{k''}{k'} \qquad .$$

At a wavelength of 0.7μ the values obtained are

$$k' = 6$$
$$k'' = 25$$

which vary little with temperature over the measured range. From these are obtained

$$n = 4.0 \qquad\qquad k = 3.14$$

$$\delta = 360 \ \text{Å}$$

$$R = 0.56 \qquad\qquad 1 - R = 0.44$$

Therefore 44 per cent of the incident radiation is absorbed in a layer of depth 360 Å, and the wavelength in the metal is $0.17 \ \mu$ compared with a free-space wavelength of 0.7μ.

It is noteworthy that for light polarized parallel to the plane of incidence, maximum absorption does not occur at normal incidence but at some other angle ϕ called the principal angle of incidence, giving[15]

$$R_p = \frac{(n - \frac{1}{\cos\phi})^2 + k^2}{(n + \frac{1}{\cos\phi})^2 + k^2}$$

and

$$\sin\phi \tan\phi = n(1 + k^2)^{1/2}$$

where R_p is the reflection coefficient at the principal angle of incidence. For tungsten these give

$$\phi = 85^0$$

$$R_p = 0.3$$

$$(1-R_p) = 0.7 \qquad .$$

For plane polarized light incident on a tungsten surface at the principal angle of incidence of 85^0, the absorption coefficient is therefore 0.7. This is significantly higher than the absorption coefficient for normal incidence.

APPENDIX C. CONSIDERATIONS OF LASER REQUIREMENTS

The energy required to melt a 0.005 in. diameter region of the 0.0005 in. thick tungsten ribbon is 2.5 millijoules. Assuming an absorbtion coefficient of 46 per cent, gives a required incident energy of 5.5 millijoules. This figure is a factor of 10^3 less than was available from the laser used for the experiments. In any application it would be desirable to use a laser that gave the required energy with maximum efficiency. This would involve working well above threshold, therefore a small ruby crystal of approximately one thousandth the volume of the present laser would be required; that is, a crystal with a length of 0.6 in. long and a diameter of 0.025 in. if the present crystal were scaled by a factor of ten on all dimensions. The reduction would increase the surface-to-volume ratio by a factor of ten, thus easing the cooling problem. If this small laser could be made to have the same efficiency as the present laser, the required energy into the pumping lamp would be about 1.6 joules per pulse. If the laser were operated at 50 pulses per second, the average lamp power would be about 80 w. It should therefore be possible to design a small compact laser head and power supply to satisfy these requirements. The estimated crystal size quoted above is close to that used by Nelson and Boyle [16] to produce a continuous ruby laser. So far ruby laser design has mainly been aimed at producing more powerful and efficient lasers. The design of a low-energy laser would provide an interesting departure from this trend.

REFERENCES

1. F. Giori, L. A. MacKenzie, E. J. McKinney, "Laser-induced Thermionic Emission," Appl. Phys. Let. 25 (1963).

2. G. C. Dalman and T. S. Wen, "Laser-heated Cathode," Proc. I.E.E.E. 52 (1964) 200.

3. B. W. Woodward and G. J. Wolga, "Fabrication of High-Efficiency Laser Cavities," Rev. Sci. Inst., 33 (1962), 1463.

4. Tingye Lee and S. D. Sims, "A Calorimeter for Energy Measurements of Optical Masers," Appl. Optics, 1 (1962), 325.

5. E. K. Daman and J. T. Flynn, "A Liquid Calorimeter for High-Energy Lasers," Appl. Optics, 2 (1963), 163.

6. M. M. Hercher, "Optical Characteristics of Ruby Laser Emission," Ph. D. Thesis, Univ. Rochester, Rochester, New York, 1963.

7. T. P. Hughes and K. M. Young, "Mode Sequences in Ruby Laser Emission," Nature, 196 (1962), 332.

8. M. C. Chen, "Analysis of the Electron Emission from a Tungsten Surface Indirectly Heated by a Laser Pulse," M. S. Thesis, Chiao-Tung University, Taiwan, 1963.

9. H. A. Jones and I. Langmuir, "The Characteristics of Tungsten Filaments as Functions of Temperature," Gen. Elec. Rev., 30 (1927), 354.

10. N. F. Mott and H. Jones, Properties of Metals and Alloys, Oxford: Clarendon, 1936, Ch. 3.

11. M. Parker Givens, "Optical Properties of Metals," _Solid State Physics_, Vol. VI, New York: Academic Press, 1958.

12. P. Drude, Ueber Oberflachenschichten," _Ann. Physik_, _36_, (1889) 865.

13. S. Roberts, "Optical Properties of Nickel and Tungsten and their Interpretation According to Drude's Formula," _Phys. Rev._, _114_ (1959), 104.

14. R. E. Peierls, _Quantum Theory of Solids_, Oxford: Clarendon, 1955, Ch. 9.

15. F. A. Jenkins and H. E. White, _Fundamentals of Optics_, New York: McGraw-Hill, 1950.

16. D. F. Nelson and W. S. Boyle, "A Continuously Operating Ruby Optical Maser," _Appl. Optics_, _1_ (1962), 181.